

Phonon Transport in Molecular Dynamics Simulations: Formulation and Thermal Conductivity Prediction

A.J.H. MCGAUGHEY¹ and M. KAVIANY²

¹*Department of Mechanical Engineering, Carnegie Mellon University, Pittsburgh, PA 15213-3890, USA; E-mail: mcgaughey@cmu.edu*

²*Department of Mechanical Engineering, University of Michigan, Ann Arbor, MI 48109-2125, USA; E-mail: kaviany@umich.edu*

I. Introduction

A. CHALLENGES AT MICRO- AND NANO-SCALES

The past decade has seen rapid progress in the design, manufacturing, and application of electromechanical devices at micron and nanometer length scales. While advances in fabrication techniques, material characterization, and system integration continue, a lag exists in theoretical approaches that can successfully predict how these devices will behave. As classical and continuum theories reach their limits, phenomena that may be insignificant at larger length and time scales (such as interfacial effects) can become dominant. Only a basic, qualitative understanding of the observed behavior exists in many cases. In part, one can attribute this lack of knowledge to the difficulty in solving the Schrödinger equation exactly for anything more than a hydrogen atom, and to the enormous computational resources needed to solve it numerically for a system with more than a few hundred atoms.

By ignoring the electrons and instead moving to an atomic-level description, the computational demands are greatly reduced. Though neglecting electrons removes the ability to model the associated electrical and thermal transport, one can still consider many of the relevant thermal issues in devices. These include the transport of phonons in superlattices and across material interfaces and grain boundaries, the dissipation of heat in integrated circuits (the dimensions of FETs are approaching tens of nanometers), and low-dimensional effects in structures such as quantum dots and nanotubes. Descriptions of the current challenges in experiments, theory, and computations can be found in Refs. [1] and [2].

Molecular dynamics (MD) simulations, Monte Carlo methods, the Boltzmann transport equation (BTE), Brownian dynamics, and dissipative particle dynamics are useful in investigations of systems beyond the scope of first principle calculations. The approach chosen depends on the length and time scales associated with the problem of interest, and what level of detail is required in the analysis. Not all of the methods listed allow for complete atomic-level resolution or an investigation of the system dynamics. One often selects a suitable methodology by considering the relative magnitudes of the carrier mean free path and system dimensions (i.e., the layer thickness in a superlattice). This comparison will indicate if the transport is primarily diffusive, ballistic, or a combination of the two, and if a continuum or discrete technique is required.

B. MOTIVATION FOR USING MOLECULAR DYNAMICS SIMULATIONS

We will focus here on dielectric solids, where the valence electrons are tightly bound to the atomic nuclei, at temperatures low enough that photonic contributions to thermal transport are negligible¹. Phonons, energy waves associated with the lattice dynamics, will dominate the thermal transport. In such systems, one gains an advantage by moving from the continuum to the atomic scale in that the lattice dynamics can be completely and explicitly modeled [3–6]. Analysis of thermal transport in dielectrics is typically done in the phonon space (also referred to as momentum space or frequency space), which is a wave-based description of the lattice dynamics. For a harmonic solid, the phonon system corresponds to a set of independent harmonic oscillators. This system is far simpler to analyze than the coupled motions of the atoms in real space. The harmonic theory is only exact at zero temperature, however. As temperature increases, anharmonic (higher-order) effects, which are difficult to model theoretically, become important.

While phonon space is convenient for analysis, the design and synthesis of new materials is performed in real space. It can be difficult to move from criteria in phonon space to a crystal structure that will have the desired behavior. For example, the link between the positions of the atoms in a large unit cell and the relaxation times of the associated phonon modes is not intuitive. A research environment has thus developed where design is done in real space, while analysis is performed in phonon space. From a thermal transport standpoint, there are no easy ways to move between these paradigms without losing important information. To proceed, one must

¹ The analysis techniques presented can also be taken to isolate phonon effects in materials with mobile electrons. Caution must be taken in interpreting the results, however, due to the possible strong coupling between the phonon and electron systems.

move either the analysis to real space, or the design to phonon space, or develop new tools to bridge the existing approaches.

MD simulations are a suitable tool for the analysis of dielectrics at finite temperature and for the bridging of real and phonon space analysis techniques. Most importantly, MD simulations allow for the natural inclusion of anharmonic effects and for atomic-level observations that are not possible in experiments. As large-scale computing capabilities continue to grow and component sizes decrease, the dimensions of systems accessible with MD approach those of real devices. Simulations run in parallel (e.g., on a Beowulf cluster) can handle systems with tens of millions of atoms, and supercomputers have modeled systems with billions of atoms [7,8].

C. SCOPE

The objective of this review is to describe how MD simulations can be used to further the understanding of solid-phase conduction heat transfer at the atomic level. The simulations can both complement experimental and theoretical work, and give new insights.

In Section II continuum-level thermal transport analysis is reviewed, and its limitations are used to motivate atomic-level analysis. Through this discussion, thermal conductivity, the material property that is the focus of much of the review, is introduced.

In Section III the MD method is described, and general details on setting up and running simulations are presented. This is done in the context of the Lennard-Jones (LJ) potential, and the associated face-centered cubic (fcc) crystal, amorphous, and liquid phases of argon. Investigating a simple system allows one to elucidate results that might not be evident in a more complex structure. Equilibrium system parameters, such as the density, specific heat, and root mean square (RMS) atomic displacement are calculated, and compared to predictions made directly from the interatomic potential and from other theories. The harmonic description of the phonon system is introduced, and used in conjunction with simulation results to calculate phonon dispersion curves and relaxation times. The MD simulations provide data that allow for the incorporation of anharmonic effects.

Moving toward issues of thermal transport, Section IV contains a discussion of the nature of phonon transport in the MD system. The small simulation cells typically studied and the classical nature of the simulations lead to a different description of phonon transport than in the standard quantum-particle-based model. Methods to predict thermal conductivity using MD simulations are then reviewed in Sections V–VII. Attention is given particularly to the Greek–Kubo (GK) method and an approach based on a direct application of the Fourier law of conduction (the direct method).

Consideration is given to crystalline and amorphous phases, predictions for bulk phases and finite structures, and what can be gained from the simulations beyond the thermal conductivity value. Limitations of each approach, and of MD in general, are assessed by considering size effects, quantum corrections, and the nature of the interatomic potential.

II. Conduction Heat Transfer and Thermal Conductivity of Solids

Conduction heat transfer in a solid can be realized through the transport of phonons, electrons, and photons. The individual contributions of these carriers can vary widely depending on the material studied and its temperature. The thermal conductivity, k , of a substance indicates the ease with which thermal energy can be transferred through it by conduction. Unlike the specific heat, which has an equilibrium definition based on classical thermodynamics, the thermal conductivity is defined as the constant of proportionality relating the temperature gradient, ∇T , and heat flux, \mathbf{q} , in a material by

$$\mathbf{q} = -\mathbf{k}\nabla T \quad (1)$$

This is the Fourier law of conduction, and was originally formulated from empirical results. The thermal conductivity is generally a second-order tensor, but in a material with cubic isotropy it reduces to a scalar. The thermal conductivity is an intensive property (i.e., it can vary from point to point in a continuum) and is a function of both pressure and temperature. In the context of engineering heat transfer, an object's thermal resistance is a function of both its thermal conductivity and its geometry.

By combining the Fourier law and the energy equation, and assuming no mass transfer and constant properties, one obtains the partial differential equation

$$k\nabla^2 T = \rho C_v \frac{\partial T}{\partial t} \quad (2)$$

Here, ρ is the mass density, C_v the specific heat (J/kg K), and t the time. Given the appropriate boundary and initial conditions, this equation can be solved to give the temperature distribution in a system of interest. Equations (1) and (2) are the standard basis for describing conduction heat transfer. The validity and applicability of each is based on these assumptions:

- The system behaves classically and can be modeled as a continuum.
- The energy carrier transport, be it a result of phonons, electrons, or photons, is diffuse (i.e., the scattering of the carriers is primarily a

result of interactions with other carriers). Cases where interface and/or boundary effects dominate correspond to ballistic transport, and cannot be considered in this formulation.

- The material properties are known.

At small length scales the suitability of the first two criteria may be questionable, and experimental property data may not always be available. Alternative approaches (such as the BTE or MD) may be required.

Consider the required properties in Eq. (2). Given the chemical composition of a material and some atomic-level length scales (e.g., the lattice constant for a crystal), predicting its density is straightforward. For the specific heat, the Debye approach [3] (based on quantum mechanics) models most solids well, although the Debye temperature must first be fit from the experimental data. One can approximate the high-temperature specific heat from the Dulong–Petit theory [3], which is based on classical statistical thermodynamics, and requires only the molecular mass for its evaluation. The thermal conductivity is a more elusive quantity, however. It is a material property related to energy transport, unlike the density and specific heat, which are associated with structure and energy storage, respectively. As opposed to thinking of the thermal conductivity in terms of a static, equilibrium system, one typically envisions this property in the context of nonequilibrium, although it can be determined in an equilibrium system by looking at the decay of energy fluctuations (the GK method, described in Section V). Experimental techniques for determining the thermal conductivity directly based on the Fourier law have been developed, and analogous computational techniques exist (see Section VI). Experimentally, it is also possible to determine the thermal diffusivity, α , from which the thermal conductivity can be inferred ($\alpha = k/\rho C_p$, where C_p is the volumetric specific heat at constant pressure, equal to C_v for a solid).

In Fig. 1, experimental thermal conductivities of a number of solids are plotted over a wide temperature range [9,10]. The energy carriers represented are electrons and phonons. The range of thermal conductivities available at essentially any temperature covers five orders of magnitude. While some overall trends are evident (e.g., amorphous materials have a much lower thermal conductivity and a different temperature dependence of this property than crystals), one cannot easily explain much of the behavior. The finite thermal conductivity of a perfect crystal is a result of anharmonic effects. Modeling these exactly is difficult, making it a challenge to realize simple and accurate expressions for the thermal conductivity. In Ref. [11], methods for predicting the thermal conductivity are reviewed. The available models often require simplifying assumptions about the nature of the thermal transport and/or require that one fit the predictions to experimental

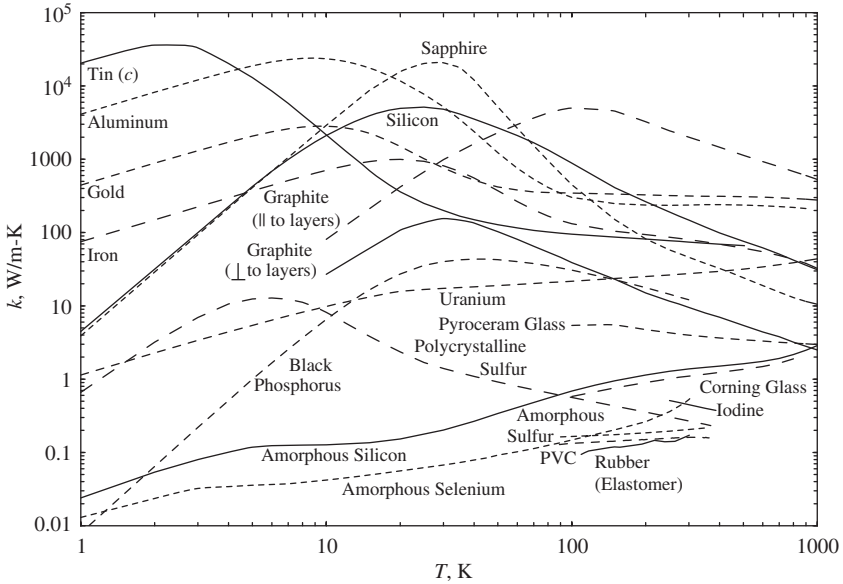


FIG. 1. Experimental thermal conductivities of crystalline and amorphous solids plotted as a function of temperature [9,10]. The materials presented are examples of dielectrics, semiconductors, and metals. They cover the spectrum of electron-dominated to phonon-dominated thermal transport. Note the wide range of thermal conductivity values available at almost any temperature.

data. Omini and Sparavigna [12] have developed a solution method based on an iterative solution of the BTE free of some of these assumptions. While the predictions are in reasonable agreement with experimental data, the required calculations are complex. As such, discussions of thermal conductivity typically revolve around the simple kinetic theory expression [6]

$$k = \frac{1}{3} \rho C_v v \Lambda \quad (3)$$

where v is a representative carrier velocity and Λ the carrier mean free path, the average distance traveled between collisions. Reported values of the mean free path are often calculated using Eq. (3) and experimental values of the other parameters, including the thermal conductivity. This expression for the thermal conductivity assumes a similar behavior for all carriers, which may mask a significant amount of the underlying physics, especially in a solid.

In Fig. 2, the thermal conductivities of materials composed of carbon atoms are plotted as a function of temperature [9,13]. Clearly, thermal

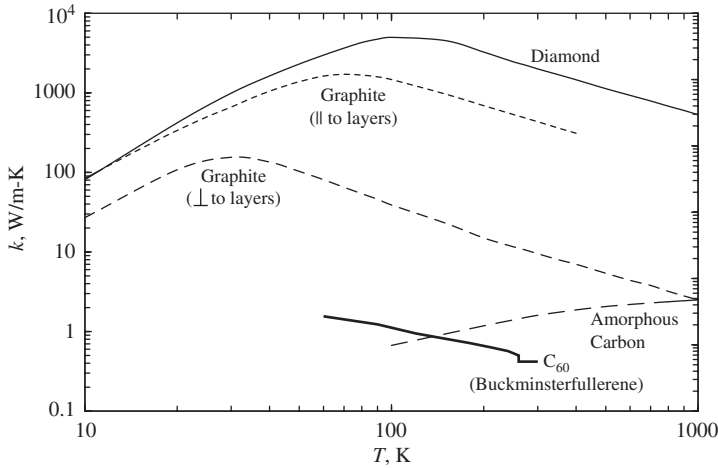


FIG. 2. Thermal conductivities of carbon-based solids plotted as a function of temperature [9,13]. The discontinuity in the C_{60} curve is a result of a phase transition.

transport relates to both what a material is made of, and how the constituent atoms are arranged. An explanation of the second effect is not as obvious as it would be for either the density or specific heat [i.e., the more atoms in a given volume, the higher the density, and higher the specific heat (on a volumetric basis)].

Without elaborate expressions for the mean free path (which can vary depending on wavelength, temperature, etc.), seeing how a relation such as Eq. (3) could be used to explain the trends in Figs. 1 and 2 is difficult. Many of the theoretical challenges can be bypassed in the MD formulation (e.g., anharmonic effects are naturally included), making this approach a good option for investigating atomic-level thermal transport in dielectrics.

III. Real and Phonon Space Analyses

A. MOLECULAR DYNAMICS SIMULATION

In an MD simulation, one predicts the position and momentum space trajectories of a system of classical particles using the Newton laws of motion. The only required inputs are an atomic structure and an appropriate interatomic potential. Using the positions and momenta, it is possible to investigate thermal transport at the atomic level [14], and a variety of other problems, including, for example, molecular assembly, chemical reaction, and material fracture.

Early MD work focused on the fluid phase, and this is reflected in the contents of books written in the area (see, e.g. [15,16]). Only in the last 15 years has the solid state, and in particular, crystals (as opposed to amorphous materials), been studied extensively. This may be a result of the long correlation times that can exist in crystals. Extensive computational resources may be required to obtain sufficient data to observe trends in what might initially appear to be noisy data. Also, many solid state applications are concerned with electrons, which cannot be explicitly included in MD simulations. In the last five years, smaller system sizes and the associated high power densities have heightened interest in phonon thermal transport issues in semiconductor devices, and led to a significant increase in MD-related work. The analysis of new materials, such as carbon nanotubes, which are predicted to have very high thermal conductivities, has also motivated the development of the field.

1. *Simulation Setup*²

To perform an MD simulation, one first needs to specify the interatomic potential (referred to hereafter as simply the potential) that will be used to model the system of interest. The potential, ϕ , is an algebraic (or numerical) function used to calculate the potential energies and forces (through its derivative) associated with the particles in the system. It can include terms that account for two-body, three-body, etc. effects. Potentials can be obtained by fitting a chosen functional form to experimental data, or to the results of *ab initio* calculations. This process is not trivial.

The discussion here is left in terms of a general two-body (pair) potential, $\phi(r)$, where r is the distance between the two particles in question. In this case, the total potential energy in the system, Φ , is given by

$$\Phi = \sum_i \Phi_i = \frac{1}{2} \sum_i \sum_{i \neq j} \phi(r_{ij}) \quad (4)$$

where the summations are over the particles in the system,³ Φ_i is the potential energy associated with particle i , and the factor of one half accounts for double counting. It is more computationally efficient to calculate the total potential energy as

$$\Phi = \sum_i \sum_{j>i} \phi(r_{ij}) \quad (5)$$

² Much of the material in Sections III.A.1–III.A.3 is taken from Refs. [15] and [16]. Additional references from the literature are included where appropriate.

³ Where possible, i and j are used as indices for particle summations, and k is used for normal mode summations.

The total force on a particle i , \mathbf{F}_i , is given by

$$\mathbf{F}_i = \sum_{i \neq j} \mathbf{F}_{ij} = - \sum_{i \neq j} \frac{\partial \phi(r_{ij})}{\partial \mathbf{r}_{ij}} = - \sum_{i \neq j} \frac{\partial \phi(r_{ij})}{\partial r_{ij}} \frac{\partial r_{ij}}{\partial \mathbf{r}_{ij}} = - \sum_{i \neq j} \frac{\partial \phi(r_{ij})}{\partial r_{ij}} \hat{\mathbf{r}}_{ij} \quad (6)$$

where \mathbf{F}_{ij} is the force exerted on particle i by particle j , \mathbf{r}_{ij} the position vector between particles i and j ($= \mathbf{r}_i - \mathbf{r}_j$), and $\hat{\mathbf{r}}_{ij}$ the unit vector along \mathbf{r}_{ij} . Thus, for a pair potential, is \mathbf{F}_{ij} parallel to \mathbf{r}_{ij} .

All results of an MD simulation are, at their most fundamental level, related to the suitability of the chosen potential. Even if the potential is initially well formed, this does not guarantee good-quality predictions. For example, if a potential has been constructed using the experimental lattice constant and elastic constants for a crystal phase, should one expect it to properly model thermal transport, or the associated liquid phase, or a variation of the crystal structure? The answer, unfortunately, is maybe, but as potentials are difficult and time intensive to construct, one often proceeds with what is readily available in the literature, and hopes it will be suitable.

The contribution to the potential energy of an atom from other atoms beyond a radius R is given by approximately

$$\int_R^\infty 4\pi r^2 \phi(r) dr \quad (7)$$

where it is assumed that the system is spherically symmetric with the particles evenly distributed. This is a good assumption for fluids, and reasonable for solids beyond the fourth or fifth nearest neighbor. One can check the validity of this assumption by constructing the radial distribution function (RDF, see Section III.C.2). Many pair potentials are of the form r^{-n} , so that the energy given by Eq. (7) will be proportional to

$$\int_R^\infty r^{2-n} dr \quad (8)$$

which is bounded for $n > 3$. If this condition is satisfied, contributions to the potential energy of a particle from beyond a certain radius can be safely neglected. For computational efficiency, one can then apply a cutoff to the potential at a radius R_c . One should choose the cutoff so that the magnitude of the energy at the cutoff is small compared to the largest magnitude the energy can take on (i.e., the energy of a pair of nearest-neighbor atoms). To ensure that energy is conserved in the system, the potential must go to zero at the cutoff. This is accomplished by forming a shifted potential, $\phi_c(r)$, defined as

$$\phi_c(r) = \phi(r) - \phi(R_c) \quad (9)$$

Note that the forces are not affected [see Eq. (6)]. Other techniques for implementing the cutoff exist [17]. For the LJ work to be presented here, Eq. (9) is applied. When dealing with potentials that are not bounded, such as electrostatic interactions (where $\phi \sim 1/r$), applying a cutoff is not a well-defined operation. Instead, such potentials require special computational techniques such as the Ewald summation, the cell multipole method [18,19], or the Wolf (direct summation) method [20].

To obtain sufficient statistics for thermal transport calculations, simulations on the order of 1 ns may be required. Typically, systems with hundreds or thousands of atoms are considered. The actual number of atoms considered should be taken to be the smallest number for which there are no size effects. One should choose the time step so that all timescales of interest in the system can be resolved. In simulations of LJ argon, for example, where the highest frequency is 2 THz, a time step of 5–10 ps is typically chosen.

Using periodic boundary conditions and the minimum image convention allow for modeling of a bulk phase in an MD simulation. The idea is to reproduce the simulation cell periodically in space in all directions, and have a pair of particles only possibly interact between their images that are the closest together (i.e., a particle only interacts with another particle once). Success of this technique requires that the potential cutoff be no larger than one half of the simulation cell side length. In normal mode analysis or when calculating RMS displacements, one must carefully calculate displacements from equilibrium for the particles near the boundaries. In very large systems, where some particles will never interact with certain others, binning techniques and neighbor lists can significantly reduce computation times, and allow for the implementation of parallel MD code.

2. Energy, Temperature, and Pressure

The total system energy, E , is given by $\Phi + KE$, where KE is the total kinetic energy. The potential energy is given by Eq. (5). The kinetic energy is

$$KE = \sum_i \frac{1}{2} \frac{|\mathbf{p}_i|^2}{m_i} \quad (10)$$

where \mathbf{p}_i and m_i are the momentum vector and mass of particle i . From kinetic theory, the expectation value of the energy of one degree of freedom is $k_B T/2$, where k_B is the Boltzmann constant. The expectation value of the kinetic energy of one atom is $3k_B T/2$ (based on the three degrees of freedom associated with the momentum). The temperature of the MD system can be obtained by equating the average kinetic energy with that predicted from

kinetic theory, such that

$$T = \frac{\langle \sum_i |\mathbf{p}_i|^2 / m_i \rangle}{3(N-1)k_B} \quad (11)$$

where N is the total number of atoms in the system. $3(N-1)$ degrees of freedom have been used in Eq. (11) as the MD simulation cell is assumed to be fixed in space (i.e., the total linear momentum is set to zero, removing three degrees of freedom). One should only use the expression for the temperature given by Eq. (11) with the expectation value of the kinetic energy (i.e., the temperature cannot really be defined at an instant in time). For the purpose of temperature control, however, it is assumed that the instantaneous temperature is a well-defined quantity.

When working in the canonical (NVT) ensemble, where the independent variables are the system mass, volume (V), and temperature, it is also possible to calculate the temperature based on the fluctuations of the total system energy as

$$T = \left[\frac{\langle (E - \langle E \rangle)^2 \rangle}{3(N-1)k_B c_v} \right]^{1/2} \quad (12)$$

where c_v is the specific heat per mode (J/K). The temperature defined as such can only be evaluated as an ensemble average. Similar expressions can be derived for different ensembles [21].

The pressure, P , of the system can be calculated from

$$P = \frac{Nk_B T}{V} + \frac{1}{3V} \langle \sum_i \sum_{j>i} r_{ij} \cdot \mathbf{F}_{ij} \rangle \quad (13)$$

which is based on the virial equation for the pressure. The temperature is calculated from Eq. (11). As with the temperature, this quantity should, in theory, only be calculated as an ensemble average. For the purposes of pressure control, however, it is assumed to be valid at an instant in time.

3. Equations of Motion

The equations of motion to be used in an MD simulation are dependent on which thermodynamic ensemble one wishes to model. The most natural ensemble is the NVE (microcanonical), where the independent variables are mass, volume, and energy. In this case, the equations of motion for a particle i are

$$\frac{d\mathbf{r}_i}{dt} = \frac{\mathbf{p}_i}{m_i} \quad (14)$$

$$\frac{d\mathbf{p}_i}{dt} = \mathbf{F}_i \quad (15)$$

To implement these equations in the MD simulations, they must be discretized. Different schemes are available for this procedure, which have varying levels of accuracy and computational requirements. While some higher-order approaches allow for the use of long-time steps (e.g., the Gear predictor–corrector method), if the dynamics of the system are of interest these may be computationally inefficient. When a small time step is needed, a scheme such as the Verlet leapfrog algorithm is suitable.

To reproduce the canonical ensemble, the temperature must be controlled with a thermostat. Rescaling the velocities at every time step to get the desired temperature is a straightforward method. This approach, however, does not reproduce the temperature fluctuations associated with the NVT ensemble [21]. Allowing the MD system to interact with a thermal reservoir at constant temperature is another possibility. To do so, the equations of motion are modified with a damping parameter η such that

$$\frac{d\mathbf{r}}{dt} = \frac{\mathbf{p}_i}{m_i} \quad (16)$$

$$\frac{d\mathbf{p}_i}{dt} = \mathbf{F}_i - \eta\mathbf{p}_i \quad (17)$$

The damping parameter changes in time according to

$$\frac{d\eta}{dt} = \frac{1}{\tau_T^2} \left(\frac{T}{T_{set}} - 1 \right) \quad (18)$$

where τ_T is the reservoir-system time constant and T_{set} the desired temperature. This is the Nose–Hoover thermostat [22–24], which produces the appropriate temperature fluctuations, and reduces to the NVE ensemble when η is set to zero. When the system temperature is above that desired, η is positive, and kinetic energy is removed from the system. When the system temperature is below the desired value, η will be negative, leading to an increase of the system kinetic energy. By setting η to be positive and constant, energy can be continually removed from the system. This concept can be used to simulate a quench from a liquid state to a solid state, possibly forming an amorphous phase, or to obtain the zero-temperature structure. The thermostat time constant determines the strength of the coupling between the MD system and the thermal reservoir. If τ_T is very large, the response of the MD system will be slow. The limit of $\tau_T \rightarrow \infty$ corresponds to the NVE ensemble. One should choose the time constant to reproduce the temperature as defined in the NVT ensemble [Eq. (12)]. From a dynamics standpoint, the equations of motion in the NVT ensemble have been

modified in a nonphysical manner. Thus, one must use caution when extracting dynamical properties from a canonical MD system. Static properties (those not based on the time progression of quantities, but on their average values, such as the zero-pressure unit cell) are not affected.

To simulate the *NPT* ensemble, where the independent variables are the system mass, pressure, and temperature, the system volume must be allowed to change (i.e., a barostat is implemented). Simulations in this ensemble are useful for determining pressure-dependent cell sizes for use in either the *NVE* or *NVT* ensembles. Numerous techniques exist with modified equations of motion, notably those of Anderson [25], and Parrinello and Rahman [26].

4. Initialization

It is easiest to initialize the particle positions based on their equilibrium locations in a known solid state (be it an amorphous phase or a crystal). Such an initialization is also appropriate for a fluid, as the temperatures to be studied will quickly induce melting. If the particles are placed in their equilibrium positions each will experience no net force. For something to happen the initial momenta must be nonzero, so as to move the system away from equilibrium. A convenient method is to give each atom an extremely small, but nonzero, random momentum and then initially run the simulation in the *NVT* ensemble to obtain the desired temperature. If post-processing of the positions and momenta into normal mode coordinates is required, starting as such is beneficial as the equilibrium positions are exactly known. Many thermal properties require averaging over multiple simulations. One can initialize distinct simulations with the same independent variables by the initial momenta distribution. At equilibrium, the momenta of the particles will take on a Maxwell–Boltzmann distribution. Sufficient time must be given for this to occur. In the LJ case study reported here, at least 10^5 time steps are taken for all reported results. One could also initialize the momenta in the Maxwell–Boltzmann distribution.

To determine the equilibrium unit cell size at a specified temperature and pressure, simulations can be run in the *NPT* ensemble. A few hundred thousand time steps should be sufficient to generate enough data for a good average. The average potential energy of the system as a function of temperature can also be determined from the simulations. To set the temperature for runs in the *NVE* ensemble, we suggest the following scheme. The system is first run in the *NVT* ensemble until the momenta are properly initialized. The potential energy of the system is then monitored at every time step. When it reaches a value within $10^{-4}\%$ of the desired potential energy as calculated from the *NPT* simulations, the ensemble is switched to *NVE*, and the velocities are scaled to the desired temperature. This

procedure is less invasive than other temperature-setting techniques such as velocity scaling, as the particles are allowed to move within the equations of motion for a given ensemble at all times other than when the switch occurs. In the *NVE* ensemble, the total energy is a function of temperature. By simply setting the kinetic energy to a specific value without considering the potential energy, one will not achieve the desired temperature unless the potential energy at that time has its average value.

B. LENNARD-JONES SYSTEM

To begin the presentation of what MD simulations can reveal about the nature of atomic-level thermal transport in dielectrics, we consider materials described by the LJ potential. Choosing a simple system allows for the elucidation of results that may be difficult to resolve in more complex materials, where multi-atom unit cells (and thus, optical phonons) can generate additional effects. The LJ atomic interactions are described by the pair potential [3]

$$\phi_{LJ,ij}(r_{ij}) = 4\epsilon_{LJ} \left[\left(\frac{\sigma_{LJ}}{r_{ij}} \right)^{12} - \left(\frac{\sigma_{LJ}}{r_{ij}} \right)^6 \right] \quad (19)$$

The depth of the potential energy well is ϵ_{LJ} , and corresponds to an equilibrium particle separation of $2^{1/6}\sigma_{LJ}$. The LJ potential describes the noble elements well, and is plotted in dimensionless form in Fig. 3.

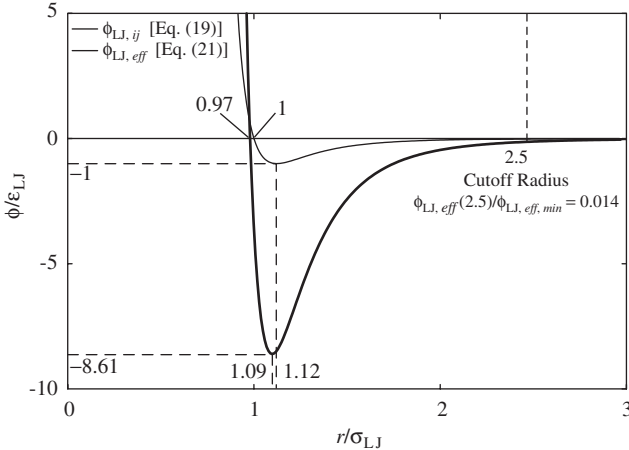


FIG. 3. A dimensionless plot of the LJ potential. Both the pair [Eq. (19)] and effective [Eq. (21)] curves are shown, along with the values of the energy and separation distance at important points.

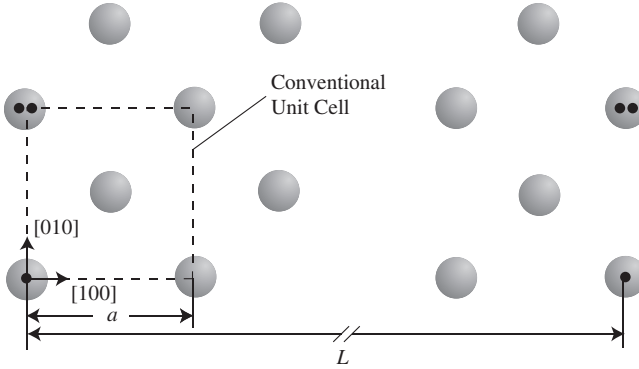


FIG. 4. A plane in the fcc crystal. The atoms with black dots are equivalent through the use of periodic boundary conditions.

Argon, for which σ_{LJ} and ε_{LJ} have values of 3.40×10^{-10} m and 1.67×10^{-21} J [3], is chosen for the current investigation. The fcc crystal, amorphous, and liquid phases are considered. The plane formed by the $[100]$ and $[010]$ axes in the crystal is shown in Fig. 4. In the figure, a is the side length of the conventional unit cell (which contains four atoms) and L the side length of the simulation cell (which is taken to be cubic). This leads to $\eta = L/a$ unit cells in each of the $[100]$, $[010]$, and $[001]$ directions, and $N = 4\eta^3$ total atoms. Here, values of η of 4, 5, and 6 are considered, which correspond to 256, 500, and 864 total atoms. The true fcc unit cell, containing one atom, is rhombohedral, and not as suitable for analysis.

Unless noted, all reported data correspond to simulations of the 256 atom unit cell in the NVE ensemble at zero pressure with a time step of 4.285 fs (0.002 LJ units) [11,27,28]. This time step sufficiently resolves the phenomena of interest [e.g., the smallest timescale of interest in the heat current (see Section V) is about 20 time steps]. In similar simulations, Kaburaki *et al.* [29] found good agreement between the fcc crystal thermal conductivities predicted from cells containing 256 and 500 atoms. Tretiakov and Scandolo [30] found no size effects in simulation cells with as few as 128 atoms. Periodic boundary conditions are imposed in all directions. The equations of motion are integrated with a Verlet leapfrog algorithm. The atomic interactions are truncated and shifted at a cutoff radius equal to $2.5\sigma_{LJ}$. For the fcc crystal, temperatures between 10 and 80 K are considered in 10 K increments. Melting occurs at a temperature of 87 K. The amorphous phase is generated by starting with the desired number of atoms placed on an fcc lattice, running at a temperature of 300 K for 10^4 time steps to eliminate any memory of the initial configuration, and then quenching at 8.5×10^{11} K/s back to a temperature of 10 K. The amorphous

phase is stable up to a temperature of 20 K. Above this point, the equilibrium thermal fluctuations in the system are large enough to return the atoms to the fcc crystal structure. This is consistent with the findings of Li [17]. Temperatures of 10, 15, and 20 K are considered. Three different amorphous phases (each with 250 atoms) were formed to check if the systems are truly disordered, and cells with 500 and 1000 atoms were created to investigate size effects. The liquid phase is obtained by first heating the 256 atom crystal phase to a temperature of 100 K to induce melting, then lowering the temperature. Using this approach, a stable liquid is found to exist at temperatures as low as 70 K. Owing to the small length and timescales used (necessary for reasonable computational times), the melting/solidifying temperature is not well defined, and it is possible to have stable fcc crystal and liquid phases at the same temperature and pressure, although the densities differ. Temperatures of 70, 80, 90, and 100 K are considered for the liquid simulations.

C. REAL SPACE ANALYSIS

1. Prediction of System Parameters from Lennard-Jones Potential

a. Unit Cell Size. When relaxed to zero temperature, the MD fcc crystal unit cell parameter, a (the lattice constant), is 5.2686 Å. The experimental value for argon is 5.3033 Å [3]. Li [17] has found values of 5.3050 Å for a cutoff radius of $2.5\sigma_{LJ}$, and 5.2562 Å for a cutoff radius of $5\sigma_{LJ}$. The discrepancy between the current result and that of Li can be attributed to differences in how the potential energy and force are cutoff. Whenever performing simulations, the question often arises of whether or not one should strive to match certain experimental parameters (such as the lattice constant). For the LJ argon system, this can be done by choosing a cutoff radius of about $3\sigma_{LJ}$. This by no means, however, guarantees that agreement with experimental data for the temperature dependence of the unit cell size, or other properties (e.g., elastic constant, thermal conductivity, etc.) will follow. The other option is to choose suitable simulation parameters and strive for consistency. These can be chosen based on previous work, to allow for comparison-making. The choice of a cutoff of $2.5\sigma_{LJ}$, used here, is standard.

The lattice constant can be predicted from the analytical form of the LJ potential. To do this, one must consider the total potential energy associated with one atom, Φ_i . If the energy in each pair interaction is assumed to be equally distributed between the two atoms, Φ_i will be given by

$$\Phi_i = \frac{1}{2} \sum_{i \neq j} \phi_{LJ,ij} \quad (20)$$

which for the fcc crystal lattice can be expressed as [3]

$$\Phi_i = 2\varepsilon_{LJ} \left[A_{12} \left(\frac{\sigma_{LJ}}{r_{mn}} \right)^{12} - A_6 \left(\frac{\sigma_{LJ}}{r_{mn}} \right)^6 \right] \equiv \phi_{LJ,eff} \quad (21)$$

where A_{12} and A_6 have values of 12.13 and 14.45, respectively, and r_{mn} is the nearest neighbor (mn) separation. This effective LJ potential is plotted in Fig. 3 alongside the pair potential, given by Eq. (19). By setting

$$\frac{\partial \Phi_i}{\partial r_{mn}} = 0 \quad (22)$$

the equilibrium value of r_{mn} is found to be

$$r_{mn,eq} = \left(\frac{2A_{12}}{A_6} \right)^{1/6} \sigma_{LJ} = 1.09\sigma_{LJ} \quad (23)$$

The location of the minimum is slightly shifted from that in the pair potential, and the energy well is deeper and steeper. For argon, the equilibrium separation of Eq. (23) corresponds to a unit cell parameter of 5.2411 Å, which agrees with the zero temperature MD result to within 0.6%.

b. Period of Atomic Oscillation and Energy Transfer. In a simplified, real space model of atomic-level behavior, the energy transfer between neighboring atoms can be assumed to occur over one half of the period of oscillation of an atom [31–33]. The associated time constant, τ_D , can be estimated from the Debye temperature, T_D , as

$$\tau_D = \frac{2\pi\hbar}{2k_B T_D} \quad (24)$$

where \hbar is the Planck constant divided by 2π . The factor of 2 in the denominator is included as one half of the period of oscillation is desired. By fitting the specific heat (as predicted by the MD zero-temperature phonon density of states, see Section III.D.3) to the Debye model using a least-square method, the Debye temperature is found to be 81.2 K. This compares well with the experimental value of 85 K [3]. The MD result is used in subsequent calculations, and gives a τ_D value of 0.296 ps (~ 69 time steps).

Using the LJ potential, an estimate of this time constant can also be made. The time constant is related to the curvature of the potential well that an atom experiences at its minimum energy. Assuming that the potential is harmonic at the minimum, the natural angular frequency, ω , of the atom will be given by

$$\omega = \left(\frac{1}{m} \frac{\partial^2 \Phi_i}{\partial r_{mn}^2} \Big|_{r_{mn}=r_{mn,eq}} \right)^{1/2} = 22.88 \left(\frac{\varepsilon_{LJ}}{\sigma_{LJ}^2 m} \right)^{1/2} \quad (25)$$

where m is the mass of one atom, which for argon is 6.63×10^{-26} kg, and Φ_i and $r_{m, equ}$ are taken from Eqs. (21) and (23). One half of the period of oscillation is then

$$\tau_{LJ} = \frac{1}{2} \frac{2\pi}{\omega} = 0.137 \left(\frac{\sigma_{LJ}^2 m}{\epsilon_{LJ}} \right)^{1/2} \quad (26)$$

which evaluates to 0.294 ps, within 1% of τ_D .

One can further investigate the physical significance of this time constant by considering the flow of energy between atoms in the MD simulation cell [27,34]. This is done by constructing energy correlation functions between an atom and its 12 nearest neighbors. The calculations are based on the deviations of the particle energies from their mean values. As all the atoms in the fcc crystal simulation cell are at equivalent positions, the results can be averaged over neighbors, space, and time. The resulting correlations for the fcc crystal are shown in Fig. 5 for all temperatures considered. In the figure, E denotes the particle energy, and the subscripts o and nm refer to a particle and one of its nearest neighbors. The curves are normalized against their zero time value to allow for comparison between the different temperatures. The first peak locations are denoted as τ_{nm} . The value of τ_{nm} increases with temperature, which is due to the decreasing density. As the

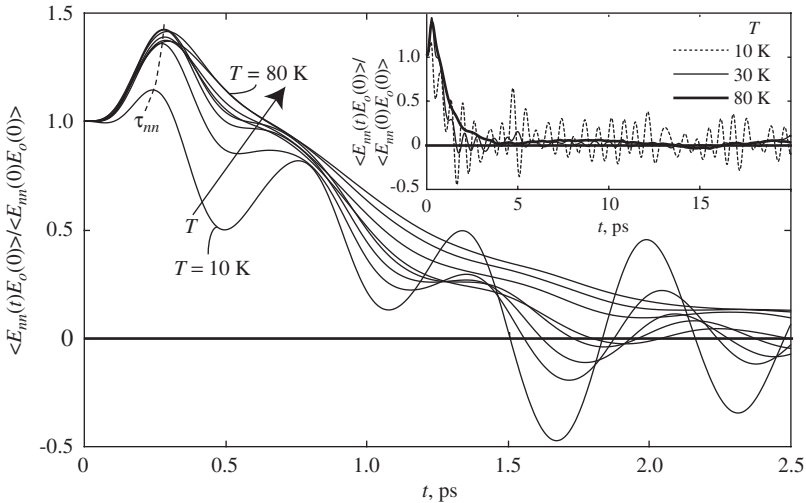


FIG. 5. Nearest-neighbor particle-particle energy correlation functions for the LJ fcc crystal. The energy data correspond to deviations from the mean values. A longer time scale is shown for $T = 10, 30,$ and 80 K in the inset plot, where the decrease in the long time coherence at higher temperatures is evident.

atomic separation increases, it takes longer to transfer energy between two atoms. Except at a temperature of 10 K, the time constants τ_D , τ_{LJ} , and τ_{nn} agree to within 10%.

Ohara [35] has developed a technique in the same spirit for investigating the flow of energy between atoms in an MD simulation, and applied it to an LJ argon fluid. The technique does not involve correlation functions as described here, but instead looks at the time rate of energy change between pairs of atoms.

2. Lennard-Jones Phase Comparisons

The densities and potential energies per particle of the zero pressure LJ fcc crystal, liquid, and amorphous phases are plotted as a function of temperature in Figs. 6(a) and (b). As would be expected, the crystal phase has the lowest potential energy at a given temperature. Note the consistent trend between the amorphous and liquid phases in both density and potential energy. This is consistent with the idea of an amorphous phase being a fluid with a very high viscosity.

The RDF, $g(r)$, describes the distribution of the atoms in a system from the standpoint of a fixed, central atom. Its numerical value at a position r is the probability of finding an atom in the region $r-dr/2 < r < r+dr/2$ divided by the probability that the atom would be there in an ideal gas [i.e., $g(r) = 1$ implies that the atoms are evenly distributed]. The calculation includes no directional dependence. The Fourier transform of the RDF is the structure factor, which can be determined from scattering experiments. The RDFs for the fcc crystal at temperatures of 20, 40, 60, and 80 K, the amorphous phase at a temperature of 10 K, and the liquid phase at temperatures of 70 and 100 K are shown in Fig. 7. The results presented are based on 10^5 time steps of *NVE* simulation, with data extracted every five time steps. The RDF is calculated with a bin size of 0.034 \AA for all atoms at each time step, then averaged over space and time. The RDF can only be determined up to one half of the simulation cell size, which here is about $3.25\sigma_{LJ}$ for the solid phases, and slightly larger for the liquid.

The RDF of the fcc crystal phase shows well-defined peaks that broaden as the temperature increases, causing the atomic displacements to grow. Each peak can be associated with a particular set of nearest-neighbor atoms. The locations of the peaks shift to higher values of r as the temperature increases and the crystal expands. In the amorphous phase, the first peak is well defined, but after that, the disordered nature of the system leads to a much flatter RDF. There is no order beyond a certain point. The splitting of the second peak is typical of amorphous phases, and consistent with the results of Li for LJ argon [17]. The presence of only short-range order is also

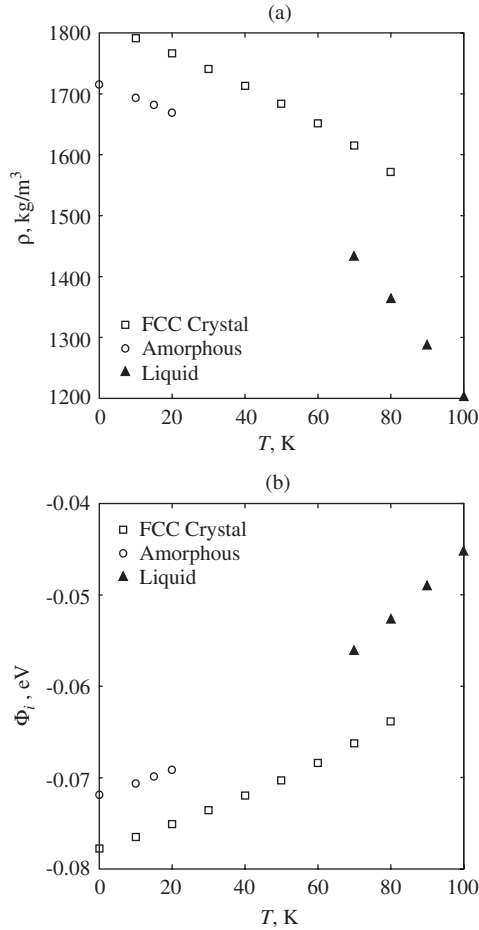


FIG. 6. Temperature dependencies of the LJ phase (a) densities and (b) per particle potential energies.

true for the liquid phase, where only the first neighbor peak is well defined. Since the physical size of the atoms defines the minimum distance over which they may be separated, this is expected.

The RMS displacement, $\langle |\mathbf{u}_i|^2 \rangle^{1/2}$, where \mathbf{u}_i is the displacement of atom i from its equilibrium position, of the atoms in the fcc crystal is shown as a function of temperature in Fig. 8. The results presented are based on 10^5 time steps of NVE simulation, with data extracted every five time steps. The RMS displacement can be predicted from a quantum-mechanical

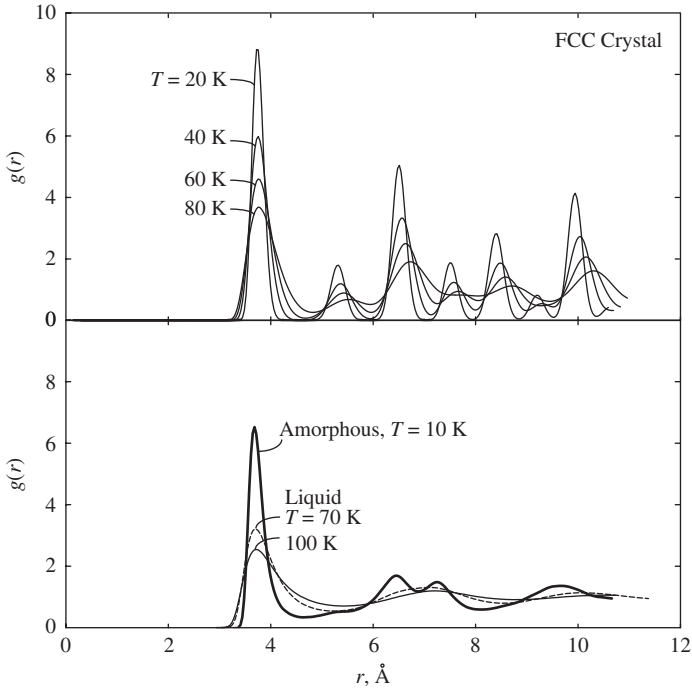


FIG. 7. Lennard-Jones RDFs for the fcc crystal at $T = 20, 40, 60,$ and 80 K, the amorphous phase at $T = 10$ K, and the liquid phase at $T = 70$ and 100 K.

description of the system under the Debye approximation as [36]

$$\langle |\mathbf{u}_i|^2 \rangle^{1/2} = \left\{ \frac{3\hbar}{m\omega_D} \left[\frac{1}{4} + \left(\frac{T}{T_D} \right)^2 \int_0^{T_D/T} \frac{x dx}{\exp(x) - 1} \right] \right\}^{1/2} \quad (27)$$

where $\omega_D = k_B T_D / \hbar$. This relation is also shown in Fig. 8. Considering the minimal input required in the theoretical model (only the atomic mass and the Debye temperature), the agreement between the two curves is fair. Note that while the quantum model predicts the finite zero-point motion $(3\hbar/4m\omega_D)^{1/2}$, the MD results show a trend toward no motion at zero temperature. One expects this in a classical system, as the phase space approaches a single point when motion ceases.

The specific heat is defined thermodynamically as the rate of change of the total system energy (kinetic and potential) as a function of temperature at

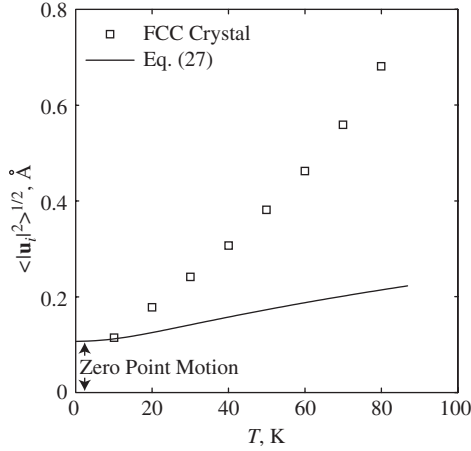


FIG. 8. Face-centered cubic crystal RMS data, and comparison to Eq. (27), a quantum-mechanical prediction. The zero-point RMS value is $(3\hbar/4m\omega_D)^{1/2}$.

constant volume [3],

$$c_v = \left. \frac{\partial E}{\partial T} \right|_V \quad (28)$$

Such a calculation can be explicitly performed using the results of MD simulations. The predicted specific heats for the fcc crystal, amorphous, and liquid phases are plotted in Fig. 9. The values given correspond to the specific heat per mode (i.e., per two degrees of freedom), of which there are $3(N-1)$. The calculation is performed by varying the temperature in 0.1 K increments over a ± 0.2 K range around the temperature of interest. Five simulations are performed at each of the five increments, with energy data averaged over 3×10^5 time steps. The resulting 25 data points are fit with a linear function, the slope of which is the specific heat. For the fcc crystal at temperatures of 70 and 80 K, and for all liquid phase calculations, 10 simulations were performed at all of the temperature increments due to larger scatter in the data. The spread of the energy data in these calculations increases with increasing temperature. The overall trends are good though, so any errors present are not likely more than 1% (based on linear fits to the data). The specific heat can also be predicted from system fluctuations (energy or temperature, depending on the ensemble), which are easily accessed in the simulations.

Not surprisingly, the fcc crystal and amorphous data are close. The crystal structure should not significantly affect the specific heat, especially at

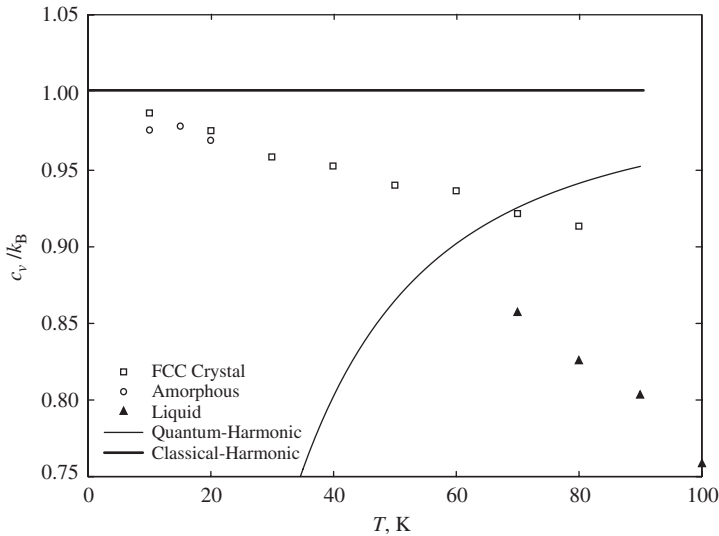


FIG. 9. The classical-anharmonic specific heat per degree of freedom predicted from the MD simulations, and the classical- and quantum-harmonic curves for the crystal phase (all scaled by k_B). The theoretical predictions are stopped at a temperature of 87 K, the melting point of the MD system.

low temperatures, where the harmonic approximation is still reasonable. There is a definite drop in the liquid values, and the specific heat would continue to decrease as the temperature is increased. The lower limit for the specific heat per mode is $0.5k_B$, when potential energy effects have been completely eliminated (i.e., an ideal gas).

The specific heat predicted from the MD simulations is a classical-anharmonic value. Also shown in Fig. 9 are the classical- and the quantum-harmonic specific heats for the crystal phase. The classical-harmonic specific heat, k_B , is based on an assumption of equipartition of kinetic and potential energy between the degrees of freedom. The equipartition assumption is always valid for the kinetic energy (i.e., it contributes $k_B/2$ to c_v , which has been verified). For the potential energy, however, it is only true under the harmonic approximation, which itself is only valid at zero temperature (this is discussed in Section III.D.1). The deviations of the classical anharmonic results from the classical harmonic model are significant. It is sometimes assumed that the mode specific heat of solids in MD is equal to k_B , which is not the case, and will lead to errors at high temperatures. The quantum-harmonic specific heat is based on the zero-temperature phonon density of states (calculated with normal mode analysis as discussed in Section III.D.3)

and is given by [37]

$$c_{v,quant-harm} = k_B \sum_k \frac{x_k^2 \exp(x_k)}{[\exp(x_k) - 1]^2} \quad (29)$$

where x_k is $\hbar\omega_k/k_B T$, and the summation is over the normal modes of the system. As expected, the classical and harmonic specific heats are significantly different at low temperatures, where quantum effects are important. Prediction of the quantum-anharmonic specific heat (that which would be measured experimentally) would require the temperature dependence and coupling of the normal modes into account. The results would be expected to converge with the classical-anharmonic value at high temperatures (i.e., on the order of the Debye temperature).

D. PHONON SPACE ANALYSIS

1. Harmonic Approximation

One foundation of phonon analysis is the harmonic approximation (i.e., that the phonon modes are equivalent to independent harmonic oscillators). Even when anharmonicities are accounted for, it is usually as a perturbation to the harmonic solution of the lattice dynamics problem. In these cases, phonon-phonon interactions are modeled as instantaneous events, preceded and followed by the independent propagation of phonons through the system (i.e., the phonons behave harmonically except when they are interacting). In this section, we briefly review the harmonic description of the lattice dynamics, and present calculations on the zero-temperature unit cell. A discussion follows of how MD simulations can be used to incorporate anharmonic effects.

At zero temperature in a classical solid, all the atoms are at rest in their equilibrium positions. This is evident from the trend in the atomic RMS data shown in Fig. 8. The potential energy of the system, which is a function of the atomic positions, can only take on one value (i.e., the phase space consists of a single point). As the temperature of the system is raised, the atoms start moving, and the extent of the associated phase space increases.

In lattice dynamics calculations, a frequency space description is sought through which one can predict and analyze the motions of the atoms. Instead of discussing the localized motions of individual atoms, one describes the system by energy waves with given wave vector ($\mathbf{\kappa}$), frequency (ω), and polarization vector (\mathbf{e}). The formulation of lattice dynamics theory is described in detail in numerous books (see, e.g. [3–6]). Here, we will discuss a few specific points of interest.

Suppose that the equilibrium zero-temperature potential energy of a system with N atoms is given by Φ_0 . If each atom i is moved by an amount \mathbf{u}_i , the resulting energy of the system, Φ , can be found by expanding around

the equilibrium energy with a Taylor series as

$$\begin{aligned} \Phi = \Phi_0 &+ \sum_i \sum_\alpha \left. \frac{\partial \Phi}{\partial u_{i,\alpha}} \right|_0 u_{i,\alpha} + \frac{1}{2} \sum_{i,j} \sum_{\alpha,\beta} \left. \frac{\partial^2 \Phi}{\partial u_{i,\alpha} \partial u_{j,\beta}} \right|_0 u_{i,\alpha} u_{j,\beta} \\ &+ \frac{1}{6} \sum_{i,j,k} \sum_{\alpha,\beta,\gamma} \left. \frac{\partial^3 \Phi}{\partial u_{i,\alpha} \partial u_{j,\beta} \partial u_{k,\gamma}} \right|_0 u_{i,\alpha} u_{j,\beta} u_{k,\gamma} + \dots \end{aligned} \quad (30)$$

Here, the i , j , and k sums are over the atoms in the system, and the α , β , and γ sums are over the x -, y -, and z -directions. Both Φ and Φ_0 are only functions of the atomic positions. The first derivative of the potential energy with respect to each of the atomic positions is the negative of the net force acting on that atom. Evaluated at equilibrium, this term is zero. Thus, the first non-negligible term in the expansion is the second-order term. The harmonic approximation is made by truncating the Taylor series at the second-order term. The $\partial^2 \Phi / \partial u_{i,\alpha} \partial u_{j,\beta}$ terms are the elements of the force constant matrix.

The harmonic approximation is valid for small displacements ($u_{i,\alpha} \ll r_m$) about the zero-temperature minimum. Raising the temperature will cause deviations for two reasons: as the temperature increases, the displacements of the atoms will increase beyond what might be considered small (say, $0.05r_m$), and the lattice constant will change, so that the equilibrium separation does not correspond to the well minimum. These two ideas can be illustrated using results of the MD simulations for the LJ fcc crystal.

The effective LJ potential (that which an atom experiences in the crystal) is given by Eq. (21). The area around the minimum is plotted in Fig. 10. Superimposed on the potential is the associated harmonic approximation, given by

$$\phi_{LJ,eff,harm} = -8.61 \varepsilon_{LJ} + 260.67 \frac{\varepsilon_{LJ}}{\sigma_{LJ}^2} (r_m - 1.09 \sigma_{LJ})^2 \quad (31)$$

The match between the harmonic curve and the effective potential, reasonable to the left of the minimum, is poor to its right. Also shown in Fig. 10 are the equilibrium atomic separations (equal to the lattice constant a divided by $2^{1/2}$, see Fig. 4) and the distribution of the nearest-neighbor atomic separations at temperatures 20, 40, 60, and 80 K. The distributions are based on 10^5 time steps of NVE simulation with data extracted every five time steps, and the probability density function $p(r)$ is defined such that $\int p(r) dr = 1$.

The crystal expands as the temperature increases. The sign of the thermal expansion coefficient for a solid is related to the asymmetry of the potential

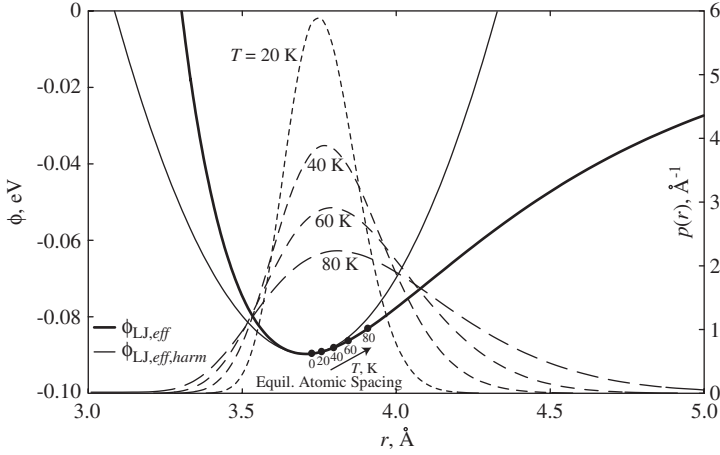


FIG. 10. The effective LJ potential, the associated harmonic approximation, and the resulting atomic separations at temperatures of 20, 40, 60, and 80 K for the fcc crystal.

well. At very low temperatures, this effect can be quantitatively related to the third-order term in the expansion of the potential energy [38]. For the LJ system, and most other solids, the potential is not as steep as the atomic separation is increased, leading to an expansion of the solid with increasing temperature. This is not always the case, however, as materials with a negative coefficient of thermal expansion exist (e.g., some zeolites [39], cuprous oxide [40], and ZrW_2O_8 [41]). As the temperature is raised, the spread of the nearest neighbor separation distance increases, and the distribution becomes significantly asymmetrical. This effect can also be interpreted based on the shape of the potential well.

For the case of the LJ system, it is clear that the harmonic approximation is not strictly valid, even at the lowest temperature considered (10 K). In order to work with phonons and normal modes, however, the harmonic approximation is necessary.

2. Normal Modes

A challenge in working with Eq. (30) under the harmonic approximation is the coupling of the atomic coordinates in the second-order derivatives. A transformation exists on the $3N$ real space coordinates (three for each of the N atoms) to a set of $3N$ new coordinates S_k (the normal modes) such that [5]

$$\Phi - \Phi_0 = \frac{1}{2} \sum_{i,j} \sum_{\alpha,\beta} \left. \frac{\partial^2 \Phi}{\partial u_{i,\alpha} \partial u_{j,\beta}} \right|_0 u_{i,\alpha} u_{j,\beta} = \frac{1}{2} \sum_k \left. \frac{\partial \Phi^2}{\partial S_k^2} \right|_0 S_k^* S_k \quad (32)$$

The normal modes are equivalent to harmonic oscillators, each of which has an associated wave vector, frequency, and polarization. They are completely nonlocalized spatially. The specification of the normal modes (which is based on the crystal structure and system size) is known as the first quantization. It is not related to quantum mechanics, but indicates that the frequencies and wave numbers available to a crystal are discrete and limited. This idea can be understood by considering a one-dimensional arrangement of four atoms in a periodic system, as shown in Fig. 11. The atoms marked with black dots are equivalent as a result of the application of periodic boundary conditions, which any allowed vibrational mode must satisfy. Two such waves are shown, with wavelengths of $4a$ and $2a$. An important distinction between the lattice dynamics problem and the solution of a continuum system (e.g., elastic waves) is that the smallest allowed wavelength is restricted by the spacing of the atoms. A mode with a wavelength of a will be indistinguishable from the mode with wavelength $2a$. The minimum wavelength (i.e., the maximum wave number) defines the extent of the first Brillouin zone (BZ), the frequency space volume accessed by the system. There is no lower limit to the wavelength in a continuum. The longest allowed wavelength in any case is determined by the size of the system.

By introducing the idea of a quantum harmonic oscillator, the second quantization is made. In this case, in addition to quantizing the allowed normal modes, the energy of these modes is also quantized in units of $\hbar\omega$. The second quantization cannot be made in MD simulation due to their classical nature. The energy of a given mode is continuous.

Starting from Eq. (32), and noting that the second derivative terms can be considered as the spring constants, K_k , of the harmonic oscillators, the

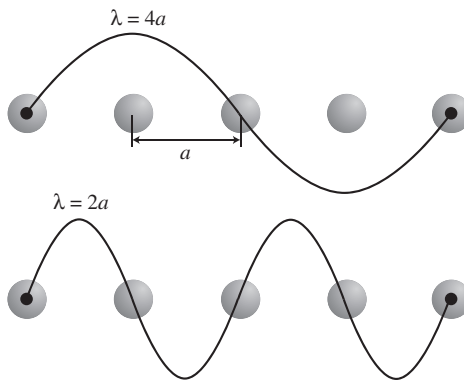


FIG. 11. One-dimensional example of how allowed wave vectors are determined and the first quantization is realized.

energy of one normal mode can be expressed as

$$\Phi_k = \frac{1}{2} \frac{\partial \Phi^2}{\partial S_k^2} \Big|_0 S_k^* S_k = \frac{1}{2} \frac{K_k}{m_k} S_k^* S_k = \frac{1}{2} \omega_k^2 S_k^* S_k \quad (33)$$

as the mass, frequency, and spring constant are related through $\omega_k = (K_k/m_k)^{1/2}$. The average potential energy will be

$$\langle \Phi_k \rangle = \frac{1}{2} \omega_k^2 \langle S_k^* S_k \rangle \quad (34)$$

This is the expectation value of the potential energy of one degree of freedom. The expectation value for one degree of freedom in a classical-harmonic system is $k_B T/2$.

The total kinetic energy, KE , in the real and normal mode spaces is given by

$$KE = \sum_i \frac{1}{2} \frac{|\mathbf{p}_i|^2}{m_i} = \sum_k \frac{1}{2} S_k^* S_k \quad (35)$$

As the kinetic energy of a particle in a classical system is proportional to the square of the magnitude of its velocity (and no higher order terms), this expression for the kinetic energy is valid in anharmonic systems. The classical-harmonic expectation value of the mode kinetic energy is $k_B T/2$ leading to a contribution of $k_B/2$ to the mode specific heat, as discussed in Section III.C.2.

In a classical-harmonic system there is an equipartition of energy between all degrees of freedom, so that the average kinetic energy of a mode will be equal to its average potential energy. Thus,

$$\langle E_k \rangle_{\text{harm}} = \omega_k^2 \langle S_k^* S_k \rangle = k_B T \quad (36)$$

The instantaneous energy in a given mode is readily calculated in the MD simulations. It is crucial to note, however, that while these expressions are based on a harmonic theory, the MD simulations are anharmonic. We will discuss some of the consequences of this fact in Section III.D.5.

3. Lattice Dynamics

Given the crystal structure of a material, the determination of the allowed wave vectors (whose extent in the wave vector space make up the first BZ) is straightforward. One must note that points on the surface of the BZ that are separated by a reciprocal lattice vector, \mathbf{G} , are degenerate. For the fcc

crystal, the reciprocal lattice vectors are $2\pi/a(2,0,0)$, $2\pi/a(1,1,1)$, and appropriate rotations. For the 256 atom fcc crystal, application of the degeneracies reduces 341 points down to the expected 256, each of which has three polarizations [11]. Specifying the frequencies and polarizations of these modes is a more involved task. The polarizations are required to transform the atomic positions into the normal mode coordinates, and the frequencies are needed to calculate the normal mode potential energies [Eq. (33)]. We outline the derivation presented by Dove [5].

Consider a general crystal with an n -atom unit cell, such that the displacement of the j th atom in the l th unit cell is denoted by $\mathbf{u}(jl, t)$. The force constant matrix [made up of the second order derivatives in Eq. (30)] between the atom (jl) and the atom ($j'l'$) will be denoted by $\Phi \begin{pmatrix} jj' \\ ll' \end{pmatrix}$. Note that this matrix is defined for all atom pairs, including the case of $j = j'$ and $l = l'$. Imagining that the atoms in the crystal are all joined by harmonic springs, the equation of motion for the atom (jl) can be written as

$$m_j \ddot{\mathbf{u}}(jl, t) = - \sum_{j'l'} \Phi \begin{pmatrix} jj' \\ ll' \end{pmatrix} \cdot \mathbf{u}(j'l', t) \quad (37)$$

Now assume that the displacement of an atom can be written as a summation over the normal modes of the system, such that

$$\mathbf{u}(jl, t) = \sum_{\kappa, \nu} m_j^{-1/2} \mathbf{e}(j, \kappa, \nu) \exp\{i[\boldsymbol{\kappa} \cdot \mathbf{r}(jl) - \omega(\kappa, \nu)t]\} \quad (38)$$

At this point, the wave vector is known, but the frequency and polarization vector are not. Note that the index k introduced in Eq. (30) has been replaced by (κ, ν) . The polarization vector and frequency are both functions of the wave vector and the dispersion branch, denoted by ν . Substituting Eq. (38) and its second derivative into the equation of motion, Eq. (37), leads to the eigenvalue equation

$$\omega^2(\kappa, \nu) \mathbf{e}(\kappa, \nu) = \mathbf{D}(\kappa) \cdot \mathbf{e}(\kappa, \nu) \quad (39)$$

where the mode frequencies are the square roots of the eigenvalues and the polarization vectors are the eigenmodes. They are obtained by diagonalizing the matrix $\mathbf{D}(\kappa)$, which is known as the dynamical matrix, and has size $3n \times 3n$. It can be broken down into 3×3 blocks (each for a given jj' pair), which will have elements

$$D_{\alpha, \beta}(jj', \kappa) = \frac{1}{(m_j m_{j'})^{1/2}} \sum_l \Phi_{\alpha, \beta} \begin{pmatrix} jj' \\ ll' \end{pmatrix} \exp\{i\boldsymbol{\kappa} \cdot [\mathbf{r}(j'l') - \mathbf{r}(jl)]\} \quad (40)$$

The LJ crystal phase considered is monatomic, so that the dynamical matrix has size 3×3 . There are thus three modes associated with each wave

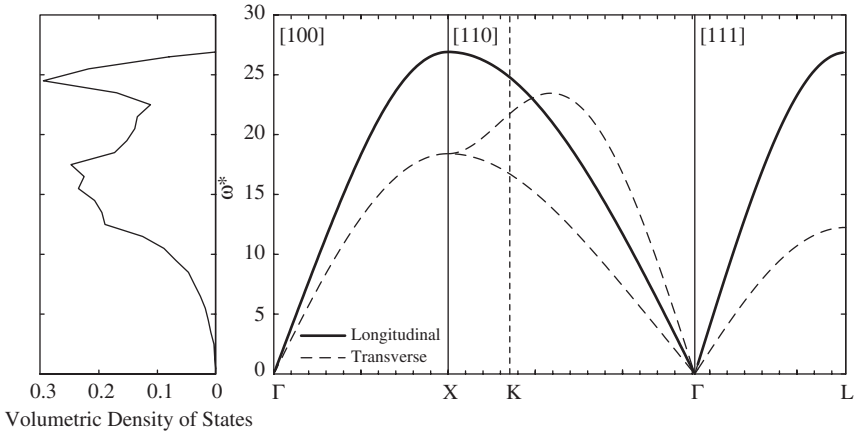


FIG. 12. Dimensionless dispersion curves and density of states for the LJ fcc crystal at zero temperature.

vector. Given the equilibrium atomic positions and the interatomic potential, one can find the frequencies and polarization vectors by substituting the wave vector into the dynamical matrix and diagonalizing. While this calculation can be performed for any wave vector, it is important to remember that only certain values are relevant to the analysis of a particular MD simulation cell.

The phonon dispersion curves are obtained by plotting the normal mode frequencies as a function of the wave number in different directions. These are shown in dimensionless form for the [1 0 0], [1 1 0], and [1 1 1] directions in Fig. 12 for the zero-temperature simulation cell. The first BZ for the fcc lattice is shown in Figs. 13(a) and (b). A dimensionless wave vector, κ^* , has been defined as

$$\kappa^* = \frac{\kappa}{2\pi/a} \quad (41)$$

such that κ^* will vary between 0 and 1 in the [1 0 0] direction in the first BZ. In Fig. 12, the divisions on the horizontal axis (the wave number) are separated by $0.1 \times 2\pi/a$ (i.e., one-twentieth of the size of the first BZ in the [1 0 0] direction). Note the degeneracies of the transverse branches in the [1 0 0] and [1 1 1] directions, but not in the [1 1 0] direction. Also, as seen in the [1 1 0] direction, the longitudinal branch does not always have the highest frequency of the three branches at a given point. The frequencies of the longitudinal and transverse branches at the X point for argon are 2.00 and 1.37 THz, which compare very well to the experimental values of 2.01

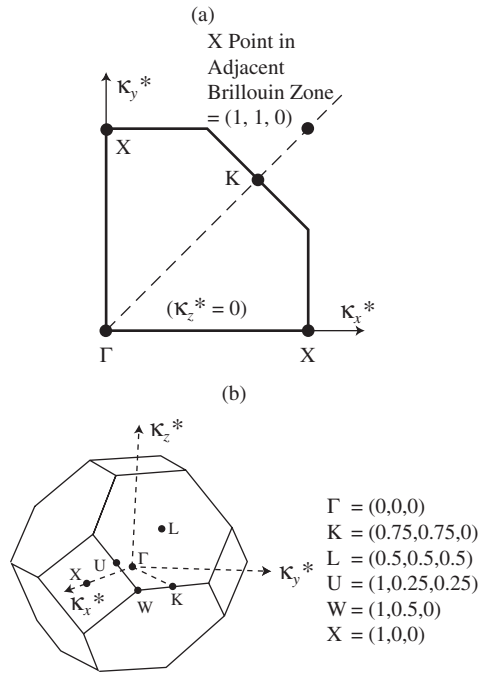


FIG. 13. (a) The [00 1] plane in the fcc crystal BZ showing how the Γ -X and Γ -K-X curves in the LJ dispersion (Fig. 12) are defined. (b) The first BZ for the fcc lattice, and important surface symmetry points. Each of the listed points has multiple equivalent locations.

and 1.36 THz, obtained at a temperature of 10 K [42]. This good agreement is somewhat surprising, as the LJ parameters ϵ_{LJ} and σ_{LJ} are obtained from the properties of low-density gases [43].

The phonon density of states describes the distribution of the normal modes as a function of frequency, with no distinction of the wave vector direction. It can be thought of as an integration of the dispersion curves over frequency. The volumetric density of states for the zero temperature LJ fcc crystal is plotted in Fig. 12 alongside the dispersion curves. The data are based on a BZ with a grid spacing of $1/21 \times 2\pi/a$. This leads to 37,044 distinct points (each with three polarizations) covering the entire first BZ. The frequencies are sorted using a histogram with a bin size of unity, and the resulting data are plotted at the middle of each bin. The density of states axis is defined such that an integration over frequency gives $3(N-1)/V \simeq 12/a^3$ (for large V , where N is the number of atoms in volume V).

As suggested by Eq. (38), the mode polarizations are required to transform the atomic coordinates to the normal modes (and vice versa). The

relevant transformations are

$$S_k(\boldsymbol{\kappa}, \nu) = N^{-1/2} \sum_i m_i^{1/2} \exp(-i\boldsymbol{\kappa} \cdot \mathbf{r}_{i,o}) \mathbf{e}_k^*(\boldsymbol{\kappa}, \nu) \cdot \mathbf{u}_i \quad (42)$$

$$\mathbf{u}_i = (m_i N)^{-1/2} \sum_k \exp(i\boldsymbol{\kappa} \cdot \mathbf{r}_{i,o}) \mathbf{e}_k^*(\boldsymbol{\kappa}, \nu) S_k \quad (43)$$

As discussed, the normal modes are a superposition of the positions that completely delocalize the system energy, and are best thought of as waves.

4. Phonon Relaxation Time

While the harmonic analysis of the preceding section establishes some methodology, it is not directly applicable to a finite temperature crystal, where anharmonic effects lead to thermal expansion and mode interactions (which lead to finite thermal conductivities). In this section and the next, we show how results of MD simulations can be used to predict finite temperature phonon relaxation times and dispersion curves.

The phonon relaxation time, τ , as originally formulated in the BTE models of Callaway [44] and Holland [45], gives an indication of how long it will take a system to return to equilibrium when one phonon mode has been perturbed. One can also think of the relaxation time as a temporal representation of the phonon mean free path if the phonon-particle description is valid (i.e., $\tau = \nu\Lambda$), or as an indication of how long energy stays coherent in a given vibrational mode.

Ladd *et al.* [46] present a method that finds the relaxation time of the k th mode, $\tau_{k,r}$, using the time history of the mode potential energy, Φ_k . This method has been modified by considering the total energy (potential and kinetic) of each mode, E_k [28]. Under the harmonic approximation, the instantaneous, total energy of each mode of a classical system is given by

$$E_k = \frac{\omega_k^2 S_k^* S_k}{2} + \frac{\dot{S}_k^* \dot{S}_k}{2} \quad (44)$$

where the first term corresponds to the potential energy and the second to the kinetic energy. The temporal decay of the autocorrelation of E_k is related to the relaxation time of that mode [46]. The resulting curve for the transverse polarization at $\boldsymbol{\kappa}^* = (0.5, 0, 0)$ for the $\eta = 4$ simulation cell at a temperature of 50 K is shown in Fig. 14. The required ensemble average is realized by averaging the autocorrelation functions (10^4 time steps long, based on 2×10^5 time steps of data) over the [100], [010], and [001] directions over five independent simulations. The relaxation time is obtained by fitting the data with an exponential decay. Based on this formulation, the calculated time constant must be multiplied by 2 to get the relaxation time

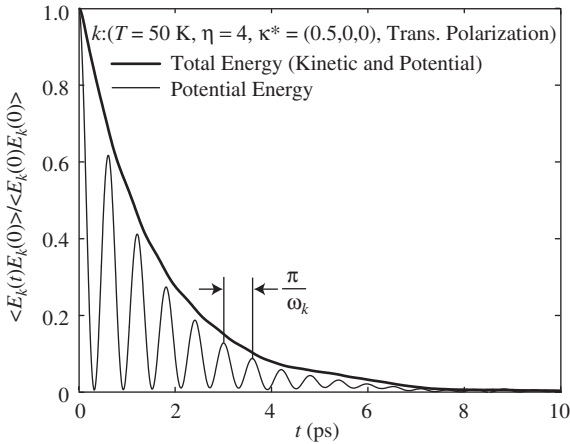


FIG. 14. Autocorrelation curves for the relaxation time and anharmonic phonon dispersion calculation methods. The data correspond to deviations from the mean energy values, and have been normalized against the zero time value of the autocorrelations. Shown are the total mode energy (used in the relaxation time calculation) and the potential energy (used to obtain the anharmonic phonon frequencies). The frequency of the oscillations in the potential energy curve is double that of the phonon mode in question because of the squaring operations in Eq. (44). From McGaughey and Kaviani [28]. Copyright (2004), with permission from America Physical Society.

used in the Callaway–Holland BTE formulation [28]. This is the value reported here. Most of the modes considered show a general behavior consistent with a single relaxation time. For some modes, a secondary decay is evident in the very early stages of the overall decay. In these cases, one neglects this portion of the autocorrelation when fitting the exponential. Alternatively, one could calculate the integral of the autocorrelation and from that deduce an effective relaxation time [46]. Owing to the short extent of the observed deviation from a single exponential decay, and the subsequent fitting of a continuous function to the discrete relaxation times, the difference between this approach and that used here is negligible.

To obtain a sufficient number of points within the first BZ to form continuous relaxation time and dispersion functions in a particular BZ direction (required for upscaling to the BTE [28]), one must consider different-sized simulation cells. Having obtained a set of discrete $\tau_{k,r}$ values for a given temperature and polarization using the 256, 500, and 864 atom simulation cell, a continuous function, τ_r , can be constructed in the principle directions (where there is sufficient data). The discrete and continuous results for the LJ fcc crystal in the [100] direction at temperatures of 20, 35, 50, 65, and 80 K are plotted as $1/\tau_{k,r}$ (or $1/\tau_r$) vs. ω in Figs. 15(a) and (b). The data for each polarization can be broken down into three distinct regions. The first

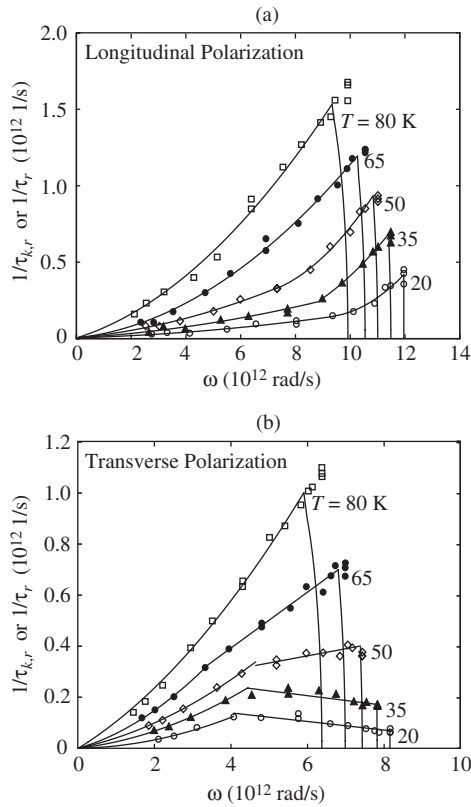


FIG. 15. Discrete relaxation times ($\tau_{k,r}$) and continuous curve fits (τ_r) for the LJ fcc crystal for (a) longitudinal and (b) transverse polarizations. From McGaughey and Kavinay [28]. Copyright (2004), with permission from America Physical Society.

two are fit with low-order polynomials. For the longitudinal polarization, the first region is fit with a second-order polynomial through the origin, and the second region with a second-order polynomial. For the transverse polarization, the first region is fit with a second-order polynomial through the origin, and the second region with a linear function. The resulting functions are also shown in Figs. 15(a) and (b) and are considered satisfactory fits to the MD data. The parts of the relaxation time curves are not forced to be continuous. For both the longitudinal and transverse polarizations, any resulting discontinuities are small, and are purely a numerical effect. The relaxation time functions do not contain the orders of magnitude discontinuities found in the Holland relaxation times for germanium, which result from the assumed functional forms, and how the

fitting parameters are determined [47]. As the temperature increases, the behavior in the two regions becomes similar. For both polarizations at a temperature of 80 K, and for the longitudinal polarization at a temperature of 65 K, a single second-order polynomial through the origin is used to fit all data. In the third region, the continuous relaxation time functions are taken up to the maximum frequency ($\omega_{L,max}$ or $\omega_{T,max}$) using the Cahill–Pohl (CP) high scatter limit [32,33], which requires that the relaxation time correspond to at least one half of the mode’s period of oscillation.

Dimensionless relaxation times for all distinct points in the first BZ of the 256 atom simulation cell (18 points describing 30 unique modes [11]) are plotted as (τ_r^* vs. κ^*) and as ($1/\tau_r^*$ vs. ω^*) in Figs. 16(a) and (b). The continuous

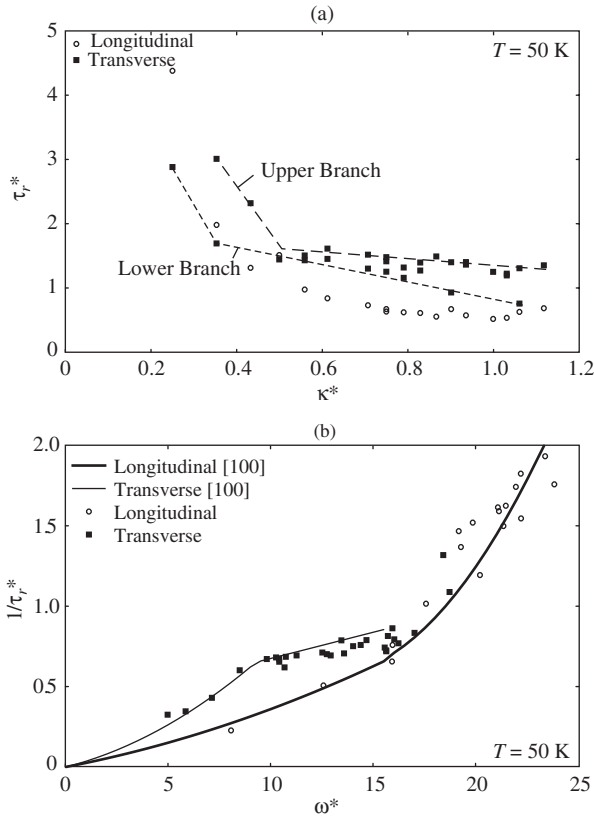


FIG. 16. Full BZ relaxation times at $T = 50$ K for the $\eta = 4$ simulation cell. (a) Relaxation time as a function of the wave number. Note the two distinct branches for the transverse polarization. (b) Inverse of the relaxation time as a function of frequency [compare to Fig. 15(a)]. The separation of the transverse data seen in (a) does not manifest. All results are dimensionless.

functions from Fig. 15 are also plotted in Fig. 16(b). For the longitudinal modes, the relaxation times show a common trend and agree well with the $[100]$ curve. The discrepancy is larger for the transverse modes. In fact, two independent trends are clear in the wave number plot. All things being equal with the phonon dispersion, the fact that the secondary branch is lower than the main trend of the data is consistent with the isotropic assumption resulting in an over-prediction of the thermal conductivity, as found in Ref. [28]. The two transverse branches are not obvious in the frequency plot. The splitting is also most evident at the intermediate temperatures. At the low temperature (20 K), the larger uncertainties in the relaxation times make trends harder to discern. At the high temperature (80 K) all the relaxation times (longitudinal and transverse) appear to follow the same trend.

5. Phonon Dispersion

The zero-temperature phonon dispersion shown in Fig. 12 is harmonic, and can be determined exactly at any wave vector using the MD equilibrium atomic positions and the interatomic potential. Thus, one can obtain a continuous dispersion relation (see Section III.D.3). Deviations from this calculation at finite temperature result from two effects [5]. Based on the higher order terms in the expansion of the potential energy about its minimum, a solid will either expand (as seen here) or contract as the temperature increases. An expansion causes the phonon frequencies to decrease. Re-calculating the dispersion harmonically with the new lattice constant is known as the quasi-harmonic approximation.

The second effect is a result of anharmonicities in the atomic interactions, which become increasingly important as the temperature increases. It is difficult to model these effects exactly due to the complexity of the higher order terms in Eq. (30). The inclusion of anharmonic effects is important in any application that requires phonon velocities, such as using the BTE to predict the thermal conductivity under the single-mode relaxation time approximation [28]. To account for the anharmonic effects, the autocorrelation data for the mode potential energy are used to calculate the frequencies of the discrete modes present in the MD simulations. This is shown in Fig. 14. While the total energy autocorrelation shows a monotonic decay, that for the potential energy oscillates. This results from the total energy having both potential and kinetic energy components. One obtains an estimate of the anharmonic frequency by averaging over all non-negligible oscillations in the autocorrelation, generating a set of discrete anharmonic frequency data. By comparing these values to the associated quasi-harmonic frequencies, a second-order polynomial scaling function is constructed. This function is then applied to the continuous quasi-harmonic data to obtain the full anharmonic dispersion. The excellent quality of the mapping from the

quasi-harmonic data to the anharmonic data (the R^2 values of the scaling functions are ~ 0.999) suggests that this procedure introduces minimal error.

The frequencies used for the horizontal axes of Figs. 15(a) and (b) are based on the anharmonic dispersion. Note, however, that the frequencies used in the phonon energy calculations [Eqs. (33) and (44)] must be those corresponding to the quasi-harmonic dispersion. This is a result of the phonon dynamics being based on a harmonic theory, while the BTE expression for the thermal conductivity is not. We can justify the need to use the quasi-harmonic frequencies in the phonon energy calculation by calculating the total, average phonon potential energy and comparing the result to that directly calculated with the LJ potential. This is shown for a 4 ps time interval in Figs. 17(a) and (b) for temperatures of 20 and 80 K. To allow

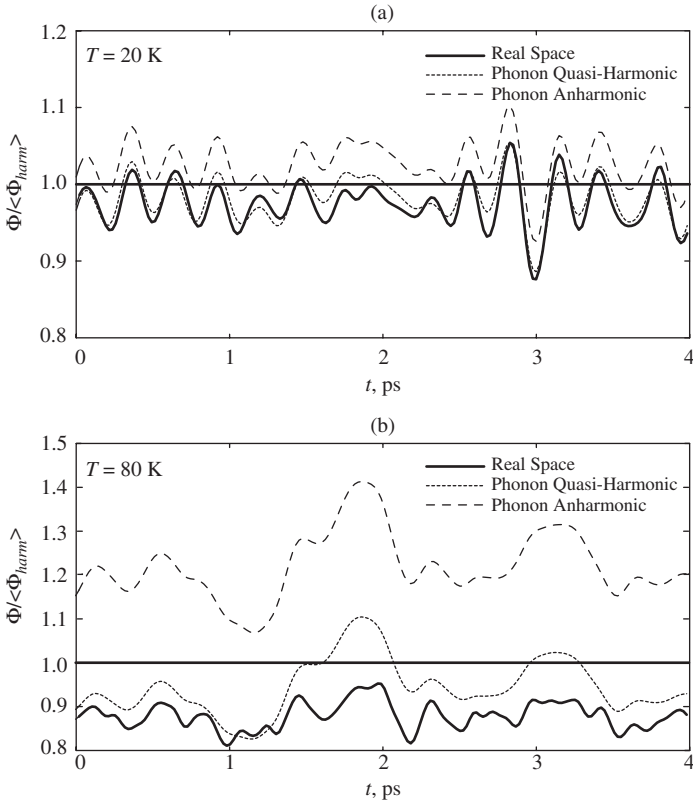


FIG. 17. Real and phonon space energy calculations at temperatures of (a) 20 K and (b) 80 K. The phonon space energy is calculated using both the quasi-harmonic and anharmonic frequencies. While the quasi-harmonic data match the real space calculation reasonably well in both cases, the anharmonic data diverge as the temperature increases.

for a direct comparison of the real space and phonon space energies, the real space value has been shifted by the potential energy that would exist if all the atoms were at their equilibrium positions. The data have been normalized against the classical-harmonic expectation value, $\langle \Phi_{\text{harm}} \rangle = 3(N-1)k_B T/2$.

In Fig. 18(a), the average energy for each case, along with data for temperatures of 35, 50, and 65 K (based on 10^5 time steps of *NVE* MD simulation) is plotted as a function of temperature. Using the quasi-harmonic frequencies results in an energy that matches the magnitude and temperature trend of the exact calculation to within 5% over the entire temperature range considered. The anharmonic results diverge from the

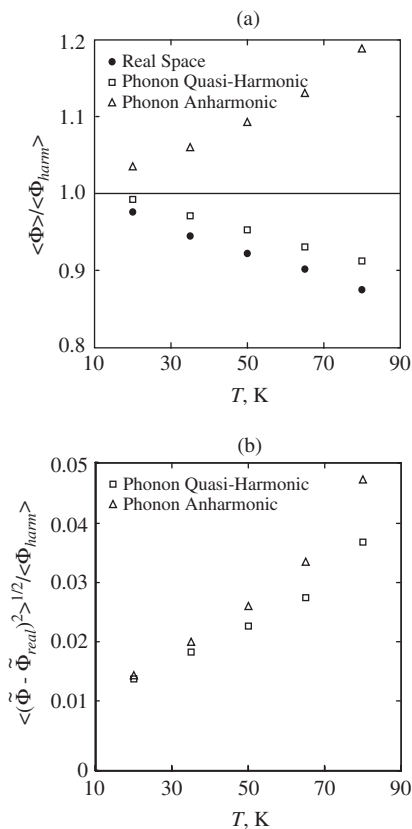


FIG. 18. (a) Average energies calculated using the quasi-harmonic and anharmonic frequencies compared to that predicted directly from the LJ potential in real space. (b) Root mean square deviations of the phonon space energies from that in the real space. In both plots, the energies have been scaled by the expectation value in the classical-harmonic system.

exact calculation, and are 36% larger at the highest temperature. This trend is evident from the plots in Fig. 17.

In Fig. 18(b), the RMS deviation of the phonon space energies (anharmonic and quasiharmonic) compared to the real space energy are plotted. To perform this calculation, all three sets of energy data were shifted to an average value of zero. From Fig. 17, the fluctuations in the quasiharmonic and anharmonic calculations appear to be about the same. Both curves seem to pick up an equivalent amount of the detail in the real space energy. But, as seen in Fig. 18(b), the deviations in the anharmonic data are larger. Therefore, based on both the magnitude and fluctuations in the energy calculations, it is the quasi-harmonic frequencies that need to be used when calculating the phonon space energy. This is not surprising, as the model in use is based in harmonic theory.

The phonon dispersion for the [100] direction is shown in Fig. 19(a) for the zero-temperature simulation cell, and for the quasi-harmonic and anharmonic predictions at a temperature of 50 K. The effect of the unit cell size is significant, and increases with increasing temperature. The anharmonic effects are significant for the longitudinal polarization at all temperatures, and increase with increasing temperature. For the transverse polarization, the deviations from the quasi-harmonic values are found to be significant only at a temperature of 80 K. The discrete anharmonic normal mode frequencies for the entire BZ for the $\eta = 4$ simulation cell at a temperature of 50 K are plotted in dimensionless form in Fig. 20 as a function of the magnitude of the associated wave vector. The anharmonic

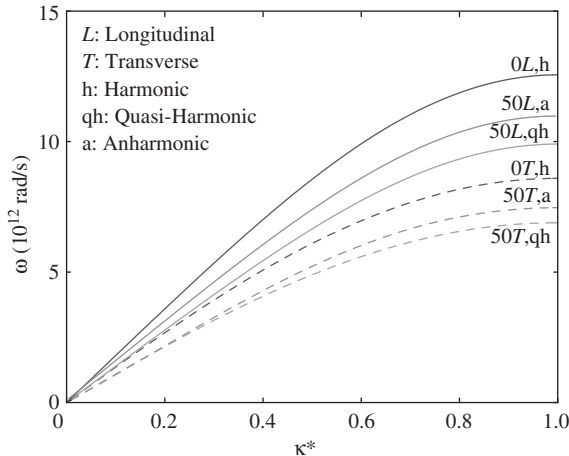


FIG. 19. (a) Phonon dispersion in the [100] direction. The curves are identified by the temperature in Kelvin, the polarization, and the nature of the calculation. From McGaughey and Kaviani [28]. Copyright (2004), with permission from American Physical Society.

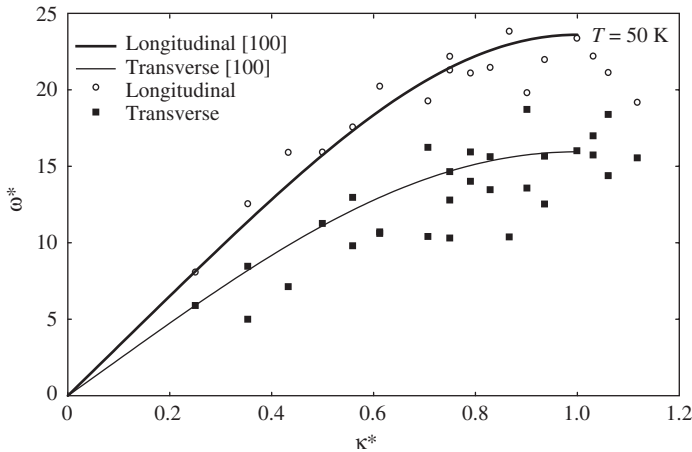


FIG. 20. Full BZ dispersion at $T = 50$ K for the $\eta = 4$ simulation cell. All data are dimensionless.

dispersion curves in the [100] direction are also shown. The [100] data represent the trend in the data for the entire first BZ reasonably well.

IV. Nature of Phonon Transport in Molecular Dynamics Simulations

A. QUANTUM FORMULATION AND SELECTION RULES

Traditionally, phonon transport and interactions have been described in the context of a quantum-particle-based model. The existence of a particle implies localization. A phonon mode in a crystal is, in fact, completely nonlocalized, but one can imagine that in a large system (where the resolution of the BZ is fine), a wave packet can be created by superimposing phonon modes of similar wavelengths. Such a wave packet, or phonon particle, can then move around the system of interest. These phonon particles are assumed to propagate ballistically in between collisions with other phonons, impurities, and boundaries. Under these conditions, the phonon particles are often described as making up a phonon gas.

In MD simulations of a perfect crystal, the only scattering present is a result of inter-phonon interactions. To model such interactions theoretically, it is necessary to consider third order and higher (anharmonic) terms in the expansion of the potential energy about its minimum [see Eq. (30)]. Anharmonicities in the atomic interactions are required to obtain a finite bulk phase thermal conductivity for crystals. Interestingly, a disordered MD system modeled with a harmonic potential can produce a finite thermal conductivity [48,49]. The third order term in the expansion of the potential

energy is related to three-phonon interactions, and is the basis for standard analysis techniques. The mathematics at this level are involved, and the level of complexity increases for fourth order and higher terms. These higher-order effects, however, are generally thought to be insignificant [4].

In the three-phonon interaction formulation there are two types of allowed events. In a type I interaction, one phonon decays into two others. In a type II interaction, two phonons combine to form a third. To satisfy conservation of energy, processes in which three phonons are either created or destroyed are not allowed. Two selection rules exist for the allowed phonon interactions.

First, from the translational invariance of the lattice potential energy, the wave vectors of the phonon modes in question must satisfy [4]

$$\boldsymbol{\kappa}_1 = \boldsymbol{\kappa}_2 + \boldsymbol{\kappa}_3 + \mathbf{G} \quad (\text{type I}) \quad (45)$$

$$\boldsymbol{\kappa}_1 + \boldsymbol{\kappa}_2 = \boldsymbol{\kappa}_3 + \mathbf{G} \quad (\text{type II}) \quad (46)$$

where \mathbf{G} is either equal to zero [corresponding to a Normal (N) process] or a reciprocal lattice vector [corresponding to an Umklapp (U) process]. These criteria are valid in both the classical and quantum descriptions of the phonon system. These wave vector conservation equations are only dependent on the crystal structure, and are not affected by temperature. By multiplying through by \hbar , terms with the units of momentum are obtained, so that this criterion is often referred to as the conservation of crystal (or phonon) momentum. This is not real momentum, however, as no phonon modes (other than that at the center of the BZ) can carry physical momentum. With respect to thermal conductivity, the N and U processes play different roles [44,45]. Note that selection rules for the classical system cannot contain \hbar .

The second selection rule, which only applies to the quantum system, is based on conservation of energy. The second quantization in the formulation of the lattice dynamics theory results in the energy of the phonon modes being discretized into packets of size $\hbar\omega$. For the type I and II interactions, conservation of energy then leads to

$$\hbar\omega_1 = \hbar\omega_2 + \hbar\omega_3 \quad (\text{type I}) \quad (47)$$

$$\hbar\omega_1 + \hbar\omega_2 = \hbar\omega_3 \quad (\text{type II}) \quad (48)$$

With respect to the discussion of Section III.D.5, it is the anharmonic frequencies that should be used here. The second quantization cannot be made in the MD system. Energy is still conserved in the NVE ensemble, but not as described by Eqs. (47) and (48). In the quantum-particle description,

the interactions are assumed to occur instantaneously (i.e., they are discrete events). In the MD system the energy in a given mode is a continuous function of time, and discrete energy exchange events will not occur. One must instead think of a continuous flow of energy between the modes in the frequency space. Considered from another standpoint, the MD system is a nonlinear, many-body dynamics problem being solved using the Newton laws of motion.

The wave vector and energy selection rules only indicate what three-phonon interactions are possible. The rate at which a given interaction takes place is related to the intrinsic scattering rate, and the degree of departure of the mode populations from the equilibrium distribution at an instant in time [4].

B. PHONON GAS AND NORMAL MODES

To describe a phonon system as a phonon gas in which the particles are interacting weakly (i.e., kinetically), a number of criteria must be satisfied regarding the length scales in the system. These are shown schematically in Fig. 21.

To treat a phonon as a particle, a wave packet must be formed, the size of which, l , is much greater than the wavelength, λ , of the mode of interest. For the wave packets to have distinct interactions with each other, the distance they travel between collisions (the average value of this distance is the mean free path, Λ) must be much greater than the size of the wave packets. Finally, if inter-phonon interactions are to dominate the phonon scattering (i.e., diffuse transport), the size of the system, L , must be much greater than the mean free path.

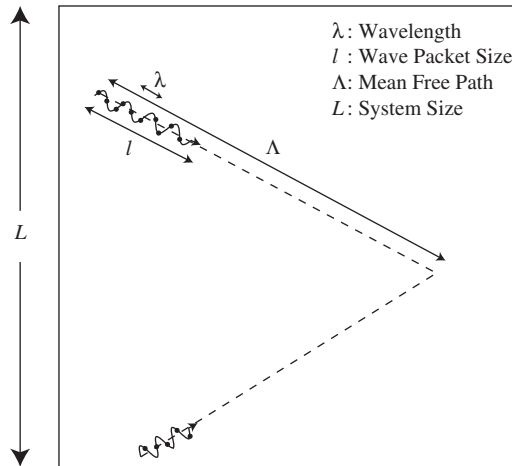


FIG.21. Length scales in the phonon gas. For the phonon particle and phonon gas concepts to be valid, $\lambda \ll l \ll \Lambda \ll L$.

To form a wave packet, modes in the near vicinity of the mode of interest are superimposed. This is not possible in an MD system with a few hundred atoms. For example, in the 256 atom fcc crystal simulation cell, only four nonzero points can be resolved in the [1 0 0] direction. Considered from a different viewpoint, the system is too small to form a wave packet, as the side length is on the order of all the available wavelengths. Very large MD system sizes are required to form a wave packet. This has been done by Schelling *et al.* [50], Schelling and Phillpot [51], and Sinha *et al.* [52], who, for silicon, used simulation cells very long in one direction.

Having established that a wave packet cannot be formed in an MD simulation cell with a few hundred atoms, one can eliminate the possibility of treating the system as a collection of phonon particles. One must thus treat the phonon modes as they are defined in the lattice dynamics theory: as completely nonlocalized modes. The energy within a given phonon mode, while corresponding to a point in frequency space, cannot be spatially resolved in real space.

If a phonon mode cannot be spatially resolved, the concept of the mean free path becomes questionable. It is better to think of the energy in a given mode from a purely temporal perspective in the context of a relaxation time. From the phonon particle perspective, the relaxation time is the average time between collisions. In the nonlocalized description, the relaxation time is an indication of the timescale over which the energy in a mode stays correlated with itself. That is, the time over which a certain percentage of the energy in a mode is a part of the initial, and not the result of energy scattering into the mode as its original energy scatters to other modes. Within this framework, McGaughey [11] has directly observed phonon interactions in MD simulations of LJ argon. The results are interpreted in the context of internal resonance.

V. Thermal Conductivity Prediction: Green-Kubo Method

Two main techniques have been developed to predict the thermal conductivity of a dielectric material using MD simulations. These are the GK approach (an equilibrium method) and a direct application of the Fourier law (a steady state, nonequilibrium approach called the direct method). The implementation and interpretation of the results of these two approaches are discussed in this section and in Section VI.

A. FORMULATION

The development of a time-correlation function expression for the thermal conductivity (the GK approach) is based in classical statistical

thermodynamics [53,54]. Multiple methods can be used to arrive at the final result [55]. Similar approaches can be used to develop expressions for the self-diffusion coefficient, the shear viscosity, and the bulk viscosity. These are all transport coefficients that cannot be obtained by applying a perturbation to the system Hamiltonian, as can be done for some properties (e.g. the electrical conductivity) where there is a real force that drives the transport. A step-by-step derivation using the method of Helfand [56] as outlined by McQuarrie [21], is presented in Ref. [11].

The net flow of heat in a solid, described by the heat current vector, \mathbf{S} , fluctuates about zero at equilibrium. In the GK method, the thermal conductivity is related to how long it takes these fluctuations to dissipate, and for an isotropic material is given by [21]

$$k = \frac{1}{k_B V T^2} \int_0^\infty \frac{\langle \mathbf{S}(t) \cdot \mathbf{S}(0) \rangle}{3} dt \quad (49)$$

where $\langle \mathbf{S}(t) \cdot \mathbf{S}(0) \rangle$ is the heat current autocorrelation function (HCACF). The GK approach is valid in the case of small disturbances from equilibrium and for long times (i.e., the hydrodynamic limit), and should be applied to simulations in the microcanonical ensemble. In ionic systems at high temperature, the charge flux may also contribute to the thermal conductivity. Lindan and Gillan [57] address this issue, which is generally irrelevant, by considering a more formal description of the transport theory. The heat current should be differentiated from the energy current, which is the expression that appears in a formal statement of the transport theory and contains terms related to the mass flux [58].

The heat current vector is given by [21]

$$\mathbf{S} = \frac{d}{dt} \sum_i \mathbf{r}_i E_i \quad (50)$$

where the summation is over the particles in the system, and E_i is the energy (kinetic and potential) of a particle. Either the total or excess energy can be used. The units of the heat current are W m. Those of the heat flux, \mathbf{q} , are W/m² such that $\mathbf{S} = \mathbf{q}V$. One should avoid using the symbol \mathbf{q} for the heat current.

Li [17] has derived a general expression for the heat current for an n -body potential. For a pair potential ($n = 2$), Eq. (50) can be recast as

$$\mathbf{S} = \sum_i E_i \mathbf{v}_i + \frac{1}{2} \sum_{ij} (\mathbf{F}_{ij} \cdot \mathbf{v}_i) \mathbf{r}_{ij} \quad (51)$$

where \mathbf{v} is the velocity vector of a particle. This form of the heat current is readily implemented in an MD simulation, and can be used for both rigid-ion and core-shell potentials [59]. The first term is associated with convection, and the second with conduction. For a three-body potential, an additional conduction term,

$$\frac{1}{6} \sum_{i,j,k} (\mathbf{F}_{ijk} \cdot \mathbf{v}_i)(\mathbf{r}_{ij} + \mathbf{r}_{ik}) \quad (52)$$

where \mathbf{F}_{ijk} is a three-body force, is added to Eq. (51). In many-body potentials ($n > 2$), the division of potential energy between particles is not unique. How the energy is divided has not been found to affect the predicted thermal conductivity [60,61].

Developing a physical interpretation of Eq. (49) is useful. The argument of the derivative in the heat current can be taken as the energy center of mass of the system. It is a vector that indicates the direction of energy transfer in the system at an instant in time. How long this quantity stays correlated with itself is related to the thermal conductivity. In a material with a high thermal conductivity, the correlation will be long lasting (i.e., fluctuations from equilibrium dissipate slowly). For a material with a low thermal conductivity, the correlation will be short-lived. One interesting aspect of the Green–Kubo approach is that with it, transport properties can be obtained from an equilibrium system. This is an important point for the thermal conductivity, since it is generally thought of in a nonequilibrium system with a temperature gradient.

The GK approach was first used to calculate the thermal conductivity of a three-dimensional-solid by Ladd *et al.* [46], who considered an fcc crystal modeled with an inverse 12th-order potential. Since then, researchers from a wide range of disciplines (e.g., mechanical engineering, physics, materials science, and nuclear engineering) have addressed methodological issues and used MD and the GK method as a predictive tool for many different materials.

These include LJ argon [17,27–30,62–68], silicon [61,69–73], β -silicon carbide [60,74], silica structures [34,75], silicon nitride [76], diamond [77], carbon nanotubes [78–82], germanium-based materials [83,84], uranium dioxide [57,58,64,85], uranium nitride [86], calcium fluoride [57,58], potassium chloride [59], clathrate hydrates [87], nanofluids [88], and superlattices [89].

B. CASE STUDY: LENNARD-JONES ARGON

All simulations used in the LJ thermal conductivity calculations presented here consist of 10^6 time steps over which the heat current vector is calculated every five time steps. A correlation length of 5×10^4 time steps with 2×10^5 time origins is used in the autocorrelation function. For all cases, five

independent simulations (with random initial velocities) are performed and the HCACFs are averaged before finding the thermal conductivity. This ensures a proper sampling of phase space [60]. For the fcc crystal at a temperature of 10 K, where the correlation time is long, 10 independent simulations are performed. The main challenge at all conditions is the specification of the integral in Eq. (49).

1. Heat Current Autocorrelation Function and Thermal Conductivity

The HCACF and its integral [whose converged value is related to the thermal conductivity through Eq. (49)] are shown in Figs. 22(a) and (b) for the LJ argon fcc crystal, amorphous phase, and liquid described in Section III.B. The HCACF is normalized by its zero-time value to allow for comparison between the different temperatures. The integral is calculated using the trapezoidal rule. Note that as the temperature increases, the HCACFs of the three phases are approaching each other. The predicted thermal conductivities are shown in Fig. 23 along with experimental data [9], and the MD predictions of Li [17].

The zero-time value of the fcc crystal HCACF shows little temperature dependence (it increases by 10% over the entire temperature range). Li *et al.* [60] observe similar behavior for β -silicon carbide, and suggest that this quantity can be interpreted as a susceptibility. At finite time, the HCACF shows a two-stage decay. There is an initial drop, similar for all cases, followed by a longer decay, whose extent decreases as the temperature increases. The oscillations in the secondary decay are believed to result from the periodic boundary conditions [11]. For all cases considered, the integral of the HCACF converges well, and the thermal conductivity can be specified directly by averaging the integral over a suitable range. To remove the subjective judgment, Li *et al.* [60] proposed two methods by which one can specify the thermal conductivity. In the first dip (FD) method, the integral is evaluated at the first place where the HCACF goes negative. In the exponential fit (EF) method, an exponential function is fitted to the HCACF beyond a certain point (determined on a case-by-case basis), and this function is then used to calculate the contribution of the tail to the integral. Up to that point the integral is evaluated directly. In their investigation of β -silicon carbide, no significant differences were found between the predictions of these two methods.

Based on the observed shape of the fcc crystal HCACF, it can be fitted to a sum of two exponential functions as

$$\frac{\langle \mathbf{S}(t) \cdot \mathbf{S}(0) \rangle}{3} = A_{ac,sh} \exp(-t/\tau_{ac,sh}) + A_{ac,lg} \exp(-t/\tau_{ac,lg}) \quad (53)$$

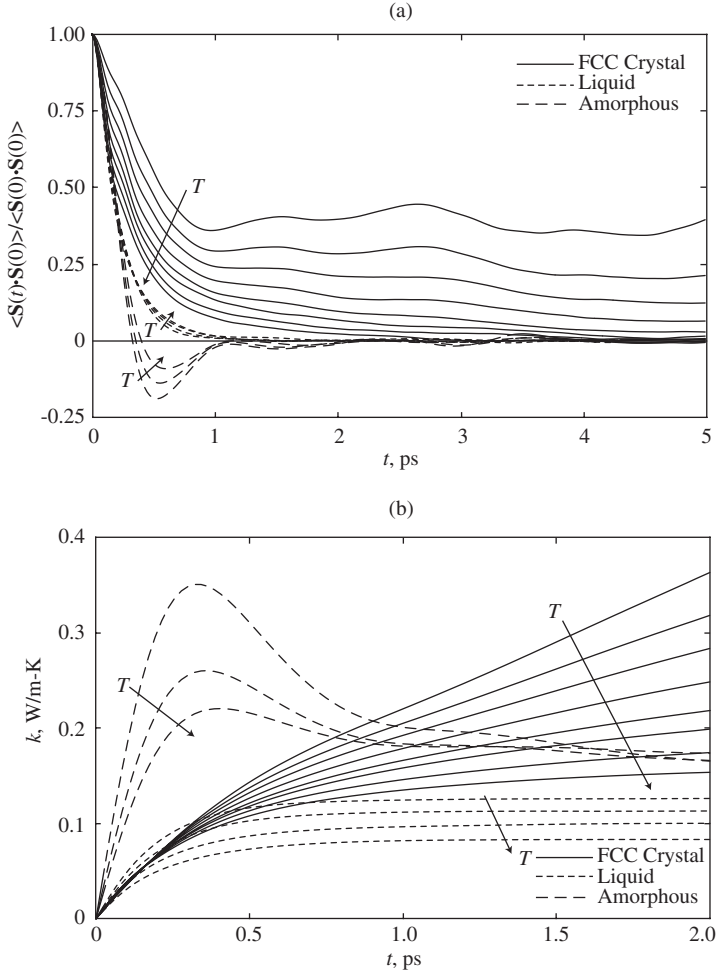


FIG. 22. Time dependence of (a) the raw HCACF and (b) its integral (the thermal conductivity) for LJ phases. Note the different timescales in the two plots.

as suggested by Che *et al.* [77]. With Eq. (49), the thermal conductivity is then

$$\begin{aligned}
 k &= \frac{1}{k_B V T^2} (A_{ac,sh} \tau_{ac,sh} + A_{ac,lg} \tau_{ac,lg}) \\
 &\equiv k_{ac,sh} + k_{ac,lg}
 \end{aligned} \tag{54}$$

In Eqs. (53) and (54) the subscripts *ac*, *sh*, and *lg* refer to acoustic, short-, and long range. Ladd *et al.* [46] first observed the two-stage decay in the HCACF.

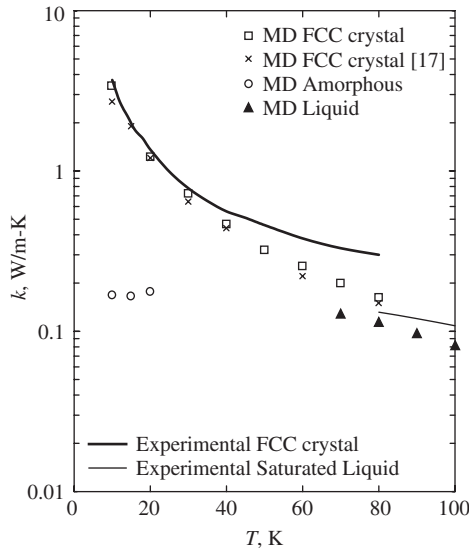


FIG. 23. Temperature dependence of the experimental and MD- predicted LJ argon thermal conductivities.

It is in contrast to the Peierls theory of thermal conductivity, which is consistent with a single-stage decay of the HCACF [17,46]. Kaburaki *et al.* [29] suggest that the two stages in the HCACF represent contributions from local dynamics and the dynamics of phonon transport, each having a time constant τ and strength A . The use of the term “local” is questionable, as in a crystal, there are no localized vibrational modes. Che *et al.* [77] associate the initial, fast decay of the HCACF with optical phonons, which cannot be the case here, as the unit cell is monatomic. Fitting the HCACF according to Eq. (53) captures the two-stage decay very well at all temperatures [27]. The only region where the exponential does not fit is at very short times, when Markovian processes are not yet present [77]. The fits of a single exponential function with time constant τ_1 , according to

$$\frac{\langle \mathbf{S}(t) \cdot \mathbf{S}(0) \rangle}{3} = A_1 \exp(-t/\tau_1) \quad (55)$$

are reasonable at low and high temperatures, but poor at the intermediate temperatures [11].

For a series of five sets of five simulations at a temperature of 50 K for the fcc crystal, the thermal conductivities calculated with Eq. (54) fall within a range of 6.0% of their average value. This error is expected to increase as the

temperature decreases, and longer correlation times are required for convergence. The thermal conductivity predicted by the fit of a single exponential function [Eq. (55)] to the fcc crystal HCACF agrees with the prediction of the fit of the sum of two exponentials [Eq. (53)] to within 2.2% and 12.2% at the temperature extremes of 10 and 80 K. At the intermediate temperatures, the difference between the two predictions is as much as 31% (at a temperature of 50 K). This confirms the importance of considering the two-stage decay. The success of the single exponential function at low temperatures is due to the dominance of $k_{ac,lg}$. At high temperatures, the single exponential succeeds because the two time constants have similar values [11].

For the fcc crystal, the direct specification of the integral and the FD method agree to within 3.6% at all temperatures. The thermal conductivities calculated by the fit of Eq. (53) to the HCACF for all temperatures agree with the direct specification and FD predictions to within 2.0%. The fcc crystal MD results are in reasonable agreement with the trend and magnitude of the experimental data (a decrease above the experimental peak value, which is near a temperature of 6 K), justifying neglecting quantum effects. The data are in good agreement with those of Li [17]. Tretiakov and Scandolo [30] have reported LJ argon fcc crystal thermal conductivity results that are in better agreement with the experimental data. This may be a result of their simulation setup, which resulted in higher densities than those found here [90].

Schelling *et al.* [61] have found a long tail in the HCACF of silicon at a temperature of 1000 K that is not well described by an exponential function. They find that a single exponential fit to the HCACF gives a thermal conductivity value 42% lower than that found from the direct specification of the integral. The thermal conductivities studied are around 50 W/m K, so that based on the predicted order of $k_{ac,sh}$, considering two exponentials would not affect the results. They indicate that such exponential fits are unsuitable. Evidence to support the two-stage exponential fit is found in simulations of LJ argon [27], a series of silica structures [34], silicon nitride [76], and carbon structures [77,78]. In the work of Che *et al.* [77], the thermal conductivity of diamond is predicted to be 1220 W/m K, a very large value. Thus, the failure of the exponential fit, as found for silicon, is not solely related to a large value of the thermal conductivity.

The two-stage behavior of the fcc crystal HCACF, and the resulting decomposition of the thermal conductivity into two distinct components, has been interpreted in the context of the mean phonon relaxation time [27]. While the relaxation time is generally taken to be an averaged quantity (over all phonons in a system or over those of a given phonon mode), it can be applied to an individual phonon. For a given phonon mode, there will thus be some continuous distribution of relaxation times. Physically, the lower bound on

the relaxation time corresponds to a phonon with a mean free path equal to one half of its wavelength. This is the CP limit, a thermal conductivity model developed for amorphous materials [32,33]. The first part of the thermal conductivity decomposition ($k_{ac,sh}$) takes into account those phonons with this limiting value of the relaxation time. Phonons with longer relaxation times are accounted for by the second term ($k_{ac,lg}$), which has a longer decay time.

The liquid HCACF shows a single-stage decay, with a timescale comparable to that of the initial drop in the fcc crystal HCACF. Both the FD and EF methods are suitable for specifying the thermal conductivity. The fit of a single exponential to the liquid HCACF predicts a thermal conductivity that agrees with that predicted by the direct specification and FD methods to within 5.7% for all temperatures. The experimental liquid data correspond to saturation conditions, and agree reasonably well with the MD predictions.

The amorphous phase HCACF shows a very different behavior. It drops below zero in the initial decay, and oscillates between positive and negative as it converges to zero. The velocity autocorrelation function for amorphous LJ argon shows a similar form [91]. This behavior can be interpreted as follows. In the fcc crystal, each atom experiences the same local environment. By averaging over time, the same is true for the liquid. This is not the case for the amorphous solid, where each atom has a distinct local environment. At short timescales, atoms near their equilibrium positions experience the free trajectory of a liquid atom. When the atom eventually feels the effects of the other atoms, the trajectory changes. Because the intended trajectory cannot be completed, the correlation goes negative. The timescale for this behavior is comparable to that of the liquid HCACF. The FD and EF methods are not appropriate here, and the thermal conductivity must be found from a direct specification of the integral. The amorphous phase thermal conductivity results are independent of temperature. This is attributed to the small temperature range studied, the approximately constant specific heat in the classical MD simulations, and the attainment of the CP limit (i.e., the mean free path is a minimum, and equal to one half of the wavelength of a given mode). Two additional amorphous phases with 250 atoms gave thermal conductivities of 0.170 and 0.166 W/m K at a temperature of 10 K (the plotted value is 0.170 W/m K), indicating that the phases considered are truly disordered. Amorphous phases with 500 and 1000 atoms both gave thermal conductivities of 0.165 W/m K, indicating that the periodic boundary conditions do not introduce undesired effects.

2. Thermal Conductivity Decomposition

In Fig. 24, the decomposition of the fcc crystal thermal conductivity into $k_{ac,sh}$ and $k_{ac,lg}$ is shown along with the classical limit of the CP limit, k_{CP} ,

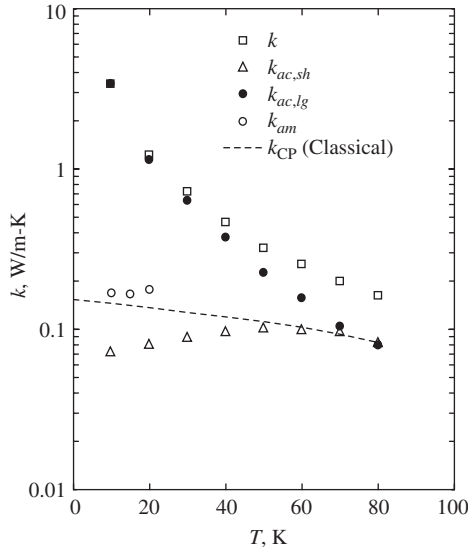


FIG. 24. Decomposition of the LJ fcc crystal thermal conductivity as described by Eq. (54).

and k_{am} . The idea of the crystal-phase thermal conductivity being made up of temperature-dependent and independent components has been explored previously in attempts to interpret experimental data [92,93]. In the decomposition given by Eq. (54), all of the temperature dependence of the thermal conductivity is contained in $k_{ac,lg}$, while the short-range component, $k_{ac,sh}$, shows little temperature dependence. We believe this behavior to be a result of the coordination of the atoms remaining constant as the density changes; it has also been found in silica structures [34] and carbon structures [77]. It has been proposed as a thermal conductivity limit [34].

Based on the association of $k_{ac,sh}$ with k_{CP} it might be expected that $k_{ac,sh}$, k_{am} , and k_{CP} would be the same. As shown in Fig. 24, while an exact equality is not observed, this statement is reasonable. The amorphous phase thermal conductivities are quite close to the CP limit. The values of $k_{ac,sh}$ at the higher temperatures agree with k_{CP} . The disagreement at low temperatures may be a result of the fitting procedure for $k_{ac,sh}$. In the liquid phase (see Fig. 23), the thermal conductivity drops below the fcc crystal value to near $k_{ac,sh}$. Once the solid phase has been eliminated, only short-range interactions are important. The lack of fixed atomic positions in the liquid leads to an improved efficiency of these interactions in the transfer of heat, a shorter time constant, and a slightly higher thermal conductivity than $k_{ac,sh}$.

In Fig. 25, $\tau_{ac,sh}$ is plotted along with τ_{LJ} , τ_D , τ_{nm} (see Section III.C.1 for a description of these quantities), and τ_1 for the liquid phase. Between

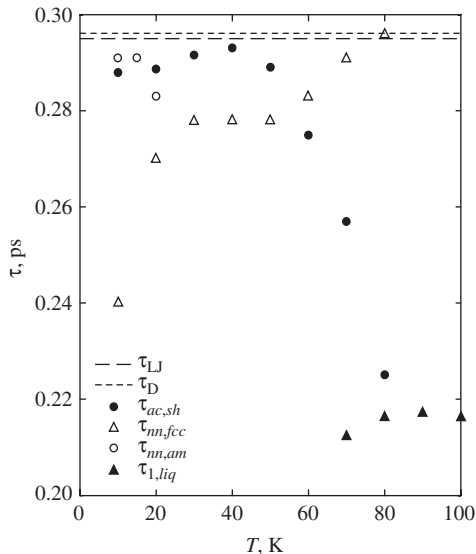


FIG. 25. Comparison of the short-time constants extracted from the MD simulations and from analytical calculations.

temperatures 20 and 60 K, there is an agreement to within 7% between $\tau_{ac,sh}$ and τ_{nm} . Thus, the first timescale in the HCACF decomposition is related to how long it takes for energy to move between nearest-neighbor atoms. No simulation cell size effects on the magnitude of $\tau_{ac,sh}$ or $k_{ac,sh}$ in the LJ argon system have been found, suggesting that the associated phonons are in the higher frequency range of the acoustic branches (i.e., those with wavelengths on the order of a few atomic spacings). From a real space perspective, one can imagine the movement of a phonon through a system as a series of energy transfers between neighboring atoms. For a phonon with a mean free path on the order of its wavelength (as assumed for $k_{ac,sh}$), this will correspond to a few $\tau_{ac,sh}$, which explains why this is the timescale found in the decomposition. Thus, this component of the thermal conductivity is strongly a function of the coordination of the atoms.

3. Multi-atom Unit Cell Decomposition

In the LJ fcc argon crystal the HCACF decays monotonically (see Fig. 22). Small oscillations can be attributed to the periodic boundary conditions. In other materials, such as β -silicon carbide [60] and diamond [77], larger oscillations are present, but their magnitudes are small

compared to the total value of the HCACF. In such cases the thermal conductivity can be specified using different approaches, as discussed in Section V.B.1.

The HCACFs of some materials, such as silica structures [34], germanium structures [83], and carbon structures [77] do not decay monotonically. As shown in Figs. 26(a) and (b), for quartz(a) and quartz(c) at temperatures of 250 and 200 K, there are large oscillations in the HCACF. Similar oscillations have been attributed to the relative motion of bonded atoms with different masses [77]. Such behavior, however, has also been observed in an all germanium clathrate structure [83]. This suggests the more general explanation that the oscillations are a result of optical phonons. Lindan and Gillan [57] attribute the oscillations specifically to transverse optical phonons in CaF_2 and UO_2 by comparing the one observed oscillation frequency to phonon dispersion curves. In many cases more than one mode of oscillation is present [34], so their statement should not be generalized. The FD and EF methods are not suitable for determining the thermal

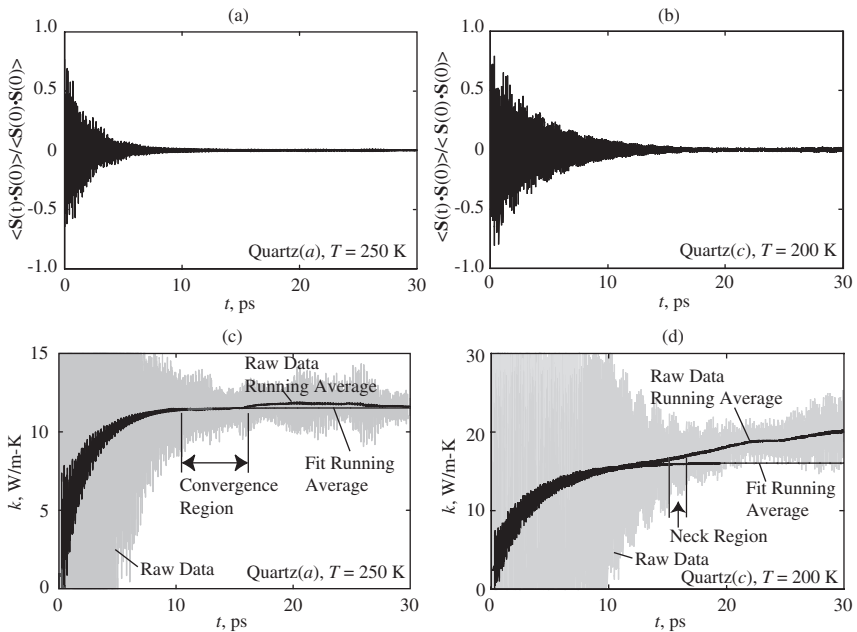


FIG. 26. Time dependence of the HCACF [(a) and (b)] and its integral [(c) and (d)] (whose converged value is proportional to the thermal conductivity) for quartz(a) at $T = 250$ K and quartz(c) at $T = 200$ K. From McGaughey and Kavinany [34]. Copyright (2004), with permission from Elsevier.

conductivity. Even the direct specification of the integral in Eq. (49) is not trivial. Noise in the HCACF can result in no obvious convergence region.

The following scheme has been proposed for the direct specification of the thermal conductivity [34] and is described here with respect to simulations of silica structures. First, the integral is averaged in overlapping blocks of 2500 time steps. The resulting curves related to Figs. 26(a) and (b) are shown in Figs. 26(c) and (d), along with the raw data. When the convergence is clear [Fig. 26(c)], a region of at least 5000 time steps is chosen over which the integral is deemed to have a constant value. The integral is averaged over this region, and this value is used to determine the thermal conductivity. When the convergence is not clear [Fig. 26(d)], it has been observed that the oscillations reach a minimum (i.e., a neck) before the divergence begins. Through comparison to the cases where the integral clearly converges, it is found that the HCACF function beyond this point does not make a significant contribution to the integral. An average of the integral is taken over 1000 time steps around the neck. This is the value used in the specification of the thermal conductivity.

The thermal conductivity decomposition can be applied in such a case by fitting the HCACF to a function of the form

$$\frac{\langle \mathbf{S}(t) \cdot \mathbf{S}(0) \rangle}{3} = A_{ac,sh} \exp(-t/\tau_{ac,sh}) + A_{ac,lg} \exp(-t/\tau_{ac,lg}) + \sum_i B_{op,i} \exp(-t/\tau_{op,i}) \cos(\omega_{op,i}t) \quad (56)$$

so that, from Eq. (49),

$$k = \frac{1}{k_B V T^2} \left(A_{ac,sh} \tau_{ac,sh} + A_{ac,lg} \tau_{ac,lg} + \sum_i \frac{B_{op,i} \tau_{op,i}}{1 + \tau_{op,i}^2 \omega_{op,i}^2} \right) \equiv k_{ac,sh} + k_{ac,lg} + k_{op} \quad (57)$$

The subscript *op* refers to optical phonon modes, which have a strength *B*. This procedure was found unsuitable for an amorphous silica phase, whose thermal conductivity must be specified directly from the integral of the HCACF [34]. The task of fitting the silica HCACFs to a function of the form of Eq. (56) is not trivial. A general procedure has been outlined [34], which is based on taking the Fourier transform of the HCACF, and fitting the optical modes in the frequency space, where the peaks are found to be well defined. Domingues *et al.* [94] used a similar approach to show that the thermal transport in β -cristobalite is a result of rigid unit modes.

4. Convective and Conductive Contributions

Defining, for a pair potential,

$$\mathbf{S}_k = \frac{1}{2} \sum_{ij} (\mathbf{F}_{ij} \cdot \mathbf{v}_i) \mathbf{r}_{ij} \quad (58)$$

$$\mathbf{S}_u = \sum_i e_i \mathbf{v}_i \quad (59)$$

where \mathbf{S}_k and \mathbf{S}_u are the conductive and convective contributions to the heat current, the autocorrelation in Eq. (49) become

$$\langle \mathbf{S}(t) \cdot \mathbf{S}(0) \rangle = \langle \mathbf{S}_k(t) \cdot \mathbf{S}_k(0) \rangle + 2\langle \mathbf{S}_k(t) \cdot \mathbf{S}_u(0) \rangle + \langle \mathbf{S}_u(t) \cdot \mathbf{S}_u(0) \rangle \quad (60)$$

where there are individual terms for conduction and convection, and a cross term. Some investigations of solids have neglected the convection term in Eq. (51) [65,71]. A breakdown of the LJ fcc HCACF at a temperature of 50 K into the three components in Eq. (60) is shown in Fig. 27. While the convection contribution is indeed small, the cross term is not insignificant. It also displays a peculiar shape that warrants further study. The relative contributions of the conductive, convective, and cross terms to the thermal conductivity are 0.892,

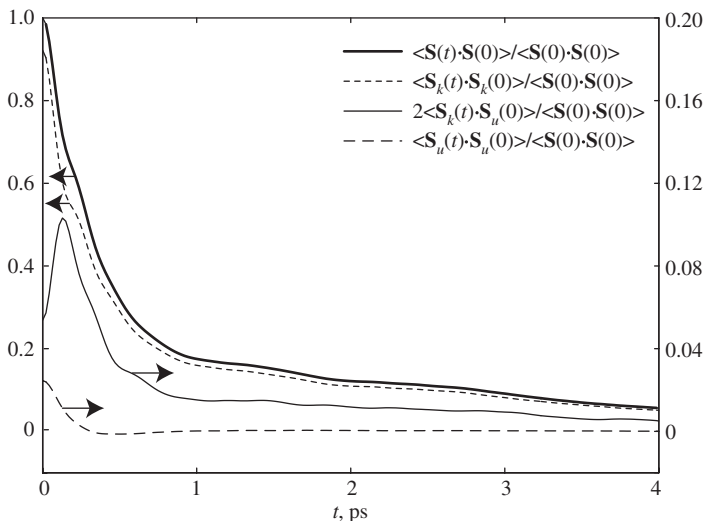


FIG. 27. Breakdown of the HCACF of the LJ fcc argon crystal at a temperature of 50 K into contributions from the conduction and convection parts of the heat current. Note that the total HCACF and the conduction component correspond to the left vertical axis, while the cross and convection curves correspond to the right axis.

0.005, and 0.103. The relative contributions of the convective and cross terms increase as the temperature goes up and anharmonic effects inhibit “pure” conduction. The absolute values of the conduction and cross term thermal conductivities both decrease with increasing temperature, while the convection contribution remains the same. While the convective term may not be as important for materials with higher thermal conductivity, in general, this contribution (and that of the cross term) should be checked before assuming they are negligible. This is particularly true at higher temperatures. Vogelsang *et al.* [62] investigated a similar breakdown for the LJ liquid. To identify heat transfer mechanisms in clathrate hydrates, Inoue *et al.* [87] have considered the contributions to the thermal conductivity from the conduction and convection terms, plus a torsional term that appears because of the rigid nature of their water molecule model. They did not consider any cross terms (three in this case), but the analysis allowed them to isolate the effect of the caged species on the thermal transport. A different breakdown of the HCACF has been performed by Keblinski *et al.* [88], who considered heat transfer in a single LJ nanoparticle suspended in an LJ fluid. By considering the liquid and solid HCACFs separately, they identified backscattering of phonons at the liquid–vapor interface.

One should not confuse neglecting the convection part of the heat current with an alternative definition of the heat current where the average atomic positions are used [46]:

$$\mathbf{S} = \frac{1}{2} \sum_{i,j} (\mathbf{F}_{ij} \cdot \mathbf{v}_i) \mathbf{r}_{o,ij} \quad (61)$$

As discussed by Li [17], using Eq. (61) should lead to the same thermal conductivity as Eq. (51) for a solid, as there is not a unique way to define the heat current. Equation (61) will not be valid in a liquid where there can be net motion of particles. Ladd *et al.* [46] define two other heat currents based on the harmonic approximation: one in real space and the other in phonon space. Li [17] presents a thorough investigation and discussion of all four forms of the heat current. From a standpoint of extracting as much information as possible from the simulations, Eq. (51) is most useful.

5. Spectral Methods

Two different spectral methods exist for predicting the thermal conductivity using the GK method. As first described by Lee *et al.* [69], and later derived in detail by Li and Yip [74], the thermal conductivity can be related to the power spectrum of the Fourier transform of the heat current, $S(\omega)$, by

$$k = \frac{1}{2t_{sim}} \frac{1}{k_B T V^2} \lim_{\omega \rightarrow 0} |S(\omega)|^2 \quad (62)$$

where t_{sim} is the length of the simulation. This method is useful because it reduces the computational load required to perform the autocorrelation, which may be substantial in materials with high thermal conductivities and long correlation times. The disadvantage of this approach is that the limit in Eq. (62) may not be trivial to evaluate. The smallest frequency that is physically meaningful is determined by the size of the simulation cell (i.e., the longest allowed wavelength, see Section III.D.2). Data at lower frequencies will come out in the Fourier transform due to long simulation times, but are meaningless. This is evident in the results of Lee *et al.* [69], shown in Fig. 28. In order to find the thermal conductivity, they perform an extrapolation of the Fourier transform power spectrum curve. The error associated with such an extrapolation is likely on the same order as the error introduced by different methods for evaluating the integral of the HCACF. Li and Yip [74] have used this approach with β -silicon carbide. They obtained reasonable values for the thermal conductivity (when compared to time integration). The computational time required was an order of magnitude less than that required to generate the HCACF.

The second approach to predicting the thermal conductivity with a spectral method is to take the Fourier transform of the HCACF,

$$\int_0^\infty \langle \mathbf{S}(t) \cdot \mathbf{S}(0) \rangle \exp(i\omega t) dt \tag{63}$$

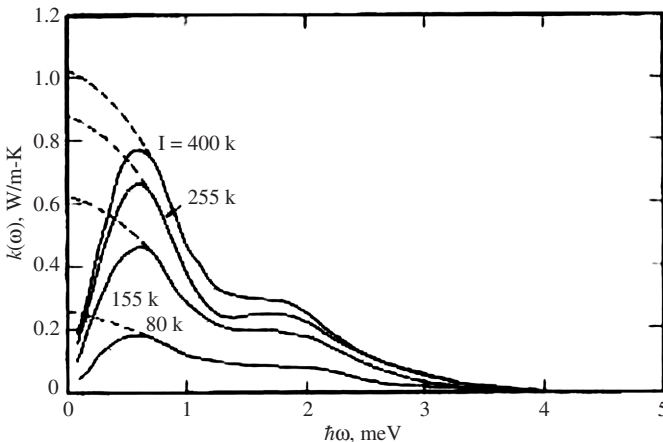


FIG. 28. Frequency-dependent thermal conductivity of amorphous silicon. The dotted lines show the extrapolation required to obtain the static thermal conductivity. From Lee *et al.* [69]. Copyright (1991), with permission from American Physical Society.

and then define the frequency-dependent thermal conductivity as

$$k(\omega) = \frac{1}{3k_B VT^2} \int_0^\infty \langle \mathbf{S}(t) \cdot \mathbf{S}(0) \rangle \exp(i\omega t) dt \quad (64)$$

The static thermal conductivity, that normally predicted and reported, is the zero-frequency limit of Eq. (64). In taking this limit, similar issues as with the first approach exist, in that the data will be unreliable below the minimum frequency allowed in the simulation cell. Extrapolation techniques are required. By assuming that the HCACF follows a single exponential decay as given by Eq. (55), the frequency-dependent thermal conductivity is found to be

$$k(\omega) = \frac{A_1 \tau_1}{3k_B VT^2} \frac{\tau}{1 + i\tau\omega} \quad (65)$$

The imaginary part can be interpreted as the lag between the heat flux and the temperature gradient in a system excited at frequency ω .

For analysis purposes, the frequency-dependent thermal conductivity is often presented as the modulus of Eq. (65) so that

$$k(\omega) = \frac{A_1 \tau_1}{3k_B VT^2} \frac{\tau}{(1 + \tau^2 \omega^2)^{1/2}} \quad (66)$$

This function can be fit to the power spectrum of the HCACF Fourier transform. Two exponentials can also be used [76]. Only the data beyond the minimum system frequency should be used in the fit. One could also fit the real part of Eq. (65) to the real part of the Fourier transform (the imaginary part goes to zero at zero frequency). Not surprisingly, this procedure has been found to give good agreement with time integration results when the HCACF is well modeled with the sum of two exponentials [76]. When a long tail is present in the HCACF, and an exponential fit is inappropriate, similar disagreement is found at the low frequencies in the frequency space fit [61]. This approach does not appear to present any significant advantages over time integration for HCACFs that decay smoothly.

6. Nonequilibrium Green-Kubo

To reduce the required computational time, a nonequilibrium technique that uses the GK expression for the thermal conductivity has been developed [95–98]. A fictitious field, $\mathbf{F}(t)$, that induces an energy flux while not creating a temperature gradient is applied to the MD system. This allows for the use of periodic boundary conditions in a reasonably sized

system, and is accomplished by modifying the equations to motion to

$$\frac{d\mathbf{r}_i}{dt} = \frac{\mathbf{p}_i}{m_i} \quad (67)$$

$$\frac{d\mathbf{p}_i}{dt} = \mathbf{F}_i + (E_i - \bar{E})\mathbf{F}(t) - \frac{1}{2} \sum_j \mathbf{F}_{ij}[\mathbf{r}_{ij} \cdot \mathbf{F}(t)] + \frac{1}{2N} \sum_{j,k} \mathbf{F}_{jk}[\mathbf{r}_{jk} \cdot \mathbf{F}(t)] \quad (68)$$

where \bar{E} is the instantaneous average particle energy. If desired, a thermostat can be included. The second term on the right-hand side of the momentum equation shows how the heat current is driven. A particle with an energy greater than the average will move with the applied field, while a particle with an energy less than the average value will move against the field. The last term on the right-hand side of the momentum equation ensures that momentum is conserved. These equations are valid for a system that contains a single mass species. More complicated expressions are required for multi-component systems [99].

By assuming that the applied field is constant and in a convenient direction [i.e., $\mathbf{F}(t) = (F_x, 0, 0)$] linear response theory and the GK expression for the thermal conductivity, Eq. (49), can be used to show that the thermal conductivity can be given by

$$k = \lim_{t \rightarrow \infty} \lim_{F_x \rightarrow 0} \frac{\langle S_x(t) \rangle}{F_x TV} \quad (69)$$

This technique has been used in simulations of a one-dimensional anharmonic lattice [100], clathrate hydrates [87], carbon nanotubes [79,82], LJ argon [64,98], uranium dioxide [64], and zeolites [75].

In the evaluation of the time limit of Eq. (69), Berber *et al.* [79] find good convergence for carbon nanotubes, while the results of Motoyama *et al.* [64] show large fluctuations about the mean value. At the triple point of argon, Evans [98] finds a linear relation between the thermal conductivity and the applied field, making the evaluation of the F_x limit in Eq. (69) straightforward. Motoyama *et al.* also observe this behavior. Berber *et al.*, on the other hand, find that the thermal conductivity of carbon nanotubes increases as the applied field is decreased, and have a more difficult extrapolation to find the thermal conductivity. This may explain why their predictions are significantly higher than those from either the GK or direct methods [77,101]. Inoue *et al.* [87] and Motayama *et al.* do not find good agreement between the nonequilibrium GK predictions are those from the

equilibrium GK implementation. The reasons for the discrepancies are unclear. This result suggests that some caution should be exercised when using the nonequilibrium method.

C. QUANTUM CORRECTIONS

Before moving on to a discussion of the direct method for predicting the thermal conductivity, we first address the use of quantum corrections in the classical MD simulations. From the standpoint of lattice dynamics, there are two significant points to consider. First, as described in Section VI, the energy of the phonon modes is quantized in units of $\hbar\omega_k$. This is not true of the classical system, where the mode energies are continuous. The second point, and the focus of this section, is the temperature dependence of the mode excitations. As predicted by the Bose–Einstein distribution, there are significant temperature effects in the quantum system that are not present in a classical description. The MD approach is thus not suitable near and below the maximum in the crystal phase thermal conductivity (observed experimentally around one-tenth of the Debye temperature [102], and for argon at a temperature of 6 K [103]), where quantum effects on the phonon mode populations are important. The thermal conductivity in this region is also strongly affected by impurities and boundary effects, which are not considered here. As such, an MD simulation of a perfect crystal with periodic boundary conditions will lead to an infinite thermal conductivity at zero temperature, as opposed to the experimental value, which goes to zero.

The classical nature of the MD simulations is perhaps most evident when considering the predicted specific heats (see Fig. 9), and how they differ from the quantum-mechanical calculations. The reason for the discrepancy is that in a classical-anharmonic system at a given temperature, all modes are excited approximately equally. The expectation value of the mode energy is about $k_B T$. In a harmonic system, the excitation is exactly the same for all modes, and the expectation value of the energy is exactly $k_B T$. In the quantum system, there is a freezing out of high-frequency modes at low temperatures. Only above the Debye temperature are all modes excited approximately equally. The quantum system also has a zero-point energy not found in the MD system.

There is no simple way to explicitly include quantum effects in the MD simulations. In fact, the whole idea behind the simulations is to save significant computational resources by ignoring quantum effects. That being said, some effort has been made to address the classical-quantum issue by mapping the results of MD simulations onto an equivalent quantum system. Using the results for the LJ fcc crystal, one of these approaches [60,69,71,104] is presented and assessed here. The main idea is to scale the

temperature and thermal conductivity (after the simulations have been completed) using simple quantum-mechanical calculations and/or arguments. For the remainder of this section, T_{MD} and k_{MD} are used to represent the temperature and thermal conductivity of the MD system, and T_{real} and k_{real} are used to represent the values for the “real”, quantum system.

The temperature in the MD system is calculated from the relation

$$\left\langle \sum_i \frac{1}{2} m_i |\mathbf{v}_i|^2 \right\rangle = \frac{3}{2} (N - 1) k_B T_{MD} \quad (70)$$

which equates the average kinetic energy of the particles (summed over the index i) to the expectation value of the kinetic energy of a classical system [see Eq. (11)]. For a harmonic system, where equipartition of energy exists between the kinetic and potential energies, and between the modes, the total system energy will be given by $3(N - 1)k_B T_{MD}$. The temperature of the real system is found by equating this energy to that of a quantum phonon system, such that [60,69]

$$3(N - 1)k_B T_{MD} = \sum_k \hbar\omega_k \left[\frac{1}{2} + \frac{1}{\exp(\hbar\omega_k/k_B T_{real}) - 1} \right] \quad (71)$$

where the summation is over the k normal modes of the system. A similar relation has been proposed without the zero-point energy included [i.e., the factor of $\hbar\omega_k/2$ on the right-hand side of Eq. (71) is not considered] [71,104].

For the thermal conductivity, it has been proposed [60,69,71] that the heat flux, \mathbf{q} , in the classical and quantum systems should be the same. Written in one dimension,

$$q = -k_{MD} \frac{dT_{MD}}{dx} = -k_{real} \frac{dT_{real}}{dx} \quad (72)$$

such that

$$k_{real} = k_{MD} \frac{dT_{MD}}{dT_{real}} \quad (73)$$

The predicted T_{MD} and dT_{MD}/dT_{real} curves for the cases of both including and neglecting the zero-point energy are shown in Fig. 29(a). The data are plotted up to a temperature of 87 K, the melting point of the MD system.

When the zero-point energy is included, the MD simulations are only of interest at temperatures of 31.8 K and higher. This is an indication of the magnitude of the zero-point energy. The T_{MD} curve approaches T_{real} as the temperature is increased and more modes are excited in the quantum

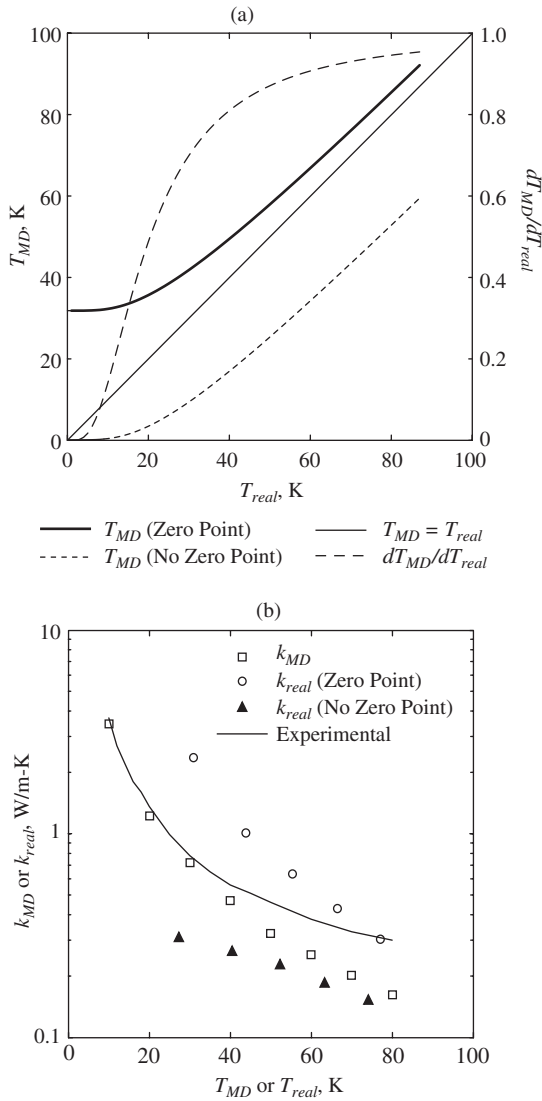


FIG. 29. (a) Temperature and thermal conductivity scaling relations. (b) Scaled thermal conductivities with raw MD predictions and experimental data.

system. The value of T_{MD} will always be higher than T_{real} because of the zero-point energy. The thermal conductivity scaling factor starts at zero. This ensures that the thermal conductivity will be zero at zero temperature. As the temperature increases, the scaling factor approaches unity.

When the zero-point energy is not included, the temperature scaling has the same shape as before, but has been shifted downward. In this case, T_{MD} will always be lower than T_{real} because of the manner in which the energy distributes in the modes of the quantum system. The T_{MD} value of zero is relevant in this case, because the associated quantum system can have zero energy. The thermal conductivity scaling factor is identical to when the zero-point energy is included, as the energies only differ by a constant.

The scaled thermal conductivities and unscaled MD predictions are shown in Fig. 29(b) along with the experimental data. To obtain these results, the T_{real} values corresponding to the available T_{MD} values are obtained. Owing to the nature of the scaling relation, not all the T_{MD} values have a corresponding T_{real} . The appropriate thermal conductivity scaling factor is then determined. Overall, the agreement with the experimental data worsens for either of the scaling possibilities compared to the raw MD data. Others have found an improved agreement (Li *et al.* [60] for β -silicon carbide including the zero-point energy, and Volz and Chen [71] for silicon, not including the zero-point energy). This lack of consistency raises a high level of doubt about the validity of this approach, and its possible widespread acceptance.

The main idea behind this somewhat ad hoc temperature scaling procedure is to map the classical MD results onto an equivalent quantum system. By not including the zero-point energy, a true quantum system is not being considered. For this reason, if such corrections are to be used, the zero-point energy should be included.

As it stands, there are a number of ways by which this method could be improved. These are related to the harmonic nature of the energy calculations on both sides of Eq. (71). The classical energy is based on an assumption of equipartition of energy. The average, total energy of the MD system is in fact less than $3(N - 1)k_B T_{MD}$ due to anharmonic effects (see Fig. 17). As shown there, at a temperature of 20 K, the deviation is 2.6%, and increases to 12.6% at a temperature of 80 K. This correction is straightforward to implement. The phonon space energy is most easily calculated using the zero temperature, harmonic dispersion relation (see Section III.D.3). As shown in Section III.D.5, temperature has a significant effect on the phonon dispersion, and temperature-dependent normal modes would make the temperature scaling more rigorous.

That being said, it is unlikely that these modifications would lead to a much improved model. The main drawback of this temperature/thermal conductivity scaling approach, as discussed by Li [17], is that it is a post-processing step that maps the entire MD system onto a quantum description. The effects are in practice manifested on a mode by mode basis, and how the energy is distributed, therefore making corrections on an

integrated level simply not suitable. Li goes on to suggest a way by which the classical MD system can be linked to a quantum description through the BTE.

Che *et al.* [77] have taken a more general approach to investigate the classical-quantum issue by comparing the general forms of the classical and quantum HCACFs. They do not find evidence to support the use of quantum corrections with MD thermal conductivity predictions. They argue that this is because long wavelength phonons are the dominant contributors to the thermal transport, which are active even at low temperatures. This is in contrast to the specific heat, where it is the high-frequency (short wavelength) modes that get excited as the temperature of the quantum system is increased, and lead to the significant temperature dependence up to the Debye temperature.

As discussed, the MD simulations are classical because it is within this framework that computational costs become reasonable enough to perform simulations of big systems, or for long times. When comparing the results of MD simulations to experiments, there are additional factors beyond their classical nature that need to be considered. These include the interatomic potential used, size effects, and the simulation procedures. It is difficult to isolate these effects. Efforts are needed on all fronts to increase the confidence in the results of MD simulations.

VI. Thermal Conductivity Prediction: Direct Method

A. INTRODUCTION

The direct method is a nonequilibrium, steady-state approach to predicting the thermal conductivity. By imposing a one-dimensional temperature gradient on a simulation cell and measuring the resulting heat flux (or, imposing a heat flux and measuring the resulting temperature gradient), one can predict the thermal conductivity using the Fourier law, Eq. (1). The direct method has a physical intuitiveness not present in the GK approach, and is analogous to an experimental technique. While experimentally it is easiest to apply a known heat flux and let the temperature distribution develop, in MD simulations different setups have been investigated, and are discussed in this section.

In all implementations of the direct method, energy flows from a hot region (the hot slab) to a cold region (the cold slab) of the simulation cell. Between the hot and cold slabs is the sample region, where a temperature gradient develops. This is realized by modifying the equations of motion in the hot and cold slabs. How this is done, and how the boundaries/interfaces in the system are treated has been extensively studied, and is reviewed here.

The modifications to the equations of motion must conserve momentum, or the system will drift. Energy conservation is not critical. The boundary modeling should be as physical as possible (i.e., there should be no effect in bulk phase predictions, but an effect should be present in a finite structure, such as a thin film). The goal is to obtain a result as close as possible to that which would be measured experimentally.

In the GK method, the MD system runs in the *NVE* ensemble and the thermal conductivity is predicted in a post-processing calculation. In the direct method, the thermal conductivity is predicted directly from the simulations, and the simulator has a greater impact on the value obtained. One must make decisions regarding simulation parameters. Consider the case of applying a temperature difference across the sample region by fixing the temperatures of the hot and cold slabs. Thermal conductivity is a temperature-dependent quantity; if a large temperature difference is present, there will be a gradient in the thermal properties across the sample region. It is not obvious if the predicted thermal conductivity will correspond to that for the average temperature in the system. A large temperature difference may also result in a nonlinear response, making the Fourier law, which requires a linear temperature profile, invalid. Given the large temperature gradients and heat fluxes manifested in such simulations (of order 10^9 K/m and 10^{12} W/m²), it is somewhat surprising that the response does in fact turn out to be generally linear. Conversely, if too small a temperature difference is present, it may be difficult to get a good prediction of the thermal conductivity because of fluctuations inherent to the system.

Consider Fig. 30(a), where temperature profiles obtained by Muller-Plathe [105] for an LJ fluid are shown. For the smallest temperature difference considered, shown in Fig. 30(b), the uncertainty at each point is larger than the total temperature change. As the temperature difference increases, the magnitude of these errors should not be significantly affected, which will allow for a more accurate prediction. In Fig. 31, the thermal conductivity of *t*-ZrO₂ at a temperature of 1450 K as a function of the applied temperature difference is shown [106]. There is a clear effect. One should ideally create such a plot for all cases considered, and perform an extrapolation to zero-temperature difference. At the same time, this will significantly increase the required computational time. There are other corrections than can be made in the direct method to get the best possible value for the thermal conductivity. These include accounting for size effects, as will be discussed in Section VI.C. In the end, there is always a compromise to be made between accuracy and reasonable computation times. The works of Schelling *et al.* [61], Lukes *et al.* [107] and Chantrenne and Barret [108] address many of the important methodological issues associated with the direct method.

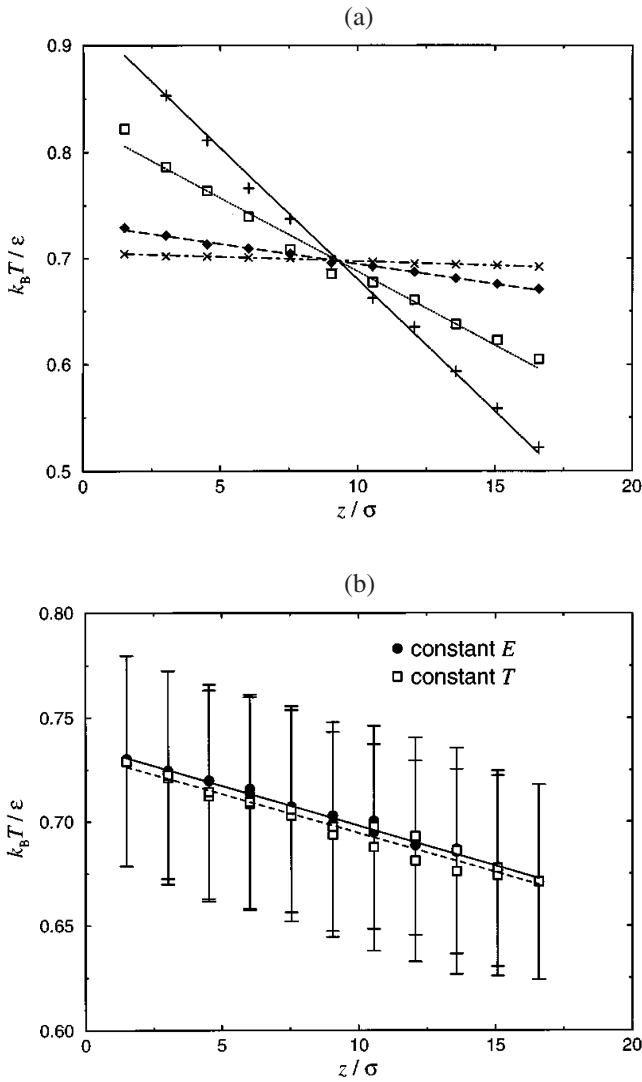


FIG. 30. (a) Temperature profiles in an LJ fluid. The profiles remain reasonably linear at large overall temperature differences. (b) Uncertainty in the temperatures for a small temperature difference. The uncertainty is larger than the overall temperature difference. The results show that applying either NVE or NVT statistics to the sample region does not affect the results. From Muller-Plather [105]. Copyright (1997), with permission from American Institute of Physics.

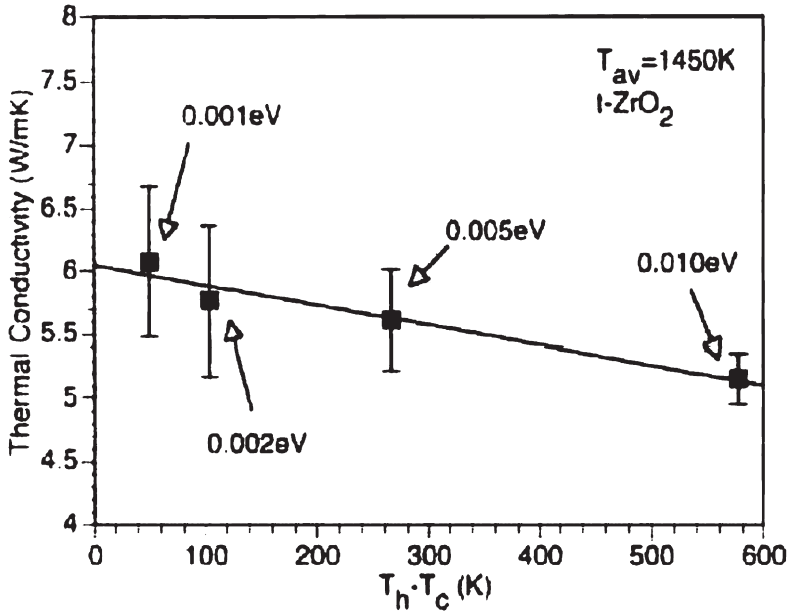


FIG. 31. Effect of the applied temperature difference on the thermal conductivity of *t*-ZrO₂. The average temperature is 1450 K. From Schelling and Phillpot [106]. Copyright (2001), with permission from Blackwell.

B. IMPLEMENTATION

One can classify implementations of the direct method into two types: applied temperature gradient or applied heat flux. Within each of these, two different simulation cell setups can be used. In one case, shown in Fig. 32(a), a system of finite length in the direction of the heat flow is used, with periodic boundary conditions in the transverse directions. Such an approach is useful for finite-sized structures, such as thin films. Energy flows in one direction. Alternatively, periodic boundary conditions can be applied in the direction of the heat flow, as shown in Fig. 32(b). This is advantageous for the simulation of a bulk phase, as one does not need to consider how the atoms at the ends will be modeled. Here, there is energy flow from both sides of the hot slab.

Because of boundary effects, the temperature gradient in the sample region may not be the same as that suggested by the hot and cold slab temperatures. A temperature discontinuity or nonlinearity may exist at the interfaces with the sample region. An example of this is shown for silicon at a temperature of 500 K in Fig. 33 [61]. As such, the temperature gradient should be calculated from the temperature profile away from the slabs. Measurement of the

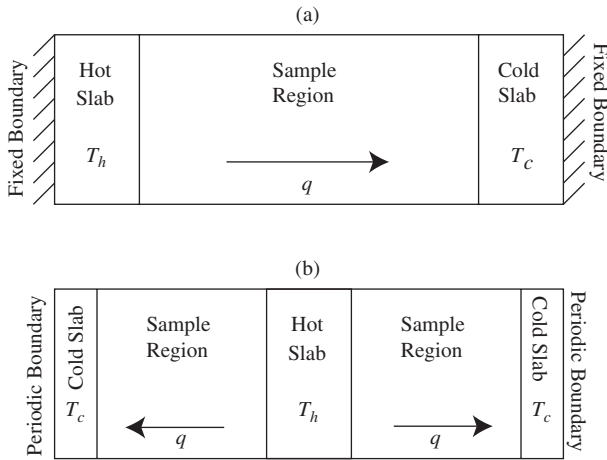


FIG. 32. Implementation of the direct method with (a) fixed end boundaries and (b) periodic boundary conditions.

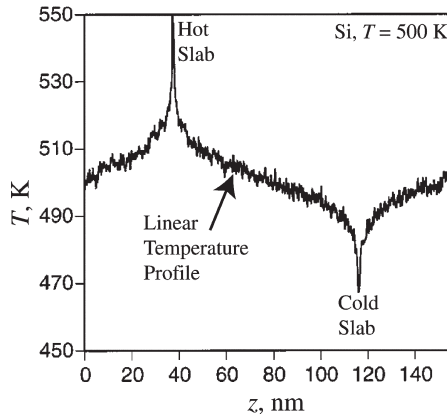


FIG. 33. Temperature profile in silicon at an average temperature of 500 K. The temperature profile around the hot and cold slabs is strongly nonlinear. The temperature gradient should be fit in the linear region. From Schelling *et al.* [61]. Copyright (2002), with permission from American Physical Society.

temperature along the sample region is thus required in both the temperature gradient and heat flux methods. The temperature gradient is found by applying a linear fit to the temperature data. The sample region is typically divided into thin slabs, each containing a few layers of atoms. Over such

distances and in the imposed state of nonequilibrium, the validity of a local temperature may be questionable. It has been found, however, that provided a long enough time is considered (typically on the order of a few hundred thousand time steps) and the layer is wide enough (at least four unit cells) that reasonable results and convergence are found. Chantrenne and Barrat [108] find that the departure from equilibrium is in fact quite small. The phonon densities of states for an equilibrium system and one that is thermostated are found to be indistinguishable, and the velocity distributions throughout the simulation cell are found to follow Maxwell–Boltzmann statistics. In general, for a given length of simulation cell, one must make a choice between the width of the slabs (more atoms will give better statistics at a given point) and the number of slabs (more points in the temperature profile will give a better fit to the gradient).

1. *Applied Temperature Gradient*

Two general approaches have been used to apply a temperature gradient to an MD cell. In simulations of a two-dimensional LJ lattice, Mountain and MacDonald [109] scale the velocities in the hot and cold slabs to achieve the desired temperatures. This is equivalent to a thermostat that keeps the kinetic energy constant. Such an approach has also been used for simulations of a two-dimensional Penrose tiling [110], amorphous and crystalline selenium and silica [111], carbon nanotubes [101,112,113], and LJ materials [108]. Poetzsch and Bottger [114] impose a temperature difference by placing the hot and cold slabs in contact with hot and cold reservoirs using Nose–Hoover thermostats. They use this approach to study a two-dimensional elastic percolating system and the roles played by anharmonicity and disorder in the associated thermal transport. The results are in agreement with predictions from the Green–Kubo method. Imamura [115] uses this method to study GaAs/AlAs superlattices. This method is less intrusive than the direct temperature scaling approach, and will produce the temperature fluctuations associated with the NVT ensemble. These fluctuations may be detrimental to achieving convergence, however. A similar strategy has been developed by Tenenbaum *et al.* [116] in which fixed walls at constant temperature at the system boundaries interact with the nearby atoms. Maruyama's [117] phantom technique is of the same spirit, and was used to model carbon nanotubes [118]. In all of the above approaches, the heat flux is found by calculating the difference in kinetic energy before and after the adjustments of the velocities. The heat flux will not be constant at every time step, and needs to be averaged over time. Michalski [110] finds good agreement between the heat current calculated with the kinetic energy change and that from Eq. (49).

2. Applied Heat Flux

Studies have reported slow convergence times for the applied temperature difference method [107]. The alternative is to apply a known heat flux. In one approach, this is accomplished by adding/removing a constant amount of energy, $\Delta\epsilon$ to/from the cold/hot slab at a regular interval. By taking this interval to be one time step, a constant heat flux will be achieved. Jund and Julien [119], in a study of amorphous silica, do this by computing the new velocities in the hot and cold regions, \mathbf{v}'_i , from

$$\mathbf{v}'_i = \mathbf{v}_G + \left(1 \pm \frac{\Delta\epsilon}{E_G}\right)^{1/2} \quad (74)$$

Here, \mathbf{v}_G is the velocity of the center of mass of the hot/cold slab, and E_G the difference between the slab's actual kinetic energy and that which its center of mass would have if it were a single particle. This implementation ensures that momentum is conserved. It has been used in studies of zirconia and yttria-stabilized zirconia [106], silicon [61], quartz [120], and metals [121].

Alternatively, new velocities can be calculated from

$$\mathbf{v}'_i = R\mathbf{v}_i + \mathbf{v}_{sub} \quad (75)$$

where R and v_{sub} are different for the hot and cold slabs, change at every time step, and are chosen to conserve momentum as described by Ikeshoji and Hafskjold [122]. Lukes *et al.* [107] used this approach to predict the thermal conductivity of thin LJ films and the corresponding bulk phase. A detailed analysis of the errors in the predicted temperature gradient, heat flux, and thermal conductivity are presented. They find that the applied heat flux does not always match that measured in the sample region due to leakage in the transverse directions. By running sufficiently long simulations, agreement between the two values is found to within 4%. Subsequent work using this approach in LJ systems has considered the effect of porosity [123], and two-component systems and nanostructures [124–126]. It has also been used to investigate the phonon contribution to the thermal conductivity of zirconium hydride [127]. Kotake and Wakuri [128] used a modified version of this approach to model a two-dimensional system where both the kinetic and potential energies are modified.

An alternative to the energy addition/removal has been used by Muller-Plathe [105]. Instead of specifying the amount of energy to be added or removed, the velocity vector of the coldest atom in the hot region and the hottest atom in the cold region are exchanged at a regular time interval. This approach conserves both energy and momentum, although it results in a

variable heat flux, which must be averaged over time. It has been used to predict the thermal conductivity of fluids [105,129].

3. *Transient Thermal Diffusivity Approach*

Daly *et al.* [130,131] have developed a variation on the direct method where a sinusoidal temperature perturbation is applied to a long MD simulation cell. The decay of the perturbation is observed, and used with the energy equation to calculate the thermal diffusivity, from which the thermal conductivity can be calculated. Agreement between their predictions for the cross-plane thermal conductivity of a simplified model of a GaAs/AlAs superlattice and predictions from the temperature gradient method has been found by Imamura *et al.* [115].

C. SIZE EFFECTS

In the GK method, all phonon modes are nonlocalized, and size effects are most likely an effect of not having enough modes present to establish an accurate description of the scattering processes [11]. A few thousand atoms are typically enough to overcome such size effects. When the direct method is used to predict the bulk thermal conductivity, the predicted value is found to increase as the length of the sample in the direction of the heat flow increases. One finds size effects even when tens of thousands of atoms are considered, and in amorphous materials, where the mean free path is expected to be small. Size effects are a result of three possible factors. First, the finite size of the simulation cell may not allow phonon modes to naturally decay (i.e., the length is shorter than the mean free path). Second, long wavelength modes cannot exist. Third, there is a thermal boundary resistance at the interface between the hot and cold slabs and the sample region. Based on GK predictions, the first and third factors are likely responsible for observed size effects. To find the true bulk thermal conductivity, the results must be extrapolated to what would be present in a simulation cell of infinite length.

To motivate how this can be done, Schelling *et al.* [61] consider a simple description of the phonon scattering where the mean free path is calculated using the Matheson rule, taking into account inter-phonon interactions and boundary scattering such that

$$\frac{1}{\Lambda} = \frac{1}{\Lambda_{\infty}} + \frac{4}{L} \quad (76)$$

Here, Λ is the mean free path in the finite system of length L , and Λ_{∞} the mean free path in an infinite system. The factor of 4 in the numerator of the

boundary scattering term is a result of their simulation cell setup. By taking the thermal conductivity to be given by Eq. (3), Eq. (76) can be recast as

$$\frac{1}{k} = \frac{3}{\rho C_v v} \left(\frac{1}{\Lambda_\infty} + \frac{4}{L} \right) \quad (77)$$

suggesting that one should plot $1/k$ vs. $1/L$ and extrapolate to $L = 0$. The slope of this curve will have units of W/K, and can be interpreted as the boundary thermal resistance [110,114], which should be constant for large unit cells. This procedure has been found to work quite well (the curve is often very close to linear), and has been used in numerous investigations [61,108,110,111,114,120,121]. Results for silicon and diamond from Schelling *et al.* [61] are shown in Fig. 34.

That being said, some investigations of bulk systems have ignored size effects, and the presented results should be viewed cautiously. In some cases the authors acknowledge the existence of size effects, and instead of using computational resources to get extrapolated thermal conductivity values for all conditions considered, instead focus on one size, and vary other parameters, such as the number of layers in a superlattice.

In simulations of amorphous silica, Jund and Jullien [119] do not take size effects into account as discussed above, but do correct their low-temperature results (between 8 and 20 K) to account for the low-frequency modes that are not present in the simulation cell, but are expected to play a significant role in the low-temperature transport. This results in a marked improvement in the agreement between their results and experimental data. At very low temperatures (< 8 K) the quantum effects in the experimental data are not

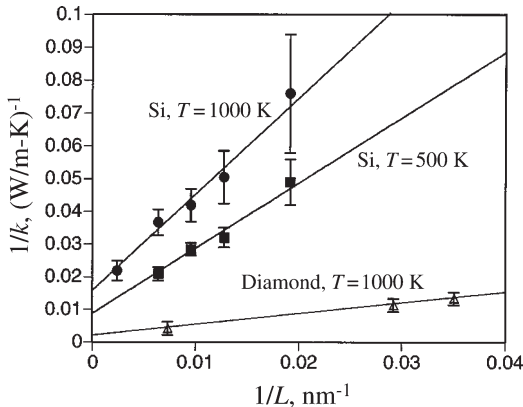


FIG. 34. System size dependence of thermal conductivity for silicon and diamond. From Schelling *et al.* [61]. Copyright (2002), with permission from American Physical Society.

reproducible, as would be expected. The temperature profiles they obtain at the low temperatures have strong nonlinearities, which seem to be a result of the dominance of boundary scattering. They use all of the temperature data in fitting the temperature gradient, however, which may have led to some of their results being overpredicted (see their Fig. 2). As discussed, one should neglect the temperatures near the boundaries when fitting the temperature profile. Oligschleger and Schon [111] find size effects for amorphous silica (although, interestingly, not for amorphous selenium), albeit with a different interatomic potential. The Jund and Jullien thermal conductivities are higher than those predicted with the GK method with the same potential by McGaughey and Kaviany [34] but in good agreement with experimental data. Considering size effects would increase their predicted thermal conductivities.

For an LJ system, increasing the lateral size beyond four conventional unit cells has not been found to have a significant effect on the predicted thermal conductivity [107]. Computational resources are better spent on longer simulation times to achieve better convergence. This result can be interpreted in the same way that the general lack of size effects in the GK method is explained; the system is bulk in the two transverse direction, and only a few modes are needed to establish representative scattering. In a finite structure, such as a nanowire, is to be simulated, this size will have a significant effect.

VII. Discussion

A. NOTABLE WORK

Many GK studies have considered the effect of defects on thermal transport, including potassium chloride doped with rubidium [59], krypton impurities and vacancies in LJ argon [67], defects in diamond [77], and yttria-stabilized zirconia [106]. Li *et al.* [60] considered a range of point defects in β -SiC, and investigated the resulting density of states at both system and species levels. Ishii *et al.* [84] investigated isotope effects in germanium, and Murakawa *et al.* [73] performed a similar study with silicon. By choosing a sample with the typical experimental concentration of isotopes, Murakawa *et al.* find much better agreement with experimental thermal conductivity data than that found with pure Si²⁸ [70].

In all cases, as is found experimentally, defects reduce the thermal conductivity and its temperature dependence. In the GK method, the change is observed in the form of the HCACF, which decays much faster than in the perfect crystal. A similar thermal conductivity reduction and temperature independence was found in zeolite crystals [34]. In such materials, the large unit cells localize energy, preventing long-range

correlations from developing. This phenomenon leads to a small, near temperature-independent value of the thermal conductivity, which has been interpreted as a thermal conductivity limit. The temperature independence does not appear to be a result of the classical nature of the simulations as temperature-dependent amorphous phase thermal conductivities have been reported [34,69,111,119]. The increasing thermal conductivity of amorphous materials with increasing temperature can be attributed to the temperature dependence of the specific heat (a quantum effect). The mean free path is assumed constant. One cannot use this explanation to analyze results from MD simulations.

Simulations of amorphous materials have allowed for an investigation of the role of disorder and anharmonicity in phonon transport. Unlike in the crystal phase, where all modes are nonlocalized (diffusive), in an amorphous structure localized, diffusive, and propagating modes exist (locons, diffusions, and propagons). These can be identified in MD simulations and used to interpret the thermal transport [61,110,132]. In a crystal, increased anharmonicity at higher temperature increases phonon scattering, reducing the thermal conductivity. In an amorphous material, anharmonicity enhances the energy exchange between localized modes, resulting in an increase in the thermal conductivity.

Dong *et al.* [83] used MD and the GK method to address the connection between dispersion and thermal transport in the prediction of the thermal conductivity of germanium-based materials. In their Fig. 1, they show the dispersion curves for a diamond structure, a clathrate cage, and for the same cage structure filled with strontium atoms. While the range of frequencies accessed by the vibrational modes in these structures is comparable, the dispersion characteristics differ. The large unit cell of the clathrate cage significantly reduces the frequency range of the acoustic phonons, the carriers generally assumed to be most responsible for thermal transport. This results in an order of magnitude reduction in the thermal conductivity. In the filled cage, the guest atoms have a natural frequency that cuts directly through the middle of what would be the acoustic phonon branch. The thermal conductivity is reduced by a further factor of 10. McGaughey *et al.* [66], by analyzing the predicted thermal conductivities together with the frequency spectra of the HCACF and quasi-harmonic phonon dispersion curves, link the thermal transport in a two-atom LJ system to the lattice dynamics.

The direct method applies well to the study of thin films, where size effects are of great interest. Anderson and Tamma [133] have reviewed techniques for predicting the thermal conductivity of thin films using BTE and MD approaches. In such simulations, the treatment of the film boundaries and the hot and cold slabs is important, and different methods have been

considered [107,108]. Generally, the conductivity of a thin film is less than the corresponding bulk value; it increases as the film thickness increases and the relative contribution of boundary scattering to the thermal resistance decreases.

A natural extension of the study of thin films is an investigation of superlattices. Interfacial scattering strongly affects the thermal transport, and the periodicity of the superlattice modifies the dispersion through zone folding. Qualitative differences exist between experimental results and theoretical predictions. Studies have been performed on LJ materials [124–126], GaAs/AlAs [115,130,131] and Ge/Si [89], investigating effects including interfacial strain, number of layers, layer thickness, and interface roughness. Temperature discontinuities are found at the interfaces, indicative of thermal boundary resistance. In general, the number of layers has an insignificant effect. The layer thickness does have an effect though, as that parameter affects the relative contributions of the interfaces and the layers to the total thermal resistance.

Carbon nanotubes of differing size and chirality have been investigated using both the GK and direct methods [78–82,101,118]. The predicted thermal conductivities are very large (room temperatures values of thousands of W/mK) and there is significant scatter between different investigations. Different factors might be responsible for this scatter, many of which were discussed in previous sections. As the length of the nanotube increases, its thermal conductivity diverges. With the exception of the work of Maruyama [118], all studies reporting temperature dependence see a peak in the thermal conductivity. This behavior is strange, as the peak is generally interpreted as a quantum effect. In this case, it is most likely related to the two-dimensional nature of the nanotube. Osman and Srivastava [101] find that the location of the peak shifts to higher temperature as the diameter of the nanotube increases, a result they attribute to the effects of Umklapp processes and radial phonons. A comparison of a (10,0) tube and a (5,5) tube, which have the same diameter, shows no significant chirality dependence of the thermal conductivity. Che *et al.* [78] considered the effects of defects and vacancies in a (10,10) nanotube.

Beyond straight, single-walled nanotubes, Noya *et al.* [112] studied the effect of placing fullerene (C_{60}) molecules inside a (10,10) nanotube (a peapod). The thermal conductivity is larger than the bare nanotube value, consistent with experimental results. They attribute this result to energy transfer to the fullerene molecules by the radial vibrations of the nanotube, and subsequent transfer between the fullerenes. Cummings *et al.* [113] studied a Y-junction nanotube [(14,0) \rightarrow (7,0), (7,0)] using the direct method. They find a temperature discontinuity at the junction, lowering the thermal conductivity. The addition of defects to the straight (14,0) nanotube

also produces a temperature discontinuity. While the electrical conductivity of such junctions has been found to be current-direction-dependent, this effect is not found for the thermal conductivity.

B. COMPARISON OF GREEN–KUBO AND DIRECT METHODS

Both the GK and direct methods have been used extensively to study thermal transport in dielectric materials and to predict their thermal conductivities. Surprisingly, few studies exist that directly compare the two approaches. Schelling *et al.* [61] predicted the thermal conductivity of silicon at a temperature of 1000 K using both methods, and found good agreement. Poetzsch and Bottger [114] also found good agreement between the two approaches in a two-dimensional elastic percolating system. Below, we qualitatively compare the two methods.

- The GK calculations are based on an equilibrium system. Implementation has no effect on the particle dynamics, and the system temperature will be uniform and constant. In the direct method, the system is perturbed to a steady-state, nonequilibrium configuration. The equations of motion of the atoms in the hot and cold slabs are modified. A temperature gradient exists, and one must check for linear system response.
- Implementation of the GK method is well defined. One must use subjective judgement in deciding how to specify the integral of the HCACF (see Section V.B.1). In the direct method, one must make more decisions. Because of this, significant time may be needed to “tune” the simulations, and comparing results of different investigations may be difficult.
- In the GK method, hundreds or thousands of atoms are required to eliminate size effects. Multiple simulations from different initial conditions (each on the order of one million time steps) are needed for good convergence of the HCACF and thermal conductivity. When simulating a bulk material using the direct method, one must use simulation cells of different lengths to account for size effects. The largest cells may contain tens or hundreds of thousands of atoms. Only one simulation is required for each configuration, which may need a few hundred thousand time steps to reach convergence.
- In both methods, the biggest challenge is overcoming noise inherent to the simulations. In the GK method, noise can lead to a HCACF integral that is difficult to specify. The challenge in the direct method is calculating the temperature gradient and the heat flux. In both approaches it helps to run longer simulations (or simulations from different initial conditions for GK).

- The GK method provides the full thermal conductivity tensor. One can also use the simulations to investigate phonon dynamics and to predict other properties, like the specific heat. In the direct method, the thermal conductivity is only predicted in one direction, and the imposed nonequilibrium limits access to extra information.

Because of size effects and computational demands associated with the direct method, we believe the GK method should be used to predict bulk phase thermal conductivity. One exception is for materials whose HCACF does not converge neatly to zero (e.g., silicon [61]). The direct method is ideal for studying finite structures like thin films and superlattices; it allows for predictions of interfacial and boundary thermal resistances not possible in the GK method.

C. EXPECTATIONS FROM MOLECULAR DYNAMICS

The finite thermal conductivities predicted in MD simulations clearly indicate that inter-phonon interactions are present. The discussion in Section IV indicates that the nature of the phonon transport in small MD systems differs from that in a particle-based description. This does not mean, however, that one should expect large differences between experimental results, predictions from a quantum model, and/or predictions from MD simulations. The nonlocalized description is a more general approach to the problem that could be applied to the quantum system. What to seek when addressing the issue of phonon transport in the MD system is a consistent framework in which to interpret the results of the classical simulations and those from a quantum-particle model.

The classical-quantum issue may lead to poor agreement in some properties at low temperatures due to freezing out of the high-frequency modes in the quantum theory. This is evident from the specific heat predicted by MD, which remains finite as temperature approaches zero. Regarding thermal conductivity prediction, some have argued [61,69,71] that above the Debye temperature the difference should not be significant. That said, classical simulations, run at temperatures significantly lower than this value, have reproduced experimental results reasonably well.

While agreement between MD thermal conductivity predictions and experimental data has been found in some cases, success is not universal. With large computational cells that eliminate size effects, MD simulations of diamond at a temperature of 300 K with the GK method predict a thermal conductivity of 1,200 W/m K [77]. This is almost half the experimental value of 2300 W/m K. On the other hand, MD simulations of germanium with the GK method over-predict the experimental room-temperature thermal

conductivity of 63 W/mK by a factor of 2 [83]. When MD results over-predict the experimental thermal conductivity, one often assumes it is because the MD system contains no impurities, removing a source of phonon scattering. When MD under-predicts the experimental results, one often assumes it is because the simulation cell was too small to capture long-wavelength phonons. One can take size effects into account, however, and very high-purity single crystals are available in experimental investigations. The question of the classical nature of the simulations also arises. Discrepancies between experimental data and MD predictions most likely result from the interatomic potential used. Because of this, many investigations still consider their efforts to be methodological in nature, or only good for qualitative predictions. To simulate real devices, MD must be applied as a predictive tool. As such, the development of new potentials must continue. The potential functions currently available are limited, and in some cases of dubious origin, especially when modeling thermal transport.

VIII. Concluding Remarks

We have presented a formulation for studying thermal transport in dielectric materials using MD simulations. The simulations allow for analysis in both the real and phonon spaces. The natural inclusion of anharmonic effects through the form of the interatomic potential presents a significant advantage over harmonic theories. We have described, examined, and compared the two major approaches for predicting thermal conductivity from MD simulations (the GK and direct methods). Each has advantages and disadvantages, and the method chosen strongly depends on the problem of interest. Generally, the GK method is superior for bulk phase simulations, while the direct method is best for finite structures. By no means are the simulations an exact representation of the real world; they are limited by their classical nature, the small systems sizes that must be considered for reasonable computational times, and the available interatomic potentials. Still, many investigations have found reasonable agreement with experimental data, and the simulations have allowed for atomic-level observations not otherwise possible – resulting in elucidation of interesting phenomena.

The exchange of energy between normal modes underlies all of the thermal transport behavior discussed. Without a fundamental knowledge of the nature of the transport, it may not be possible to understand how a complex crystal structure localizes energy, or to design a material with a specified thermal conductivity, or even to interpret the shapes of relaxation–time curves. To date, work in molecular simulation and thermal

transport seems to have skirted this issue entirely [11]. While phonons are often mentioned, little effort has been taken to observe them, or to investigate how energy flows in a frequency space whose discretization cannot be ignored.

In terms of applying MD simulations to real systems, current computational resources cannot accurately model anything close to a micron in size on an atom-by-atom level. The upscaling of MD results to larger length-scale models is a promising and exciting avenue. For example, the results of MD simulations can be used to parameterize the BTE expression for the thermal conductivity, allowing for predictions without the use of fitting parameters [28]. Upscaling has been applied in a different context to phonon transport across material interfaces by Schelling and Phillpot [51].

Acknowledgements

This work has been supported by the United States Department of Energy, Basic Energy Sciences Division under grant DE-FG02-00ER45851, the Natural Sciences and Engineering Research Council of Canada, and the Rackham Graduate School at the University of Michigan.

Nomenclature

a	lattice constant, constant	KE	kinetic energy
A	constant	l	wave packet size
B	constant	L	MD simulation cell size
c_v	specific heat at constant volume, J/K (either per particle or per mode)	m	mass
C_p	volumetric specific heat at constant pressure, J/kg K	n	number of atoms in unit cell
C_v	specific heat at constant volume, J/kg K	N	number of atoms
C	constant	p	probability distribution function
\mathbf{D}	dynamical matrix	\mathbf{p}	particle momentum vector
\mathbf{e}	normal mode polarization vector	P	pressure, function
E	energy (kinetic and potential)	\mathbf{q}, q	heat flux vector, heat flux
\mathbf{F}	force vector, forcing function	\mathbf{r}, r	particle position, inter-particle separation
g	radial distribution function	R	radius
\mathbf{G}	reciprocal space lattice vector	S	normal mode coordinate
\hbar	Planck constant/ 2π , 1.0546 $\times 10^{-34}$ J s	\mathbf{S}	heat current vector
k_B	Boltzmann constant, 1.3806 $\times 10^{-23}$ J/K	t	time
k	thermal conductivity	T	temperature
K	spring constant	\mathbf{u}, u	particle displacement from equi- librium
		\mathbf{v}, v	particle or phonon velocity
		V	volume
		x	$\hbar\omega/k_B T$

GREEK LETTERS

α	thermal diffusivity
ε	energy
ε_{LJ}	Lennard-Jones energy scale
η	unit cells in linear dimension, Nose-Hoover thermostat parameter
κ, κ	wave vector, wave number
λ	phonon wavelength
Λ	phonon mean free path
ν	polarization branch
ρ	density
σ_{LJ}	Lennard-Jones length scale
τ	time constant, relaxation time
ϕ, Φ	potential energy
Φ	force constant matrix
ω	angular frequency

SUBSCRIPTS

ac	acoustic
am	amorphous
c	cutoff
D	Debye
eff	effective
equ	equilibrium
FD	first dip
G	center of mass
$harm$	harmonic
i	summation index, particle label
j	summation index, particle label
k	summation index, particle label, phonon mode label, conduction label
l	label
lg	long range
LJ	Lennard-Jones

nm	nearest neighbor
o	self (referring to a particle), equilibrium
op	optical
r	relaxation
sh	short-range
sim	length of simulation
t	total
T	thermostat
u	convection
α, β, γ	$x, y,$ or z direction
0	zero-temperature equilibrium
1	related to single exponential fit
∞	bulk

SUPERSCRIPTS

*	complex conjugate, dimensionless
\sim	deviation from average value
$-$	instantaneous average
$'$	new (velocity)

ABBREVIATIONS

BTE	Boltzmann transport equation
BZ	Brillouin zone
CP	Cahill-Pohl
EF	exponential fit
fcc	face-centered cubic
FD	first dip
GK	Green-Kubo
HCACF	heat current autocorrelation function
LJ	Lennard-Jones
MD	molecular dynamics
RDF	radial distribution function
RMS	root mean square

References

1. Cahill, D. G., Goodson, K., and Majumdar, A. (2002). Thermometry and thermal transport in micro/nanoscale solid-state devices and structures. *J. Heat Transfer* **124**, 223–241.
2. Cahill, D. G., Ford, W. K., Goodson, K. E., Mahan, G. D., Maris, H. J., Majumdar, A., Merlin, R., and Phillpot, S. R. (2003). Nanoscale thermal transport. *J. Appl. Phys.* **93**, 793–818.

3. Ashcroft, N. W. and Mermin, N. D. (1976). "Solid State Physics". Saunders College Publishing, Fort Worth.
4. Srivastava, G. P. (1990). "The Physics of Phonons". Adam Hilger, Bristol.
5. Dove, M. T. (1993). "Introduction to Lattice Dynamics". Cambridge University Press, Cambridge.
6. Ziman, J. M. (2001). "Electrons and Phonons". Oxford University Press, Oxford.
7. Roth, J., Gahler, F., and Trebin, H.-R. (2000). A molecular dynamics run with 5 180 116 000 particles. *Int. J. Mod. Phys. C* **11**, 317–322.
8. Kadau, K., Germann, T. C., and Lomdahl, P. S. (2004). Large-scale molecular-dynamics simulation of 19 billion particles. *Int. J. Mod. Phys. C* **15**, 193–201.
9. Touloukian, Y. (1970). "Thermophysical Properties of Matter Volume 2". Plenum, New York.
10. Touloukian, Y. (1970). "Thermophysical Properties of Matter Volume 3". Plenum, New York.
11. McGaughey, A. J. H. (2004). Phonon Transport in Molecular Dynamics Simulations: Formulation and Thermal Conductivity Prediction. PhD Thesis, University of Michigan, Ann Arbor, MI.
12. Omini, M. and Sparavigna, A. (1996). Beyond the isotropic-model approximation in the theory of thermal conductivity. *Phys. Rev. B* **53**, 9064–9073.
13. Yu, R. C., Tea, N., Salamon, M. B., Lorents, D., and Malhotra, R. (1992). Thermal conductivity of single crystal C_{60} . *Phys. Rev. Lett.* **68**, 2050–2053.
14. Poulidakos, D., Arcidiacono, S., and Maruyama, S. (2003). Molecular dynamics simulation in nanoscale heat transfer: a review. *Micro. Therm. Eng.* **7**, 181–206.
15. Allen, M. P. and Tildesly, D. J. (1987). "Computer Simulation of Fluids". Clarendon, Oxford.
16. Frenkel, D. and Smit, B. (1996). "Understanding Molecular Simulation: From Algorithms to Applications". Academic Press, San Diego.
17. Li, J. (2000). "Modeling Microstructural Effects on Deformation Resistance and Thermal Conductivity". PhD Thesis, Massachusetts Institute of Technology, Cambridge, MA.
18. Ding, H.-Q., Karasawa, N., and Goddard, W. A. (1992). The reduced cell multipole method for Coulomb interactions in periodic-systems with million-atom unit cells. *Chem. Phys. Lett.* **192**, 6–10.
19. Ding, H.-Q., Karasawa, N., and Goddard, W. A. (1992). Atomic level simulations on a million particles – the cell multipole method for Coulomb and London nonbond interactions. *J. Chem. Phys.* **97**, 4309–4315.
20. Wolf, D., Keblinski, P., Phillpot, S. R., and Eggebrecht, J. (1999). Exact method for the simulation of Coulombic systems by spherically truncated, pairwise r^{-1} summation. *J. Chem. Phys.* **110**, 8254–8282.
21. McQuarrie, D. A. (2000). "Statistical Mechanics". University Science Books, Sausalito.
22. Nose, S. (1984). A molecular dynamics method for simulations in the canonical ensemble. *Mol. Phys.* **52**, 255–268.
23. Nose, S. (1984). A unified formulation of the constant temperature molecular dynamics method. *J. Chem. Phys.* **81**, 511–519.
24. Hoover, W. G. (1985). Canonical dynamics: equilibrium phase-space distributions. *Phys. Rev. A* **31**, 1695–1697.
25. Anderson, H. C. (1980). Molecular dynamics simulations at constant pressure and/or temperature. *J. Chem. Phys.* **72**, 2384–2393.
26. Parrinello, M. and Rahman, A. (1981). Polymorphic transitions in single crystals: a new molecular dynamics method. *J. Appl. Phys.* **52**, 7182–7190.

27. McGaughey, A. J. H. and Kaviany, M. (2004). Thermal conductivity decomposition and analysis using molecular dynamics simulations. Part I. Lennard-Jones argon. *Int. J. Heat Mass Transfer* **27**, 1783–1798.
28. McGaughey, A. J. H. and Kaviany, M. (2004). Quantitative validation of the Boltzmann transport equation phonon thermal conductivity model under the single-mode relaxation time approximation. *Phys. Rev. B* **69**, 094303-1-12.
29. Kaburaki, H., Li, J., and Yip, S. (1998). Thermal conductivity of solid argon by classical molecular dynamics. *Mater. Res. Soc. Symp. Proc.* **538**, 503–508.
30. Tretiakov, K. V. and Scandolo, S. (2004). Thermal conductivity of solid argon from molecular dynamics simulations. *J. Chem. Phys.* **120**, 3765–3769.
31. Einstein, A. (1911). Elementare betrachtungen uber die thermische molekularbewegung in festen korpern. *Ann. Phys.* **35**, 679–694.
32. Cahill, D. G. and Pohl, R. O. (1989). Heat flow and lattice vibrations in Glasses. *Solid State Commun.* **70**, 927–930.
33. Cahill, D. G., Watson, S. K., and Pohl, R. O. (1992). Lower limit to thermal conductivity of disordered crystals. *Phys. Rev. B* **46**, 6131–6140.
34. McGaughey, A. J. H. and Kaviany, M. (2004). Thermal conductivity decomposition and analysis using molecular dynamics simulations. Part II. Complex silica structures. *Int. J. Heat Mass Transfer* **27**, 1799–1816.
35. Ohara, T. (1999). Contribution of intermolecular energy transfer to heat conduction in a simple fluid. *J. Chem. Phys.* **111**, 9667–9672.
36. Greegor, R. B. and Lyle, F. W. (1979). Extended X-ray absorption fine structure determination of thermal disorder in Cu: comparison of theory and experiment. *Phys. Rev. B* **20**, 4902–4907.
37. Porter, L. J., Yip, S., Yamaguchi, M., Kaburaki, H., and Tang, M. (1997). Empirical bond-order potential description of thermodynamic properties of crystalline silicon. *J. Appl. Phys.* **81**, 96–106.
38. Kittel, C. (1996). “Introduction to Solid State Physics”, 7th ed. Wiley, New York.
39. Tschaufeser, P. and Parker, S. C. (1995). Thermal expansion behavior of zeolites and AlPO_4s . *J. Phys. Chem.* **9**, 10609–10615.
40. Tiano, W., Dapiaggi, M., and Artioli, G. (2003). Thermal expansion in cuprite-type structures from 10 K to decomposition temperature: Cu_2O and Ag_2O . *J. Appl. Crystallogr.* **36**, 1461–1463.
41. Pryde, A. K. A., Hammonds, K. D., Dove, M. T., Heine, V., Gale, J. D., and Warren, M. C. (1996). Origin of the negative thermal expansion in ZrW_2O_8 and ZrV_2O_7 . *J. Phys.: Condens. Matter* **8**, 10973–10982.
42. Fujii, Y., Lurie, N. A., Pynn, R., and Shirane, G. (1974). Inelastic neutron scattering from solid ^{36}Ar . *Phys. Rev. B* **10**, 3647–3659.
43. Bernandes, N. (1958). Theory of solid Ne, A, Kr, and Xe at 0°K. *Phys. Rev.* **112**, 1534–1539.
44. Callaway, J. (1959). Model for lattice thermal conductivity at low temperatures. *Phys. Rev.* **113**, 1046–1051.
45. Holland, M. G. (1963). Analysis of lattice thermal conductivity. *Phys. Rev.* **132**, 2461–2471.
46. Ladd, A. J. C., Moran, B., and Hoover, W. G. (1986). Lattice thermal conductivity: a comparison of molecular dynamics and anharmonic lattice dynamics. *Phys. Rev. B* **34**, 5058–5064.
47. Chung, J. D., McGaughey, A. J. H., and Kaviany, M. (2004). Role of phonon dispersion in lattice thermal conductivity. *J. Heat Transfer* **126**, 376–380.

48. Allen, P. B. and Feldman, J. L. (1993). Thermal conductivity of disordered harmonic solids. *Phys. Rev. B* **48**, 12581–12588.
49. Feldman, J. L., Kluge, M. D., Allen, P. B., and Wooten, F. (1993). Thermal conductivity and localization in glasses: numerical study of a model of amorphous silicon. *Phys. Rev. B* **48**, 12589–12602.
50. Schelling, P. K., Phillpot, S. R., and Keblinski, P. (2002). Phonon wave-packet dynamics at semiconductor interfaces by molecular-dynamics simulations. *Appl. Phys. Lett.* **80**, 2484–2486.
51. Schelling, P. K. and Phillpot, S. R. (2003). Multiscale simulation of phonon transport in superlattices. *J. Appl. Phys.* **93**, 5377–5387.
52. Sinha, S., Schelling, P. K., Phillpot, S. R., and Goodsen, K. E. (2005). Scattering of *g*-process longitudinal optical phonons at hotspots in silicon. *J. Appl. Phys.* **97**, 023702-1-9.
53. Green, M. S. (1954). Markoff random processes and the statistical mechanics of time-dependent phenomena. II. Irreversible processes in fluids. *J. Chem. Phys.* **22**, 398–413.
54. Kubo, R. (1957). Statistical mechanical theory of irreversible processes. I. General theory and simple applications to magnetic and conduction problems. *J. Phys. Soc. Japan* **12**, 570–586.
55. R. Zwanzig, (1965). Time-correlation functions and transport coefficients in statistical mechanics. In: “Annual Review of Physical Chemistry Volume 16”, (H. Eyring, C. J. Christensen, and H. S. Johnston, eds.), pp. 67–102 Annual Reviews, Palo Alto.
56. Helfand, E. (1960). Transport coefficients from dissipation in a canonical ensemble. *Phys. Rev.* **119**, 1–9.
57. Lindan, P. J. D. and Gillan, M. J. (1991). A molecular dynamics study of the thermal conductivity of CaF₂ and UO₂. *J. Phys. Condens. Matter* **3**, 3929–3939.
58. Gillan, M. J. (1991). The molecular dynamics calculation of transport coefficients. *Phys. Scripta* **T39**, 362–366.
59. Paolini, G. V., Lindan, P. J. D., and Harding, J. H. (1997). The thermal conductivity of defective crystals. *J. Chem. Phys.* **106**, 3681–3687.
60. Li, J., Porter, L., and Yip, S. (1998). Atomistic modeling of finite-temperature properties of crystalline β -SiC. II. Thermal conductivity and effects of point defects. *J. Nucl. Mater* **255**, 139–152.
61. Schelling, P. K., Phillpot, S. R., and Keblinski, P. (2002). Comparison of atomic-level simulation methods for computing thermal conductivity. *Phys. Rev. B* **65**, 144–306.
62. Vogelsang, R., Hoheisel, C., and Ciccotti, G. (1987). Thermal conductivity of the Lennard-Jones liquid by molecular dynamics calculations. *J. Chem. Phys.* **86**, 6371–6375.
63. Volz, S., Saulnier, J.-B., Lallemand, M., Perrin, B., Depondt, B., and Mareschal, M. (1996). Transient Fourier-law deviation by molecular dynamics in solid argon. *Phys. Rev. B* **54**, 340–347.
64. Motoyama, S., Ichikawa, Y., Hiwatari, Y., and Oe, A. (1999). Thermal conductivity of uranium dioxide by nonequilibrium molecular dynamics simulation. *Phys. Rev. B* **60**, 292–298.
65. Picu, R. C., Borca-Tasciuc, T., and Pavel, M. C. (2003). Strain and size effects on heat transport in nanostructures. *J. Appl. Phys.* **93**, 3535–3539.
66. A. J. H. McGaughey, M. I. Hussein, M. Kaviany, and G. Hulbert, (2004) Phonon band structure and thermal transport correlation in a two-atom unit cell. ASME paper IMECE2004-62328, presented at 2004 ASME International Mechanical Engineering Congress and Exhibition, Anaheim, CA, USA, November 13–19.
67. Chen, Y., Lukes, J. R., Li, D., Yang, J., and Wu, Y. (2004). Thermal expansion and impurity effect on lattice thermal conductivity of solid argon. *J. Chem. Phys.* **120**, 3841–3846.

68. Tretiakov, K. V. and Scandolo, S. (2004). Thermal conductivity of solid argon at high pressure and high temperature: a molecular dynamics study. *J. Chem. Phys.* **121**, 11177–11182.
69. Lee, Y. H., Biswas, R., Soukoulis, C. M., Wang, C. Z., Chan, C. T., and Ho, K. M. (1991). Molecular-dynamics simulation of thermal conductivity in amorphous silicon. *Phys. Rev. B* **43**, 6573–6580.
70. Volz, S. G. and Chen, G. (1999). Molecular dynamics simulation of thermal conductivity of silicon nanowires. *Appl. Phys. Lett.* **75**, 2056–2058.
71. Volz, S. G. and Chen, G. (2000). Molecular-dynamics simulation of thermal conductivity of silicon crystals. *Phys. Rev. B* **61**, 2651–2656.
72. Volz, S. and Perrin, B. (2002). Si crystal thermal conductance in the THz frequency range by molecular dynamics. *Physica B* **316–317**, 286–288.
73. Murakawa, A., Ishii, H., and Kakimoto, K. (2004). An investigation of thermal conductivity of silicon as a function of isotope concentration by molecular dynamics. *J. Cryst. Growth* **267**, 452–457.
74. J. Li, and S. Yip, (2005) Spectral method in thermal conductivity calculation. Submitted.
75. Murashov, V. V. (1999). Thermal conductivity of model zeolites: molecular dynamics study. *J. Phys: Condens. Mater* **11**, 1261–1271.
76. Hirotsaki, N., Ogata, S., Kocer, C., Kitagawi, H., and Nakamura, Y. (2002). Molecular dynamics calculation of the ideal thermal conductivity of single-crystal α - and β -Si₃N₄. *Phys. Rev. B* **65**, 134110-1-11.
77. Che, J., Cagin, T., Deng, W., and Goddard III, W. A. (2000). Thermal conductivity of diamond and related materials from molecular dynamics simulations. *J. Chem. Phys.* **113**, 6888–6900.
78. Che, J., Cagin, T., and Goddard III, W. A. (2000). Thermal conductivity of carbon nanotubes. *Nanotechnology* **11**, 65–69.
79. Berber, S., Kwon, Y.-K., and Tomanek, D. (2000). Unusually high thermal conductivity of carbon nanotubes. *Phys. Rev. Lett.* **84**, 4613–4616.
80. Grujicic, M., Cao, G., and Gersten, B. (2004). Atomic scale computations of the lattice contribution to thermal conductivity of single-walled carbon nanotubes. *Mater Sci. Eng. B* **107**, 204–216.
81. Shenogin, S., Bodapati, A., Xue, L., Ozisik, R., and Keblinski, P. (2004). Effect of chemical functionalization on thermal transport of carbon nanotube composites. *Appl. Phys. Lett.* **85**, 2229–2231.
82. Zhang, W., Zhu, Z., Wang, F., Wang, T., Sun, L., and Wang, Z. (2004). Chirality dependence of the thermal conductivity of carbon nanotubes. *Nanotechnology* **15**, 936–939.
83. Dong, J., Sankey, O. F., and Myles, C. W. (2001). Theoretical study of lattice thermal conductivity in Ge framework semiconductors. *Phys. Rev. Lett.* **86**, 2361–2364.
84. Ishii, H., Murakawa, A., and Kakimoto, K. (2004). Isotope-concentration dependence of thermal conductivity of germanium investigated by molecular dynamics. *J. Appl. Phys.* **95**, 6200–6203.
85. Yamada, K., Kurosaki, K., Uno, M., and Yamanaka, S. (2000). Evaluation of thermal properties of uranium dioxide by molecular dynamics. *J. Alloy Compd.* **307**, 10–16.
86. Kurosaki, K., Yano, K., Yamada, K., Uno, M., and Yamanaka, S. (2000). A molecular dynamics study of the thermal conductivity of uranium mononitride. *J. Alloy Compd.* **311**, 305–310.
87. Inoue, R., Tanaka, H., and Nakanishi, K. (1996). Molecular dynamics calculation of the anomalous thermal conductivity of clathrate hydrates. *J. Chem. Phys.* **104**, 9569–9577.

88. Koblinski, P., Phillpot, S. R., Choi, S. U. S., and Eastman, J. A. (2002). Mechanisms of heat flow in suspensions of nano-sized particles (nanofluids). *Int. J. Heat Mass Transfer* **45**, 855–863.
89. Volz, S., Saulnier, J. B., Chen, G., and Beauchamp, P. (2000). Computation of thermal conductivity of Si/Ge superlattices by molecular dynamics techniques. *Microelectr. J* **31**, 815–819.
90. Tretiakov, K. V. Personal communication.
91. Luchnikov, V. A., Medvedev, N. N., Naberukhin, Y. I., and Novikov, V. N. (1995). Inhomogeneity of the spatial distribution of vibrational modes in a computer model of amorphous argon. *Phys. Rev. B* **51**, 15569–15572.
92. Wolfing, B., Kloc, C., Teubner, J., and Bucher, E. (2001). High performance thermoelectric Tl_9BiTe_6 with extremely low thermal conductivity. *Phys. Rev. Lett.* **86**, 4350–4353.
93. Konstantinov, V. A. (2001). Manifestation of the lower limit to thermal conductivity in the solidified inert gases. *J. Low Temp. Phys.* **122**, 459–465.
94. Domingues, G., Saulnier, J.-B., and Volz, S. (2004). Thermal relaxation times and heat conduction in β -cristobalite and α -quartz silica structures. *Superlattice Microstruct.* **35**, 227–237.
95. Evans, D. J. (1982). Homogeneous NEMD algorithm for thermal conductivity: application of non-canonical linear response theory. *Phys. Lett.* **91A**, 457–460.
96. Gillan, M. J. and Dixon, M. (1983). The calculation of thermal conductivity by perturbed molecular simulation. *J. Phys. C. Solid State* **16**, 869–878.
97. Evans, D. J. and Morriss, G. P. (1984). Non-Newtonian molecular dynamics. *Comp. Phys. Rep.* **1**, 297–344.
98. Evans, D. J. and Morriss, G. P. (1990). “Statistical Mechanics of Nonequilibrium Liquids”. Academic Press, New York.
99. Hansen, J. P. and McDonald, I. R. (1986). “Theory of Simple Liquids”. Academic Press, New York.
100. Maeda, A. and Munakata, T. (1995). Lattice thermal conductivity via homogeneous nonequilibrium molecular dynamics. *Phys. Rev. E* **52**, 234–239.
101. Osman, M. A. and Srivastava, D. (2001). Temperature dependence of the thermal conductivity of single-wall carbon nanotubes. *Nanotechnology* **12**, 21–24.
102. Majumdar, A. (1998). Microscale energy transport in solids. In “Microscale Energy Transport” (C.-L. Tien, A. Majumdar and F.M. Gerner, eds.). Taylor Francis, Washington.
103. Christen, D. K. and Pollack, G. L. (1975). Thermal conductivity of solid argon. *Phys. Rev. B* **12**, 3380–3391.
104. Maiti, A., Mahan, G. D., and Pantelides, S. T. (1997). Dynamical simulations of nonequilibrium processes heat flow and the Kapitza resistance across grain boundaries. *Solid State Commun.* **102**, 517–521.
105. Muller-Plathe, F. (1997). A simple nonequilibrium molecular dynamics method for calculating the thermal conductivity. *J. Chem. Phys.* **106**, 6082–6085.
106. Schelling, P. K. and Phillpot, S. R. (2001). Mechanism of thermal transport in zirconia and yttria-stabilized zirconia by molecular-dynamics simulation. *J. Am.Ceram. Soc.* **84**, 2997–3007.
107. Lukes, J. R., Li, D. Y., Liang, X.-G., and Tien, C.-L. (2000). Molecular dynamics study of solid thin-film thermal conductivity. *J. Heat Transfer* **122**, 536–543.
108. Chantrenne, P. and Barrat, J.-L. (2004). Finite size effects in determination of thermal conductivities: comparing molecular dynamics results with simple models. *J. Heat Transfer* **126**, 577–585.

109. Mountain, R. D. and MacDonald, R. A. (1983). Thermal conductivity of crystals: a molecular dynamics study of heat flow in a two-dimensional crystal. *Phys. Rev. B* **28**, 3022–3025.
110. Michalski, J. (1992). Thermal conductivity of amorphous solids above the plateau: molecular-dynamics study. *Phys. Rev. B* **45**, 7054–7065.
111. Oligschleger, C. and Schon, J. C. (1999). Simulation of thermal conductivity and heat transport in solids. *Phys. Rev. B* **59**, 4125–4133.
112. Noya, E. G., Srivastava, D., Chernozatonskii, L. A., and Menon, M. (2004). Thermal conductivity of carbon nanotube peapods. *Phys. Rev. B* **70**, 115416-1-5.
113. Cummings, A., Osman, M., Srivastava, D., and Menon, M. (2004). Thermal conductivity of Y-junction carbon nanotubes. *Phys. Rev. B* **70**, 115405-1-6.
114. Poetsch, R. H. H. and Bottger, H. (1994). Interplay of disorder and anharmonicity in heat conduction: molecular-dynamics study. *Phys. Rev. B* **50**, 15757–15763.
115. Imamura, K., Tanaka, Y., Nishiguchi, N., Tamura, S., and Maris, H. J. (2003). Lattice thermal conductivity in superlattices: molecular dynamics calculations with a heat reservoir method. *J. Phys.: Condens. Matter* **15**, 8679–8690.
116. Tenenbaum, A., Ciccotti, G., and Gallico, R. (1982). Stationary nonequilibrium states by molecular dynamics Fourier's law. *Phys. Rev. A* **25**, 2778–2787.
117. Maruyama, S. (2000). Molecular dynamics method for microscale heat transfer. *Adv. Numer. Heat Transfer* **2**, 189–226.
118. Maruyama, S. (2003). A molecular dynamics simulation of heat conduction of a finite length single walled nanotube. *Microscale Therm. Eng.* **7**, 41–50.
119. Jund, P. and Jullien, R. (1999). Molecular-dynamics calculation of the thermal conductivity of vitreous silica. *Phys. Rev. B* **59**, 13707–13711.
120. Yoon, Y.-G., Car, R., Srolovitz, D. J., and Scandolo, S. (2004). Thermal conductivity of crystalline quartz from classical simulations. *Phys. Rev. B* **70**, 012302-1-4.
121. Heino, P. and Ristolainen, E. (2003). Thermal conduction at the nanoscale in some metals by MD. *Microelectr. J* **34**, 773–777.
122. Ikeshoji, T. and Hafskjold, B. (1994). Nonequilibrium molecular dynamics calculation of heat conduction in liquid and through liquid–gas interface. *Mol. Phys.* **81**, 251–261.
123. Lukes, J. R. and Tien, C.-L. (2004). Molecular dynamics simulation of thermal conduction in nanoporous thin films. *Microscale Therm. Eng.* **8**, 341–359.
124. Liang, X.-G. and Shi, B. (2000). Two-dimensional molecular dynamics simulation of the thermal conductance of superlattices. *Mater. Sci. Eng. A Struct.* **292**, 198–202.
125. Abramson, A. R., Tien, C.-L., and Majumdar, A. (2002). Interface and strain effects on the thermal conductivity of heterostructures: a molecular dynamics study. *J. Heat Transfer* **124**, 963–970.
126. Chen, Y., Li, D., Yang, J., Wu, Y., Lukes, J. R., and Majumdar, A. (2004). Molecular dynamics study of the lattice thermal conductivity of Kr/Ar superlattice nanowires. *Physica B* **349**, 270–280.
127. Konashi, K., Ikeshoji, T., Kawazoe, Y., and Matsui, H. (2003). A molecular dynamics study of thermal conductivity of zirconium hydride. *J. Alloy. Compd.* **356–357**, 279–282.
128. Kotake, S. and Wakuri, S. (1994). Molecular dynamics study of heat conduction in solid materials. *JSME Int. J. B – Fluid T* **37**, 103–108.
129. Bedrov, R. and Smith, G. D. (2000). Thermal conductivity of molecular fluids from molecular dynamics simulations: application of a new imposed-flux method. *J. Chem. Phys.* **113**, 8080–8084.
130. Daly, B. C., Maris, H. J., Imamura, K., and Tamura, S. (2002). Molecular dynamics calculation of the thermal conductivity of superlattices. *Phys. Rev. B* **66**, 024301-1-7.

131. Daly, B. C., Maris, H. J., Tanaka, Y., and Tamura, S. (2003). Molecular dynamics calculation of the in-plane thermal conductivity of GaAs/AlAs superlattices. *Phys. Rev. B* **67**, 033308-1-3.
132. Allen, P. B., Feldman, J. L., Fabian, J., and Wooten, F. (1999). Diffusions, locons and propagons: character of atomic vibrations in amorphous Si. *Philos. Mag. B* **79**, 1715–1731.
133. Anderson, C. V. D. R. and Tamma, K. K. (2004). An overview of advances in heat conduction models and approaches for prediction of thermal conductivity in thin dielectric films. *Int. J. Numer. Method Heat* **14**, 12–65.